APPROVAL SHEET

Title of Thesis: Light Propagation Into, Out of, and Through Mid-Infrared Optical Fibers

Name of Candidate: Robert Joseph Weiblen
Doctor of Philosophy, 2015

Thesis and Abstract Approved: Curtis R. Menyuk

Curtis R. Menyuk
Professor
Department of Computer Science and
Electrical Engineering

Date Approved: November 23, 2015

Curriculum Vitae

Robert Joseph Weiblen

EDUCATION

Ph.D. **Electrical Engineering**
University of Maryland, Baltimore County, December 2015
Dissertation: *Light Propagation Into, Out of, and Through Mid-Infrared Optical Fibers*
Advisor: Curtis Menyuk

B.S. **Computer Engineering**
University of Maryland, Baltimore County, May 2007

ACTIVITES

Reviewer for *Optics Express*, *Applied Optics*

AWARDS

University Scholarship, **University of Maryland, Baltimore County** 2003–2007

JOURNAL PUBLICATIONS

1. **R. J. Weiblen**, A. Docherty, J. Hu, and C. R. Menyuk, "Calculation of the expected bandwidth for a mid-infrared supercontinuum source based on As_2S_3 chalcogenide photonic crystal fibers," Opt. Exp. **18**, 26666–26674 (2010). (*invited*)

2. **R. J. Weiblen**, A. Docherty, C. R. Menyuk, L. B. Shaw, J. S. Sanghera, and I. D. Aggarwal, "Calculation of the expected output spectrum for a mid-infrared supercontinuum source based on As_2S_3 chalcogenide photonic crystal fibers," Opt. Exp. **22**, 22220-22231 (2014).

3. **R. J. Weiblen**, C. Florea, L. Busse, L. B. Shaw, C. R. Menyuk, I. Aggarwal, and J. Sanghera, "Irradiance Enhancement and Increased Laser Damage Threshold in As_2S_3 Motheye Antireflective Structures," Optics Letters (in publication).

CONFERENCE PUBLICATIONS

1. **R. J. Weiblen**, J. Hu, C. R. Menyuk, L. B. Shaw, J. S. Sanghera, and I. D. Aggarwal, "Maximizing the Supercontinuum Bandwidth in As_2S_3 Chalcogenide Photonic Crystal Fibers," in Proc. Conference on Lasers and Electro-Optics (CLEO), San Jose, CA, paper CTuX7 (2010).

2. C. R. Menyuk, J. Hu, **R. J. Weiblen**, and A. Docherty, "Supercontinuum Generation at Mid-IR Wavelengths in Chalcogenide Photonic Crystal Fibers, Frontiers in Optics, San Jose, CA paper FTuW1, (2011). (*invited*)

3. **R. J. Weiblen**, C. Florea, A. Docherty, C. R. Menyuk, L. B. Shaw, J. Sanghera, L. Busse, I. Aggarwal, "Optimizing motheye antireflective structures for maximum coupling through As_2S_3 optical fibers," *IEEE Photonics Conference*, Burlingame, CA, paper ThP3 (2012).

4. **R. J. Weiblen**, A. Docherty, C. R. Menyuk, L. B. Shaw, J. Sanghera, I. Aggarwal, "Efficient Calculation of the Mid-Infrared Supercontinuum Spectrum in As_2S_3 optical fibers," *IEEE Photonics Conference*, Bellevue, WA, paper WB4.4 (2013).

5. C. R. Menyuk, **R. J. Weiblen**, J. Hu, B. Shaw, J. S. Sanghera, and I. D. Aggarwal, "Maximizing the bandwidth while minimizing the spectral fluctuations using supercontinuum generation in photonic crystal chalcogenide fibers," SPIE Security + Defence, Dresden, Germany, paper 8898-12 (2013). (*invited*)

6. **R. J. Weiblen**, C. Florea, L. Busse, L. B. Shaw, C. R. Menyuk, I. Aggarwal, and J. Sanghera, "Increased Laser Damage Threshold in As_2S_3 Motheye Antireflective Structures," in CLEO: 2014, OSA Technical Digest (online) (Optical Society of America, 2014), paper JTh3J.4.

7. C. R. Menyuk, **R. J. Weiblen**, J. Hu, I. D. Aggarwal, B. Shaw, and J. S. Sanghera "Maximizing the bandwidth while minimizing the spectral fluctuations using supercontinuum generation in photonic crystal chalcogenide fibers," *IEEE Photonics Society Summer Topicals Meeting*, Nassau, Bahamas, paper 334982 (2015). (*invited*)

8. **R. J. Weiblen**, C. Florea, L. Busse, L. B. Shaw, C. R. Menyuk, I. Aggarwal, and J. Sanghera, "Ideal Cusp-like Motheye Antireflective Structures for Chalcogenide Optical Fibers," *IEEE Photonics Conference*, Reston, VA, paper WG1.4 (2015).

ABSTRACT

Title of Thesis: Light Propagation Into, Out of, and Through Mid-Infrared Optical Fibers

Robert Joseph Weiblen, Doctor of Philosophy, 2015

Dissertation directed by: Curtis R. Menyuk, Professor
Department of Computer Science and
Electrical Engineering

This dissertation studies the theory of mid-infrared (mid-IR) light ($\sim$1–10 μm) transmission into, out of, and through mid-infrared optical fibers. This work is broadly comprised of three separate topics — mid-IR supercontinuum generation in chalcogenide photonic crystal fibers (PCFs), moth-eye anti-reflective (AR) microstructures for mid-IR fibers, and negative curvature fibers for broadband mid-IR transmission. Mid-IR radiation has a number of military, biomedical, chemical sensing, and industrial applications that often require high power and broad bandwidth. Consequently, the generation of this broad bandwidth (using supercontinuum generation), its efficient coupling to waveguides (using moth-eye structures), and low-loss transmission (using antiresonant fibers) are of important practical interest. This work has been carried out in collaboration with an experimental group from the Naval Research Laboratory (NRL) specializing in mid-IR optics and chalcogenide glasses.

Supercontinuum (SC) generation is a complex nonlinear process that uses highly nonlinear optical fibers to broaden the bandwidth of a narrow-band input laser source. We extended earlier work in arsenic selenide (As_2Se_3) PCFs to arsenic sulfide (As_2S_3) and optimized the input parameters to maximize the output bandwidth as we changed the input pulse peak power and pulse duration. We noticed that the output bandwidth was extremely sensitive to small changes in the input parameters. However, this sensitivity is not visible in

experiments due to pulse averaging. We then employed several simulation methods short of large-scale ensemble averaging to reduce the uncertainty in the output bandwidth. The use of these methods offered only a slight reduction in the uncertainty of the output bandwidth; so, we next undertook a large study to completely characterize the statistics of the output spectrum from a supercontinuum source and to definitively determine the output spectrum and corresponding bandwidth that might be observed in an actual experiment. We used a large-scale ensemble average and determined the approximate number of realizations necessary to obtain a converged bandwidth and spectrum.

Moth-eye structures are a biomimetic anti-reflective microstructure that can be etched, milled, grown, stamped, or otherwise imprinted onto optical surfaces to reduce Fresnel reflections. We validated several simulation methods by matching the experimentally-recorded transmission spectrum of a particular moth-eye structure. Using these methods, we investigated the effect of changing the shape, size, and period of a moth-eye structure on its transmission spectrum in the region of 2–5 μm. We used this knowledge to design optimal moth-eye structures that had greater than 99% transmission in this wavelength range. We also investigated localized field enhancement effects in moth-eye structures to determine the reason for their high laser-induced damage threshold. We found that localized field enhancement occurs mostly in the air, rather than in the glass, allowing moth-eye structures to melt before suffering catastrophic damage at nearly the same levels as untreated glass.

Antiresonant fibers (ARF) are a novel type of hollow-core optical fiber that guide light in an air core by the convex curvature of the core wall. Previous work by others on ARFs have focused on silica, but a design based on chalcogenide glasses such as As_2Se_3 will have much lower loss in the mid-IR. We investigate and optimize the size of the core and other dimensions of the fiber to minimize the fiber loss in the range of 1–10 μm. We also study

the effect of imperfect fabrication of As_2S_3 ARFs.

Light Propagation Into, Out of, and Through Mid-Infrared Optical Fibers

by

Robert Joseph Weiblen

Thesis submitted to the Faculty of the Graduate School
of the University of Maryland in partial fulfillment
of the requirements for the degree of
Doctor of Philosophy
2015

To Robert Eugene Weiblen

ACKNOWLEDGMENTS

I am extremely grateful to my research advisor, Dr. Curtis Menyuk, for his gifted tutelage and unwaivering support for my education and research. Dr. Menyuk's tireless efforts to foster a research environment where scientific endeavor can thrive have helped me immensely in this work. I would like to thank the distinguished associates in Dr. Menyuk's research group that I have had the privilege of working with: John Zweck, Johnathan Hu, Anis Talkukder, Andrew Docherty, Tom Carruthers, Brian Marks, and Giuseppe D'Aguano. I also acknowledge the ever-present assistance and camaraderie of my research group colleagues: Shaokang Wang, Yue Hu, Ehsan Jamali, Pat Sykes, and Zhen Qi.

I would like to thank my experimental collaborators at the Naval Research Laboratory — Brandon Shaw, Catalin Florea, Lynda Busse, Jesse Frantz, Rafael Gattass, Jas Sanghera, and Ishwar Aggarwal — for useful discussions about science and their support for my doctoral research. I am especially grateful for their suggestions for fruitful and interesting research topics that are always timely and impactful.

I would also like to acknowledge the love and support of my family, who make the rest of my life possible in general.

The hardware used in the computational studies in Section 2.3 and Chapter 4 is part of the UMBC High Performance Computing Facility (HPCF). The facility is supported by the U.S. National Science Foundation through the MRI program (grant nos. CNS–0821258 and CNS–1228778) and the SCREMS program (grant no. DMS–0821311), with additional substantial support from the University of Maryland, Baltimore County (UMBC). See `www.umbc.edu/hpcf` for more information on HPCF and the projects using its

resources.

TABLE OF CONTENTS

List of Figures

List of Tables

Chapter 1

Introduction

Introduction

Mid-IR wavelengths (∼2–20 μm) are technically and scientifically interesting for many reasons. The mid-IR spectrum is important for materials processing, chemical and biological sensing, and spectroscopy because many important organic compounds have strong resonances in this wavelength region [1]. Also, this spectral region includes two atmospheric transmission windows from 3–5 μm and 8–13 μm; so, it is also of interest for atmospheric science and sensing and remote explosive detection. Important industrial applications include laser cutting and welding [2]. Mid-IR radiation can also be used for tissue ablation and other medical therapies. Among a number of military applications, the most important is perhaps infrared countermeasures, or the defense against heat-seeking missiles [3]. Many of these applications require or benefit from a broad bandwidth of mid-IR radiation with high average and peak power. However, due to the strong resonances of many molecules in this region and the relatively high absorption loss of glasses in this wavelength region, especially silica, these requirements are often difficult to achieve at mid-IR wavelengths. This work will focus on optimizing technologies that improve the utility of mid-IR optical fibers for these and many other applications by increasing bandwidth and

reducing loss.

The first topic that I discuss in this dissertation is supercontinuum (SC) generation. SC generation, the broadening of input laser light bandwidth using nonlinear optical fibers, is potentially of use in the applications just described. Generating many wavelengths of radiation at once can simplify and speed up sensing and spectroscopy, since sources do not have to sweep through the wavelength range. Supercontinuum generation is essential to infrared countermeasures, since heat-seeking missiles simultaneously detect a wide spectral range. Supercontinuum generation works by using nonlinearities—principally the Kerr effect and the Raman effect—and dispersion in optical fibers to broaden the bandwidth of the input radiation, which is usually pulsed. Using a PCF for SC generation allows the tailoring of the chromatic dispersion and the narrowing of the fiber core, both of which aid in broadening the SC bandwidth. For mid-IR SC generation, it is necessary to use materials that are transparent in the mid-IR spectral range. The chalcogenides As_2S_3 and As_2Se_3 are well-suited to this task because of their low loss in the mid-IR spectral range and their high nonlinear refractive indices compared to other glasses [3].

In initial work on SC generation, we extended work by Hu [4] to optimize the fiber and input parameters to maximize the bandwidth of SC generation in As_2S_3 PCFs [5]. We found that we could generate approximately 4 μm of output bandwidth using an input pump wavelength of 2.8 μm that spans the wavelength range of 2–6 μm. Compared to previous studies by Hu et al. [4], the longer input wavelength allowed for the use of a greater PCF air-hole pitch, which increased the distance between the zero-dispersion wavelengths. This increase allows the soliton self-frequency shift (SFSS) to occur over a broader bandwidth, hence increasing the output bandwidth. However, we also found that the higher power and longer input wavelength compared to previous studies [4] led to an extreme sensitivity of the output bandwidth to small changes in the input parameters. This sensitivity of the

numerical study leads to two major issues with modeling the experiments. First, this sensitivity cannot be observed in an experiment due to averaging effects because the optical spectrum analyzer (OSA) averages over many pulses from the input laser source. Secondly, it makes it difficult to determine the optimal settings for maximum bandwidth. Additionally, the spectrum that is produced by a single numerical simulation contains a large amount of spectral fluctuations that cannot be observed in experiments because of averaging over pulse-to-pulse variations in the pulse width and peak power, which can each vary by as much as 10%. These spurious fluctuations and make the bandwidth difficult to define. For these reasons, it is desirable to obtain a more certain measure of the output spectrum and its bandwidth from a particular set of input parameters.

We attempted to reduce the uncertainty in the output bandwidth using a number of methods [6]. First, we used an artificially large OSA filter bandwidth for greater spectral smoothing. Second, we defined the output bandwidth in a recursive way that is more robust to fluctuations in the output spectrum as a function of wavelength. Finally, we used small-scale ($\sim$100 realization) ensemble averaging over one pulse parameter to reduce fluctuations in bandwidth as a function of the input pulse parameters. These efforts yielded approximately the same bandwidth as in the previous study, but with reduced uncertainty.

The bandwidth as a function of the input pulse parameters found in the previous study is expected to be an approximation to the experimentally-expected bandwidth, but not as quantitatively accurate as a large ensemble average would be. Additionally, the spectrum found using the method just described is not expected to have converged to its experimentally-expected value, since the modification of the spectrum is due to artificial smoothing. In order to accurately determine the experimentally-expected spectrum and its actual bandwidth, we next used a large scale ensemble average over thousands of output spectrum realizations, varying the pulse parameters by 10% [7]. Initial estimates of the

correlation of the SC spectra from numerical simulations suggested that as many as 10^6 realizations might be necessary to find a converged spectrum. Indeed, the variance of the spectral fluctuations continues to decrease up to 10^6 realizations, but the spectrum and the bandwidth are sufficiently converged after about 5000 realizations. This number of realizations is a reasonable number that can be computed on present hardware in a few hours.

The second topic that I discuss in this dissertation is moth-eye structures. Moth-eye structures are a microstructured AR surface structure that are effective at reducing Fresnel reflections. In the long wavelength limit, they work by providing a gradual change of the effective refractive index as light propagates across the air-glass interface. They are especially useful for high-index materials, such as most mid-IR materials, including chalcogenide glasses. Reducing Fresnel reflections from optical interfaces is extremely important in mid-IR applications where high power and low loss are needed. High power laser radiation that reflects from interfaces can damage instruments, while insertion losses can be a major contributor to overall losses in a system. Hence, mid-IR systems can greatly benefit by using moth-eye structures to reduce reflections from interfaces and increase transmission through them. Scientists at the Naval Research Laboratory recently demonstrated a direct stamping method for imprinting these moth-eye structures on the end-faces of chalcogenide optical fibers [8]. The direct stamping method allows structures to be accurately replicated, which means they must be accurately modeled. Because the microstructure feature dimensions are on the same order as the wavelength of the incoming radiation ($\sim$1 μm), neither the long-wavelength average refractive index model nor the short-wavelength ray optics model is appropriate to describe transmission through moth-eye structures. Thus, they must be modeled using rigorous methods, such as the finite-difference time-domain (FDTD) method or the rigorous coupled-wave analysis (RCWA) method.

In initial work on moth-eye structures, my colleagues and I built an exact model of a particular moth-eye structure implemented in As_2S_3 glass and calculated the resulting transmission spectrum as a function of wavelength from 1–5 μm. We found we could match the experimentally observed transmission spectrum extremely well [9]. We used this model to investigate the effects of changing the geometry of the microstructure. First, we varied the dimensions of the structure. We found that, in general, increasing the height of the structure increases the transmission. Next, we varied the shape of the microstructure element, using cones, truncated cones, pyramids, half-ellipsoids, and sinusoidally shaped elements. We studied both positive shapes, which are raised from the surface, and negative shapes, which are depressed into the surface. We found that, as long as the dimensions were optimized, any structure shape could give excellent transmission in the wavelength range of interest. However, we found that some shapes, including pyramids and half-ellipsoids could be designed to give up to 99.9% average transmission from 1–5 μm [10].

An interesting advantage of moth-eye structures is that surfaces with moth-eye structures suffer catastrophic damage at much higher laser fluences than traditional thin-film AR coatings. This fact may seem counterintuitive since it might be expected that the microstructured surface causes field enhancement. This field enhancement should reduce the amount of energy per unit area required to cause catastrophic damage. We used our model to calculate the average Poynting flux density in and around the microstructures of a moth-eye structured surface to investigate why moth-eye structures are resistant to laser damage [11,12]. We found that, indeed, localized field enhancement does occur, but mostly in the air side of the air-glass interface. This enhancement can be physically understood by using the boundary conditions for electromagnetic waves from a medium with one index of refraction to another. The reduction in energy density in the glass allows the glass to heat up more slowly, which causes moth-eye structured surfaces to melt and suffer catastrophic

damage at levels similar to untreated glass [13].

The final topic that I discuss in this dissertation is antiresonant fibers (ARFs). Antiresonant fibers (ARFs) or negative curvature hollow-core fibers (NCHCFs) [14, 15] are a relatively recent (circa 2011) type of optical fiber with a hollow core and a microstructured cladding. Guidance is achieved by the negative curvature of the core wall. Because these fibers guide light in a hollow core, the loss can be greatly reduced over a broad wavelength range, provided that light is well confined. Additionally, nonlinearity is greatly reduced compared to a traditional solid-core fiber, which allows high power radiation to propagate without interference. Finally, because there is no glass in the core, the fibers are more robust to high laser fluences that might damage a traditional fiber. All of these advantages make ARFs an excellent choice for light guidance in high-power and broadband mid-IR applications. Whereas hollow-core photonic bandgap fibers offer extremely low loss over a narrow wavelength range and Kagome fibers offer a broad low-loss bandwidth at the expense of higher loss than hollow-core photonic bandgap fibers, ARFs are an excellent compromise in which low loss and broad bandwidth can be simultaneously achieved.

To date, most ARFs have been constructed from silica [16], principally because the processing of silica fibers is extremely advanced. The only design to date in a mid-IR material was made from $Te_{20}As_{30}Se_{50}$ (TAS) and only optimized for CO_2 laser power delivery at 10.6 μm [17]. We simulate chalcogenide ARFs with the goal of minimizing the loss over a broad bandwidth from 1–10 μm by optimizing the core size, cladding structure, and tailoring the resonance loss bands to match atmospheric loss peaks. We show that the resonant absorption bands of an As_2S_3 ARF can be designed to coincide with atmospheric absorption bands due to CO_2. We show that fibers with 6 cladding tubes have lower loss than fibers with 8 cladding tubes, as long as nested elements are included. Since we also show that nested elements must be included to obtain acceptable loss levels, it stands to

reason that chalcogenide ARFs should be designed with 6 cladding tubes. We also study the effect of changing the core radius of an As_2S_3 ARF, and we show that increasing the core radius decreases the loss, but at a decreasing rate.

We also study the influence of parameter variations on the loss spectrum for ARFs. We study the effect of a nonconstant cladding tube wall thickness, additional structures in the fiber jacket, variations in the cladding tube diameter, and variations in the cladding tube wall thickness for a single tube.

The remainder of this dissertation is organized as follows: In the second chapter, we study supercontinuum generation in chalcogenide PCFs. We show that it is possible to generate 4 μm of bandwidth in an As_2S_3 fiber, but the maximum bandwidth and the optimal parameters that correspond to it are difficult to determine exactly, due to the sensitivity of supercontinuum generation to small fluctuations in the input parameters. We then describe methods for finding a reliable bandwidth and output spectrum and the corresponding parameters with increased certainty.

In the third chapter, we design and optimize moth-eye antireflective nanostructures for use on As_2S_3 glass, especially the end faces of As_2S_3 fibers. We show that moth-eye structures can increase the average transmission through an As_2S_3 surface from $\sim$83% to $\sim$99.9%. We also explain the reason for the increased laser damage threshold in moth-eye structures.

In the fourth chapter, we design and optimize negative-curvature hollow-core antiresonant As_2S_3 fibers for mid-IR power delivery. In these fibers, the primary objective is to have a wide bandwidth and low loss. We also investigate the robustness of these designs in the presence of imperfect fabrication.

The fifth chapter contains conclusions that summarize the principal results of this dissertation.

Chapter 2

Supercontinuum generation

Supercontinuum generation at mid-IR wavelengths is an area of great research interest because of its importance for many applications, including biological spectroscopy [18], optical frequency metrology [19], optical tomography [20], optical cutting and welding [2], and aircraft defense [3].

To model SC generation, we use the same computational method as Hu et. al. [4, 21]. This method proceeds in two step. The first step is to calculate the loss and dispersion of the PCF for a given geometry. The second step is to solve for the pulse evolution along the fiber using the calculated loss and dispersion. The equation that governs the evolution of a single SC simulation is the generalized nonlinear Schrödinger equation (GNLSE) given by [22]:

$$\frac{\partial A(z,t)}{\partial z} + \frac{a}{2}A - i\,\mathrm{IFT}\Big\{[\beta(\omega_0+\Omega) - \beta(\omega_0) - \Omega\beta_1(\omega_0)]\tilde{A}(z,\Omega)\Big\} = i\gamma\Big(1 + \frac{i}{\omega_0}\frac{\partial}{\partial t}\Big)\Big[A(z,t)\int_{-\infty}^{t} R(t-t')|A(z,t')|^2\,dt'\Big], \quad (2.1)$$

where $A(z,t)$ is the electric field envelope and $\tilde{A}(z,\omega)$ is its Fourier transform, a is the fiber

loss, and γ is the Kerr coefficient. The Kerr coefficient is given by $\gamma = n_2\omega_0/(cA_{\text{eff}})$, where n_2 is the nonlinear refractive index, ω_0 is the angular frequency of the optical carrier, c is the speed of light, and A_{eff} is the fiber's effective area. The quantity $R(t)$ is the nonlinear response function defined by $R(t) = (1 - f_R)\delta(t) + f_R h_R(t)$, which includes both the instantaneous Kerr contribution, $\delta(t)$, and the delayed Raman response, $h_R(t)$. We use f_R to denote the fraction of the nonlinear response function due to the Raman effect, and we use IFT$\{\}$ to denote the inverse Fourier transform. The Kerr nonlinearity in As_2S_3 is given by $n_2 = 3.285 \times 10^{-18}$ m^2 W^{-1}, the Raman fraction is given by $f_R = 0.2$, and the nonlinear coefficient γ is calculated for each air-hole pitch based on the effective mode area of the numerically calculated mode. The Raman gain response of As_2S_3 was measured experimentally, and we used the Kramers-Kronig relations to find the complete Raman response function; the resulting data is published in Fig. 2 of [23]. The GNLSE is solved numerically using the split-step Fourier method implemented in MATLAB [24].

In all our studies, we use a PCF with a hexagonal geometry, as shown schematically in Fig. 2.1. The two fiber parameters that affect the dispersion are d, the air-hole diameter, and Λ, the air-hole pitch. In order to keep the fiber endlessly single-mode, we fix the air-hole diameter-to-pitch ratio in our simulations at $d/\Lambda = 0.4$. This value has been found to be the largest that is consistent with single-mode operation [21]. It is advantageous to maximize d/Λ to decrease the effective index of the cladding material, and hence increase nonlinearity and modal confinement. Thus, we optimize the fiber geometry over the single parameter of the air-hole pitch Λ. The input source wavelength is given as 2.8 μm. For all simulations except when studying the effect of varying the fiber length, we use a fiber length of 0.5 m. This value is currently used in experiments and gives a good balance between the extra spectral power that is generated at longer wavelengths by the soliton self-frequency shift as the length increases, and the negative effect of increased fiber loss.

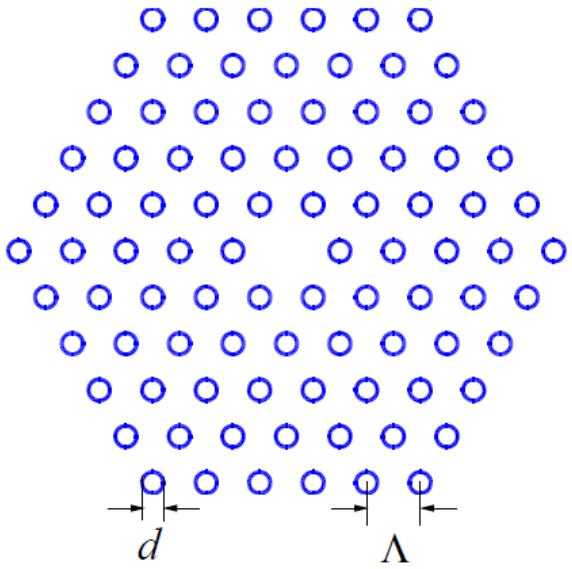

Figure 2.1: Hexagonal PCF air-hole geometry.

In optimization studies, we consider four air-hole pitches over the range of interest. They are 2.5 μm, 3.0 μm, 3.5 μm, and 4.0 μm. The chromatic dispersion as a function of frequency, $\beta(\omega)$, and leakage loss of a PCF with each of these pitches are plotted in Figs. 2.2(a) and (b), respectively. As the pitch increases, the anomalous dispersion region broadens and begins at slightly longer wavelengths. In general, larger pitches are advantageous for a number of reasons. First, given a sufficiently long wavelength pump and sufficient pump power, the phase matching condition for four-wave mixing has a wider separation between Stokes and anti-Stokes wavelengths for larger pitches. This wider separation results in a wider bandwidth for the spectral broadening in the first few centimeters of the fiber, which is dominated by four-wave mixing. Second, since the rate of the soliton self-frequency shift is proportional to the chromatic dispersion, PCFs with a larger pitch have more broadening from the soliton self-frequency shift. This shift is the dominant source of the large spectral broadening that occurs after the initial four-wave mixing broad-

ening [25]. However, a larger pitch in a PCF also leads to an increase in the effective mode area, which decreases modal confinement and hence nonlinearity, which in turn is detrimental to the supercontinuum broadening process. A larger mode area also increases the loss, since the mode extends further into the edge of the fiber.

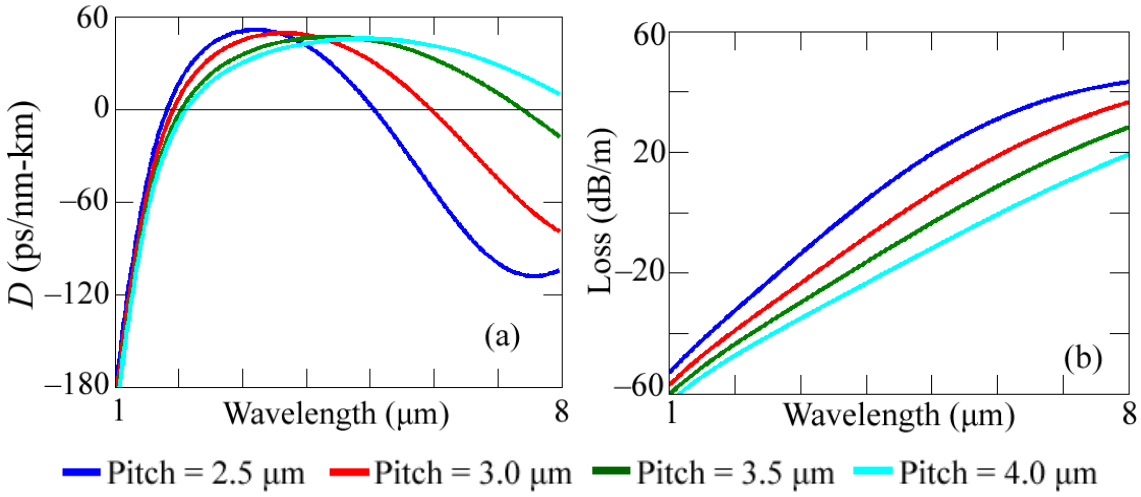

Figure 2.2: (a) Chromatic dispersion and (b) loss for hexagonal PCFs with pitches of 2.5 μm (blue), 3.0 μm (red), 3.5 μm (green), and 4.0 μm (cyan).

2.1 Maximizing the bandwidth in As_2S_3

Hu et al. previously showed that a bandwidth of over 4 μm could be generated in an As_2Se_3 chalcogenide photonic crystal fiber (PCF) with a 2.5 μm source [26]. Hu et al. also showed that 25% of the input power can be shifted into the range of 3–5 μm using an As_2S_3 chalcogenide PCF [27].

2.1.1 Simulation parameters In the work presented in this section, we optimize the fiber pitch and pulse duration in order to maximize the supercontinuum bandwidth in

As_2S_3 chalcogenide PCFs with a hexagonal structure using a source at $\lambda = 2.8$ μm and a hyperbolic-secant pulse shape. Intensities up to 3 GW/cm^2 in the range 2.5–3.0 μm can be obtained from commercial Ti:sapphire optical parametric amplifier femtosecond sources. These experimental parameters set the limits for our input pulse parameters.

In our optimization studies, we varied the pitch (Λ) between 2.5 μm and 4.0 μm. At each pitch, we set the peak intensity of the pulse to 1 GW/cm^2 and then determined the optimal pulse duration by varying the input pulse full-width half-maximum (FWHM) duration between 100 and 1500 fs. We then varied the input pulse peak intensity between 1 and 3.5 GW/cm^2 and verified that the pulse duration remained optimal.

2.1.2 Results In Figs. 2.3(a) and (b), we show the output bandwidth from the supercontinuum generation as a function of the FWHM pulse duration for different pitches at peak intensities of 1 GW/cm^2 and 3 GW/cm^2 respectively. We find that the output bandwidth is largest at a pitch of 4.0 μm and an intensity of 3 GW/cm^2. In Fig. 2.4, we show that the optimal bandwidth increases from about 2.5 μm to 4.0 μm as the intensity increases from 1.0 GW/cm^2 to 3.0 GW/cm^2, beyond which the bandwidth does not significantly increase. We attribute this saturation of the bandwidth with increasing input intensity to a decrease in the soliton self frequency shift at larger wavelengths and a rapid increase in the linear loss. As in previous studies [26, 27], we find that the number of solitons that are generated is a sensitive function of the input intensity, pulse duration, and fiber parameters, which leads to the lack of smoothness that is visible in Figs. 2.3 and 2.4.

In Fig. 2.5, we show the output spectral power with our optimal input peak intensity of 3.0 GW/cm^2 and the optimal input pulse duration of 1150 fs. We find that a flat bandwidth is achievable over a range between 2.5 μm and 6.5 μm where we used the points at which

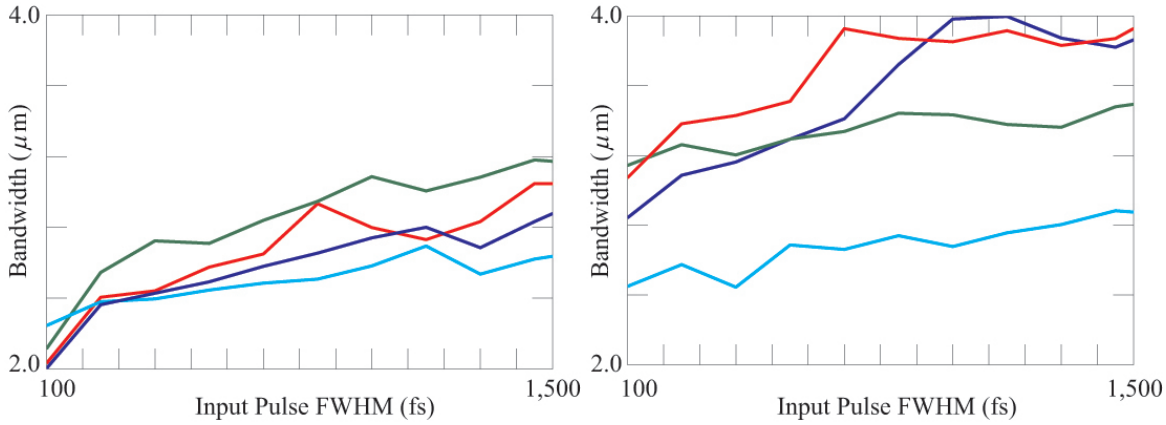

(**a**) 1 GW/cm^2 (**b**) 3 GW/cm^2

Figure 2.3: Output bandwidth vs. input pulse FWHM for $\Lambda = 2.5$ µm (cyan), $\Lambda = 3.0$ µm (green), $\Lambda = 3.5$ µm (red), $\Lambda = 4.0$ µm (blue) and an input peak intensity of (a) 1 GW/cm^2 and (b) 3 GW/cm^2.

the spectrum falls below 20 dB from the peak to determine the bandwidth. The steep fall-off around 7 µm is primarily due to the material loss of As_2S_3.

2.1.3 Discussion The optimal pitch of 4.0 µm is larger than the optimal pitch of 3.0 µm that was found in a prior study [27], where the goal was to optimize the power in the range of 3–5 µm. While the larger pitch increases the effective mode area and hence decreases the nonlinearity, the larger pitch also increases the wavelength at which the second zero dispersion wavelength is located and hence increases the bandwidth over which the soliton self-frequency shift remains effective [22]. The decrease in the nonlinearity is more than compensated by the increase in the bandwidth over which the soliton self-frequency shift remains effective.

The lack of smoothness in Figs. 2.3 and 2.4 make a reliable maximum bandwidth difficult to determine with certainty. In the balance of this chapter, we will investigate methods to reduce or eliminate this uncertainty for the purpose of finding an output bandwidth and

spectrum that correspond to what would be expected in an experiment.

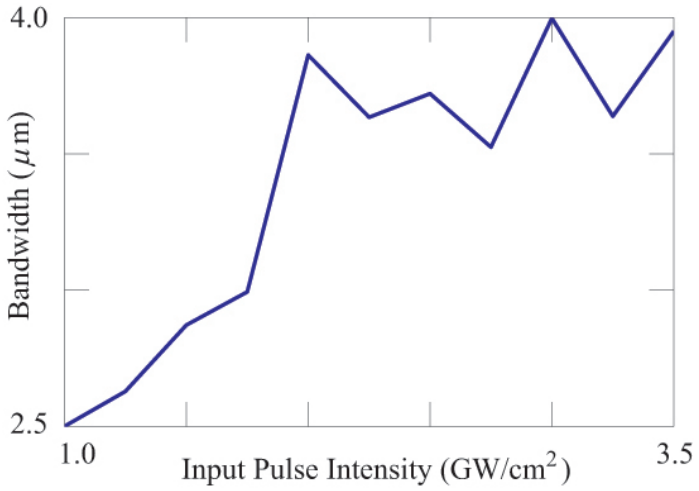

Figure 2.4: Output bandwidth vs. input pulse peak intensity.

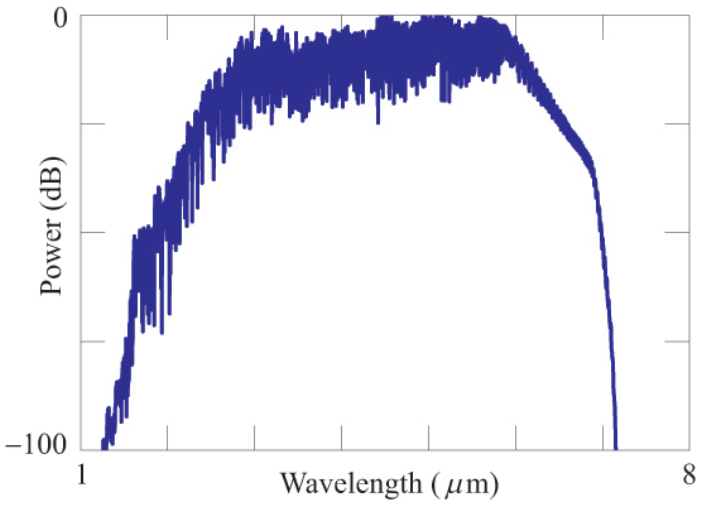

Figure 2.5: The spectrum of the supercontinuum that is generated.

2.2 Calculation of the experimentally expected bandwidth

One of the principal figures of merit by which a SC source is judged is the output bandwidth, although there are other measures of the SC output that are important for specific applications, such as the coherence properties of the spectrum [28] and the smoothness of the output spectrum [29]. When optimizing the bandwidth computationally, it is important to use a measure of the bandwidth that agrees with what would be obtained in an experimental system. In this section, we investigate a method to provide a better estimate of the bandwidth that would be observed in experiments, and we apply this method to optimize the SC bandwidth of a mid-IR SC source using an As_2S_3 PCF. In the previous section, studying the same SC source, we found a relatively large uncertainty in the optimum due to large fluctuations in the calculated bandwidth across the range of fiber and input pulse parameters (system parameters) [5]. Here, we investigate the variation of the output spectral bandwidth due to changes in the system parameters of the SC source. We use small steps in the pulse parameters to reveal the large variations in the calculated output bandwidth. These large variations would have led to false maxima if the sampling had been done less finely, as is almost universally the case in studies up to the present work, including those in the previous section.

A difficulty with the optimization of SC generation using an automated bandwidth calculation is that only calculating the bandwidth over a limited set of points in the optimization parameter space can lead to finding a false maximum. This difficulty becomes apparent when we calculate the bandwidth for many finely resolved values of the pulse duration, as shown in the next section. Large variations of the bandwidth for small changes in the pulse duration are apparent.

Moreover, these variations are not representative of the experimental system. In any

experimental system, the input pulse to the fiber will contain random quantum noise, and the pulse duration and energy will also change from pulse to pulse. Experimentally, the repetition rate of the laser pulse is much greater than the sampling rate of the spectral measurement; so, the experimental output spectrum is a time average of the actual SC output from many pulses. Therefore, the measured output spectra represents an ensemble average over quantum noise and random fluctuations in the system parameters, which consist of the input pulse and fiber parameters. Furthermore, experimental measurements have a finite spectral resolution, which also serves to smooth the spectrum and remove the large variations in the output [30].

A typical SC spectrum, such as the spectrum shown in Fig. 2.6(a), has a complex structure, which is a result of complicated soliton dynamics and depends on the number of interacting solitons, their interactions, pulse durations and individual powers — all of which are sensitive functions of the system parameters. This complex structure is changed by noise on the input pulse, and it has been shown that ensemble averaging over incoherent pulse noise leads to a smoothing of the output spectra [28].

2.2.1 Bandwidth calculation In practice, the bandwidth of a SC output spectrum is calculated as the width between the points in the spectrum that are 20 dB down from the peak value. In an experiment, the peak of the spectrum is always at the wavelength of the input source. However, in a simulation, spectral fluctuations can make the peak value and the 20 dB points difficult to determine.

Therefore, we can find a measure of the bandwidth that better represents the bandwidth that is experimentally measured by numerically approximating the experimental variations and noise on the pulse that can be expected in real systems by performing an ensemble average. Assuming that the main effect of noise on the input is to smooth the spectrum, we

may approximate the effect of this averaging on the output spectrum by artificially smoothing the spectrum. Experimentally, an optical spectral analyzer (OSA) effectively convolves the spectrum with a filter function of finite width. We can do the same computationally. We first smooth the spectrum by convolving it in the spectral domain with a super-Gaussian function of width λ_w,

$$S_f(\lambda) = \int_{\lambda-\Lambda}^{\lambda+\Lambda} \exp\Big[-\left(\frac{\lambda-\nu}{\lambda_w}\right)^4\Big] S(\nu) d\nu, \tag{2.2}$$

where $S_f(\lambda)$ is the filtered spectral density, $S(\lambda)$ is the input spectral density and Λ is chosen depending on the width of the filter function.

The effect of the OSA filter is shown in Fig. 2.6, in which one example of a SC output spectrum is filtered with different filter widths (λ_w). In practice, typical OSAs have a resolution bandwidth of approximately $\lambda_w = 10$ nm for SC generation experiments. However, our goal here is to smooth the numerical spectrum sufficiently to make automatic bandwidth calculations, so we choose a larger resolution bandwidth, namely $\lambda_w = 100$ nm.

To reduce the impact of peaks in the SC output affecting the bandwidth measurement we define the average output power spectral density (PSD) of a spectrum as the PSD of an equivalent ideal rectangular spectrum with the same total power and the same bandwidth as the spectrum being measured. This rectangular output spectrum has an averaged PSD ($\mathrm{PSD_{av}}$) calculated as

$$\mathrm{PSD_{av}} = \frac{P_{\mathrm{tot}}}{\mathrm{BW}}, \tag{2.3}$$

where P_{tot} is the total power in the output spectrum, and the bandwidth (BW) is the width of the spectrum between the points in the spectrum that are 20 dB lower than $\mathrm{PSD_{av}}$. This definition is recursive; however, it converges in a few iterations. Figure 2.6(b) shows an example spectrum, with the equivalent spectrum used in the bandwidth definition. This def-

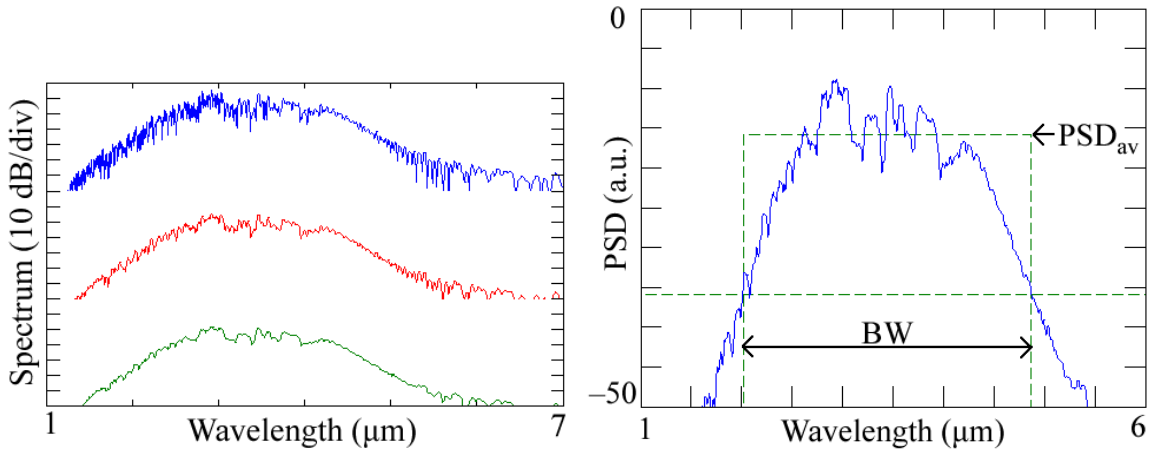

Figure 2.6: (a) Example spectra from an OSA with filter widths of $\lambda_w = 10$ nm (top), $\lambda_w = 50$ nm (middle), and $\lambda_w = 100$ nm (lower). (b) Power spectral density (PSD) for the same example spectrum (blue solid) and equivalent rectangular spectrum (green dashed) that are defined in the text.

inition of the bandwidth is slightly more complicated than the usual definition, but should be more robust to peaks in the output spectrum.

2.2.2 Bandwidth from averaging over pulse parameters

We apply the bandwidth calculation methods of Sec. 2.2.1 to the SC system that was previously described in Sec. 2.1.1. Fig. 2.7(a) shows a plot of the output bandwidth versus the input pulse full-width half-maximum (FWHM) for air-hole pitches of 2.5 μm, 3.0 μm, 3.5 μm, and 4.0 μm. In all cases, the short wavelength end of the bandwidth that we observed was at 2.5 μm and was defined by fiber loss [5]. The bandwidth for the PCF with a 2.5 μm pitch remains much the same as the pulse duration changes. When the pitch is increased to 3.0 μm, however, the output bandwidth increases markedly as the pulse duration increases. Also, the fluctuations in the bandwidth become large. They are on the order of 300 nm, or about 10%, for very small changes in the input pulse duration. These fluctuations in the measured bandwidth are even larger for a pitch of 3.5 μm, where the bandwidth fluctuates by as much as 800 nm.

Figure 2.7(b) shows a plot of the output bandwidth as a function of the input pulse peak power at a resolution of 1 W for air-hole pitches of 2.5 μm, 3.0 μm, 3.5 μm, and 4.0 μm. Again, the short wavelength end of the bandwidth is at 2.5 μm. Like Fig. 2.7(a), the output bandwidth varies greatly for a small change in pulse power. Again, the fluctuations are not as large for a pitch of 2.5 μm as they are for larger pitches. We note that for each pitch the bandwidth increases relatively smoothly to a peak power of around 300 W, after which there are large variations in the bandwidth.

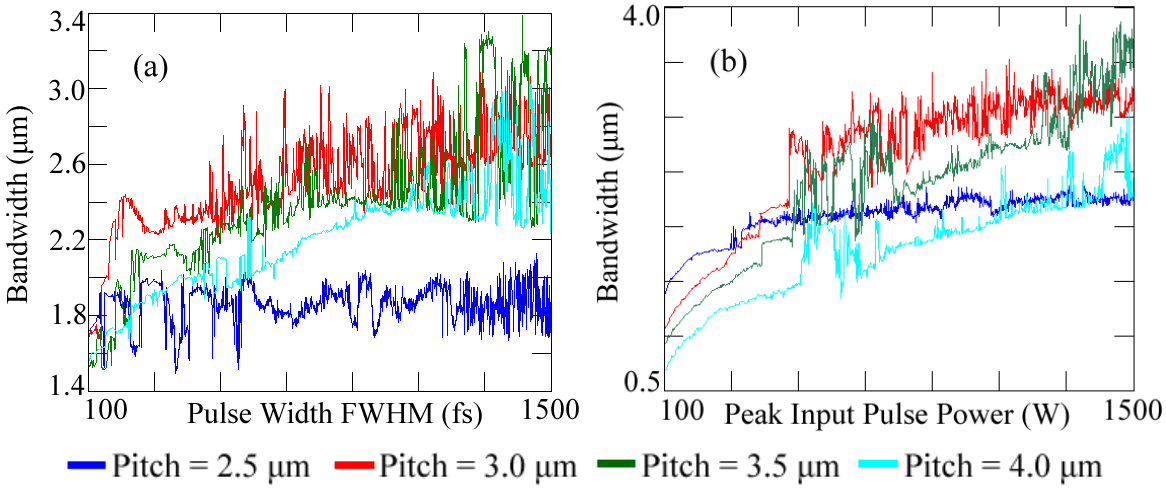

Figure 2.7: Bandwidth versus (a) input pulse duration, and (b) input pulse peak power, for air-hole pitches of 2.5 μm (blue), 3.0 μm (red), 3.5 μm (green), and 4.0 μm (cyan). In (a) the peak power is 1500 W, while in (b) the pulse duration FWHM is 1500 fs. The bandwidth is calculated for different pulse durations in steps of 1 fs. The peak power is varied in steps of 1 W.

It is clear from Fig. 2.7 that even after the spectral smoothing discussed in the previous section, corresponding to an average over the bandwidth of an optical spectrum analyzer, there are still considerable variations in the measured bandwidth that do not appear in an experimental system. As filtering the spectral output is not enough to remove these

unphysical variations, we calculated an ensemble average of the supercontinuum output for a range of pulse parameters that could be expected in an experimental system.

Figures 2.8(a) and 2.8(b) show the same data as Figs. 2.7(a) and 2.7(b), respectively, for a 3.5 μm pitch. However, we calculate the bandwidth by first averaging the pulse output for all simulations over a 10% variation in the input parameter (either pulse duration or peak power), which is a typical value, and then using the method described in the previous section. This bandwidth is plotted as a dashed line Figs. 2.8(a) and 2.8(b) and corresponds to the bandwidth that would be experimentally observed with a variation in system parameters of 10%. The bandwidth increases with increasing pulse duration and pulse peak power, but still has significant fluctuations.

Figure 2.8 makes clear the necessity of ensemble averaging to find an expected bandwidth. Spectral filtering alone is not enough to reduce the large-scale fluctuations in output power. Trying to determine an optimum set of parameters from Fig. 2.7 is unreliable.

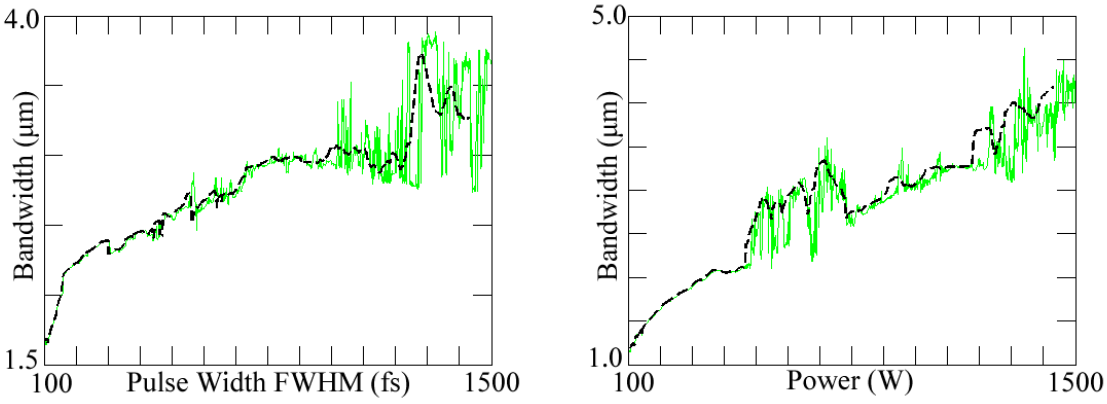

Figure 2.8: (a) Calculated bandwidth (solid) and ensemble-averaged bandwidth for a 10% parameter variation (dashed) vs. pulse duration FWHM for a pitch of 3.5 μm. (b) Calculated bandwidth (solid) and ensemble-averaged bandwidth for a 10% parameter variation (dashed) vs. peak input power for a pitch of 3.5 μm.

2.2.3 Application to optimization In Fig. 2.9, we show the average bandwidth that we calculated with the procedure described in Sections 2.2.1 and 2.2.2, applied to the data of Fig. 2.7. We find that, by keeping the pulse duration fixed at 1.5 ps, we can obtain an output bandwidth of about 4 μm for a pitch of 3.5 μm and powers greater than 1300 W. However, we see in Fig. 2.9 that a pitch of 3.0 μm more reliably yields a larger bandwidth than both 3.5 μm and 4.0 μm.

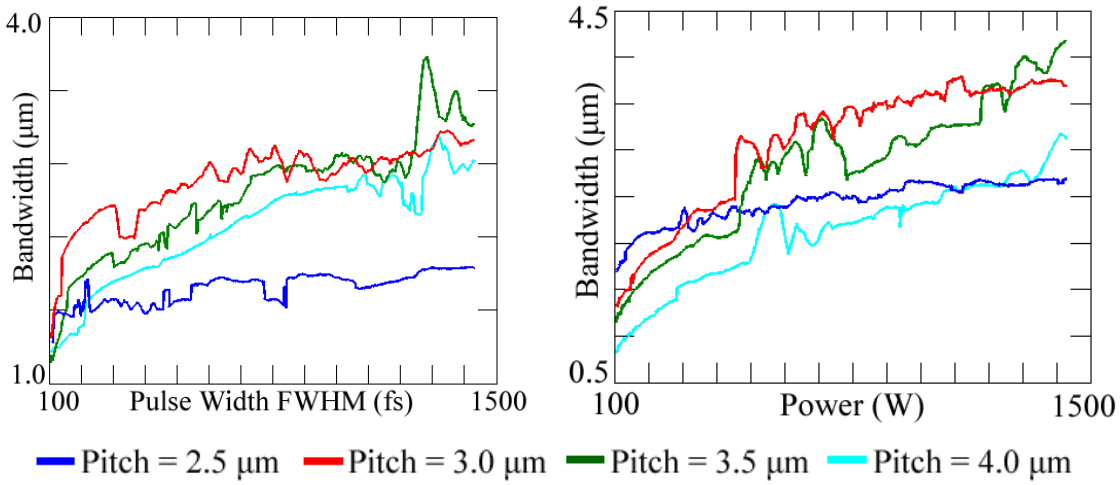

Figure 2.9: Bandwidth found using averaging method versus (a) input pulse duration and (b) input pulse peak power, for air-hole pitches of 2.5 μm (blue), 3.0 μm (red), 3.5 μm (green), and 4.0 μm (cyan). In (a) the peak power is 1500 W, while in (b) the pulse duration FWHM is 1500 fs. The bandwidth is calculated for different pulse durations in steps of 1 fs. The peak power is varied in steps of 1 W.

In a previous optimization study of the same supercontinuum source that was described in Section 2.1 [5], we found that the optimal parameters were a 4.0 μm pitch, a pulse duration of 1150 fs, and a peak input power of 1280 W. These parameters yielded an output bandwidth of about 4.0 μm, similar to the maximum bandwidth in this section. The present results are a more reliable estimate of the expected maximum bandwidth and optimal fiber and input pulse parameters, because in our previous work, we took large steps

in the pulse parameters and neglected the sensitivity of supercontinuum generation to small changes in the system parameters.

The uncertainty in choosing an optimum from Fig. 2.7 can be as high as 800 nm in about 3.5 μm, or more than 22%. The uncertainty in choosing an optimum from Fig. 2.9 is evident because the results of averaging over one parameter does not agree with results of averaging over the other. The bandwidth for a 3.5 μm pitch, 1430 fs pulse duration and 1500 W pulse peak power from Fig. 2.9(a) is about 3.7 μm. The bandwidth for a 3.5 μm pitch, 1500 fs pulse duration, and 1430 W pulse peak power from Fig. 2.9(b) is about 4.2 μm. Using these values to estimate the error in the ensemble-average method gives about 500 nm in 4 μm or slightly more than 10%. Thus, this method reduces uncertainty by more than 10%. Using this procedure, we find a reliable maximum bandwidth of 3.7 μm with a pitch of 3.0 μm that extends between 2.5 and 6.2 μm with an uncertainty of $\pm$ 0.3 μm.

This uncertainty, though reduced from previous studies, is still high. The next section describes how to find a reliable estimate of the output spectrum and its corresponding bandwidth.

2.3 Calculation of the experimentally expected output spectrum

A common aim in SC generation, especially in the mid-IR, is to obtain a broad bandwidth. Additionally, it is often desirable to generate a spectrum that is as flat as possible over the wavelength range of interest. Several characteristics of single-shot simulation results appear to indicate that SC sources cannot achieve these goals when the input pulse energies become large [6]. First, variations as large as 20 dB can exist over a single-shot spectrum. Also, the frequency of these variations depends on the bandwidth resolution. Finally, output bandwidths vary over a large range. This behavior when the input pulse energy is large contrasts strongly with the behavior when the input pulse energy is small, and

supercontinuum generation is highly reproducible from shot to shot. It has been shown that the number of solitons in the input pulse plays a critical role in determining the sensitivity of the supercontinuum spectrum to small variations in the input parameters [22].

However, the theoretically-predicted shot-to-shot variations cannot be observed in experiments, and we will show in this section that they are an artifact of single-shot simulations. In an experiment, the repetition rate of the input pulse source is much greater than the sampling rate of the optical spectrum analyzer. Therefore, the measured output spectrum of a SC source consists of an ensemble average over many thousands of pulse realizations, which include laser noise and pulse parameter (pulse duration and peak power) differences due to environmental effects. Because SC generation is extremely sensitive to small changes in the input pulse when the input pulse energy is large, a single numerical simulation will not yield an accurate representation of the experimental SC output or its bandwidth.

To obtain an accurate representation, it is necessary to use an ensemble average. That leads to the question of how large the ensemble must be in order to realistically simulate an experimental system. It is desirable for computational efficiency to use the smallest number of realizations possible. In the previous sections [5, 6] on mid-IR SC generation in As_2S_3 photonic crystal fibers, we found that changes of 0.01 % in either the pulse duration or the peak power lead to a SC spectrum that appears almost completely uncorrelated with the initial spectrum in the intermediate wavelength range of 2700–4600 nm. Since the pulse duration and peak power can vary by 10 % or more in experimental systems, this result suggests that the experiments generate as many as $10^3 \times 10^3 = 10^6$ independent realizations and it may be necessary to simulate an ensemble with as many as 10^6 realizations to find a converged spectrum. We will show, however, that a much smaller ensemble with 5,000 or fewer realizations is sufficient to reproduce the experimentally-expected spectral power

density and bandwidth.

2.3.1 Simulation parameters The ensemble average is taken from realizations in the two-dimensional parameter space defined by the input pulse duration and the input pulse peak power. The parameter space is centered around the point with a 1 kW peak power and a 1 ps pulse duration and includes a 10 % variation in each dimension. Thus, the parameter space extends from 950 fs to 1050 fs in pulse duration and from 950 W to 1050 W in pulse peak power. Realizations are chosen 100 at a time. Each set of 100 realizations forms a uniform grid in the parameter space, such that realizations in each set are separated as far apart as possible. Successive sets are created by shifting the sampling grid so that no realization is repeated and each new set is as far away from previous sets as possible. We show this gridding scheme schematically in Fig. 2.10. Each set of 100 is averaged, and we repeated this 100-point sampling until we had 10^6 individual SC realizations, or 10^4 100-realization ensemble averages. Then, these 10^4 averages were averaged cumulatively to investigate the behavior of the ensemble as more realizations are included.

We do not include white Gaussian noise in our simulations. While adding white Gaussian noise does change the SC output spectrum that results from a particular set of input parameters, so does an extremely small change to one or both of the input parameters, which is what we achieve in our sampling. Moreover, the noise spectrum of the pulses in an experimental mid-IR SC source is not well characterized. Additionally, a small-scale test of 1000 realizations showed that results that included white Gaussian noise were statistically similar to results without noise. Since the statistical properties appear to be unchanged, we omitted white Gaussian noise in our simulations.

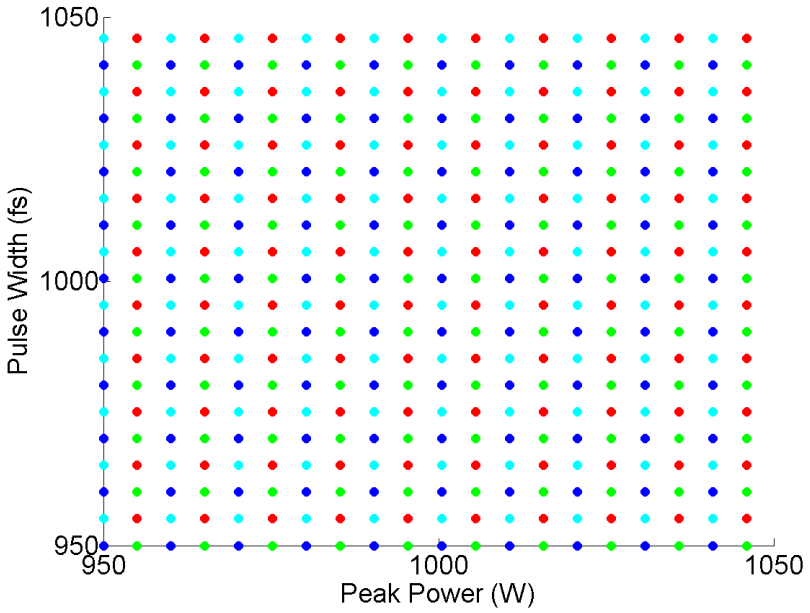

Figure 2.10: Uniform gridding scheme. Realizations indicated by the same color are averaged.

2.3.2 Spectral correlation in parameter space Figure 2.11 shows a typical supercontinuum output spectrum with the approximate delineation of the three wavelength regions. Region 1, the short wavelength region, from around 1.5 μm to 2.7 μm shows the least change as the pulse parameters vary. Region 1 represents energy formed by early four-wave mixing with a spectral shape determined primarily by material loss, which increases rapidly for wavelengths shorter than 2 μm, and by the four-wave mixing resonances. Region 2, the middle wavelength region, from around 2.7 μm to around 4.6 μm shows the most change as the pulse parameters vary slightly. However, while Region 2 shows a large amount of variation, the effect on the bandwidth is small, since most of the variation is due to a fine structure that varies rapidly with wavelength. Region 3, the long wavelength region, from around 4.6 μm and longer, changes rarely but significantly. The power spectrum in this region is due almost entirely to the longest-wavelength, highest-energy soliton and

has the greatest effect on the bandwidth of the SC output.

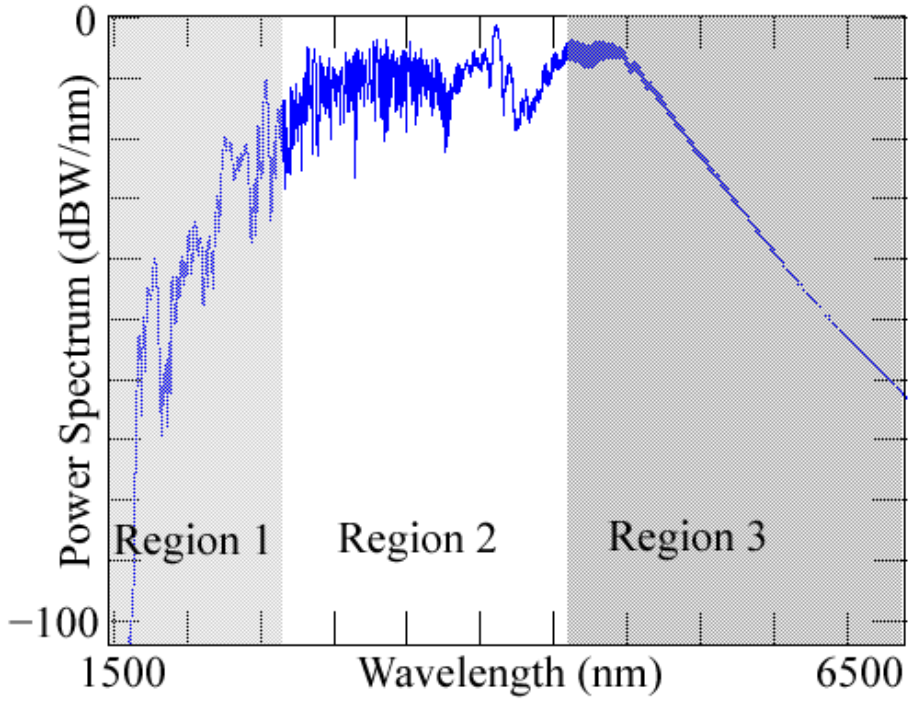

Figure 2.11: Example supercontinuum spectrum showing three regions.

In Fig. 2.12, we show the average Pearson correlation coefficient between realizations with different pulse parameters from the parameter space for the short and middle wavelength regions. The Pearson correlation coefficient is computed as

$$\rho = \frac{\sum_{\lambda=\lambda_1}^{\lambda_n}(X_\lambda - \bar{X})(Y_\lambda - \bar{Y})}{\left[\sum_{\lambda=\lambda_1}^{\lambda_n}(X_\lambda - \bar{X})^2 \sum_{\lambda=\lambda_1}^{\lambda_n}(Y_\lambda - \bar{Y})^2\right]^{1/2}}, \tag{2.4}$$

where X and Y are two different output spectra or output spectrum regions with corresponding mean values $\bar{X}$ and $\bar{Y}$, and X_λ and Y_λ are the values of those output spectra at a particular wavelength λ. For the short wavelength region, $\lambda_1 = 1000$ nm and

$\lambda_n = 2700$ nm. For the intermediate wavelength region, $\lambda_1 = 2700$ nm and $\lambda_n = 4600$ nm. In both cases, the values of λ are separated by 1 nm.

Figure 2.12(a) shows the average correlation coefficient for the short wavelength region and middle wavelength region between realizations where the input pulse peak power is varied by 0.1 W. Figure 2.12(b) shows the average correlation coefficient for the short wavelength region and middle wavelength region between realizations where the input pulse duration is varied by 0.1 fs. The average correlation coefficient is taken over 1000 realizations between 950 W and 1050 W for the peak power plots and over 1000 realizations between 950 fs and 1050 fs for the pulse duration plots. These values represent a 10% variation in pulse parameters for a 1 ps, 1 kW input pulse. The long correlation length for the short wavelength region is evident for both dimensions of the two-dimensional pulse parameter space. By contrast, the middle wavelength region has a very short correlation length in both peak power and duration, but we note that its correlation does not go to zero.

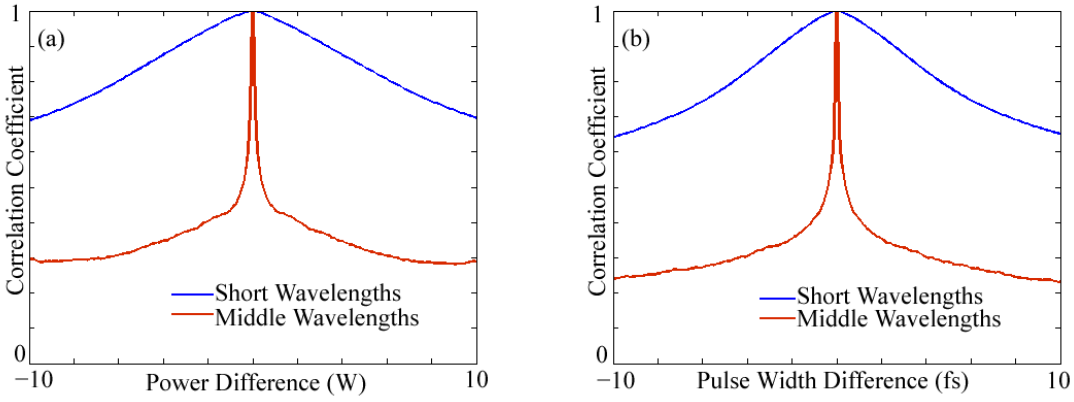

Figure 2.12: Average correlation coefficient for short and middle wavelength regions when (a) the peak power is varied and (b) when the pulse duration is varied.

2.3.3 Spectral convergence Figure 2.13 shows a typical single-shot SC output spectrum for an input pulse with a peak power of 1 kW and a pulse duration of 1 ps, which shows large fluctuations in output power, and the ensemble-averaged output spectrum for the full ensemble including 10^6 samples taken from the parameter space as described in Section 2.3.1. In addition to the large-scale fluctuations in output power present in the single-shot result, it is readily apparent that this single-shot result has a slightly larger bandwidth than the full ensemble — about 100 nm wider. This variability in the output spectrum and its bandwidth, as demonstrated here, is the main source of uncertainty in the single-shot results. We note that the short wavelength region still shows large, persistent fluctuations, even in the full ensemble average, which we attribute to periodic phase-matching of the four-wave mixing. Also visible in the ensemble-averaged result are some small-scale fluctuations in the middle wavelength region, particularly on the short wavelength side, which we attribute to residual soliton interactions, as we will discuss later.

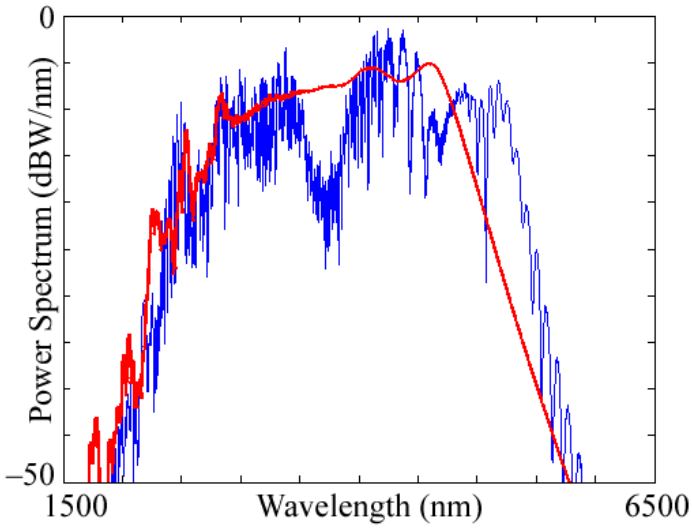

Figure 2.13: Single-shot simulation output (blue) and full 10^6 ensemble average output (red).

As mentioned previously, the variations in wavelength region 3 are most responsible for the variability in the output bandwidth. Figure 2.14 shows a comparison of two single-shot output spectra, which are similar for most wavelengths except in the long wavelength region. The difference in bandwidth between these two spectra is about 700 nm. The large bandwidth of the spectrum shown in blue is due to an optical rogue wave [31] event. These events occur rarely, but often enough to affect the ensemble average. The impact of rogue events on the bandwidth is not made evident by the logarithmic scale of the ordinate axis. The next figure better clarifies the behavior.

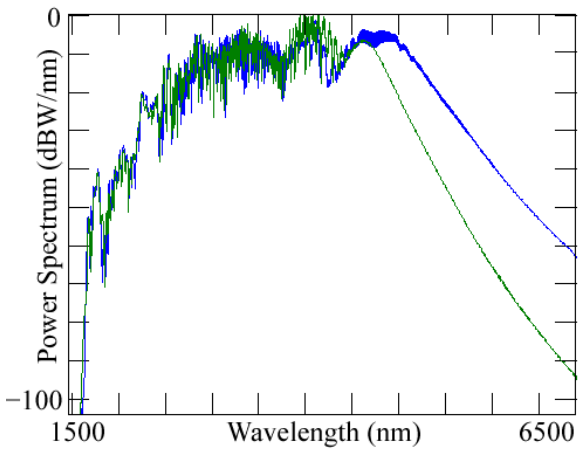

Figure 2.14: Comparison of output spectra with different bandwidths: 2.5 μm (green) and 3.2 μm (blue).

In Fig. 2.15, we show a histogram of the output bandwidth for 10^5 realizations using 50 bins. This distribution is bimodal. Most output spectra in the ensemble have a bandwidth around 2.8 μm, while a smaller group of bandwidths is clustered around 2.5 μm. However, even in this (relatively) limited sample space of noise-free simulations, spectra with bandwidths greater than 3.2 μm, more than 25% greater than the average, exist in the ensemble.

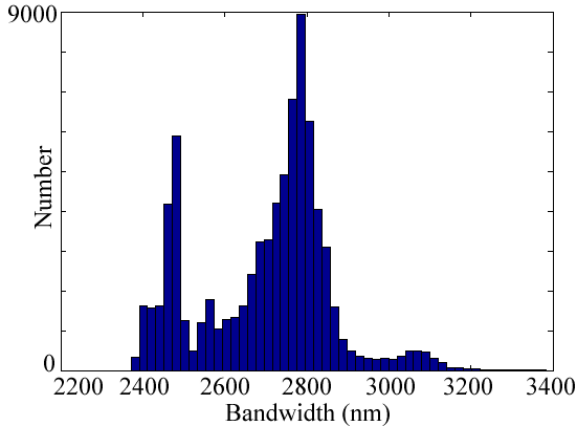

Figure 2.15: Histogram of output bandwidths.

It has been shown [22, 28], that for SC systems with soliton numbers greater than about $N = 10$, the mutual coherence between different realizations of SC generation will decrease rapidly. Hence, the wavelengths of the SC outputs will be largely uncorrelated from shot-to shot. The large soliton number for this system ($N \approx 30$) is consistent with the great sensitivity in the output spectrum that we observe when the input pulse duration and peak power change. At the same time, the number is small enough that the residual correlations remain visible. We attribute the bumps that are visible in the middle range of wavelengths in the 10^6 ensemble-averaged spectrum in Fig. 2.13 to these residual correlations. In Fig. 2.16, we show the spectrogram evolution for a single realization, and in Fig. 2.17, we show the average spectrogram evolution for an average of 1000 realizations. The solitons that are visible in a single realization remain perceptible in the average, although greatly diminished in amplitude relative to the background.

2.3.4 Statistical characterization The location and amplitude of the large-scale, fast fluctuations in the spectrum appear to be randomly varying from one realization to the next, although, as just noted, appearances are deceiving. If the samples from the parameter

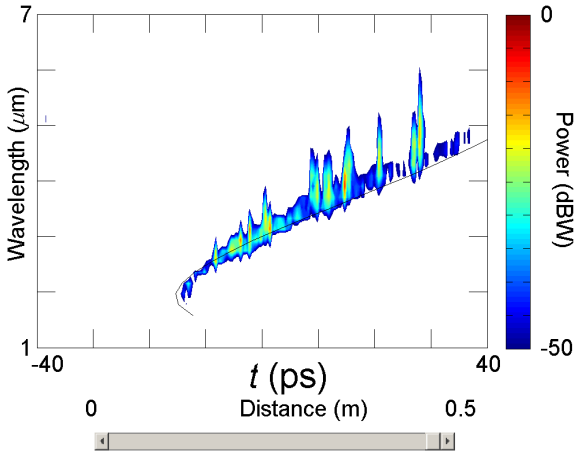

Figure 2.16: Single-shot spectrogram.

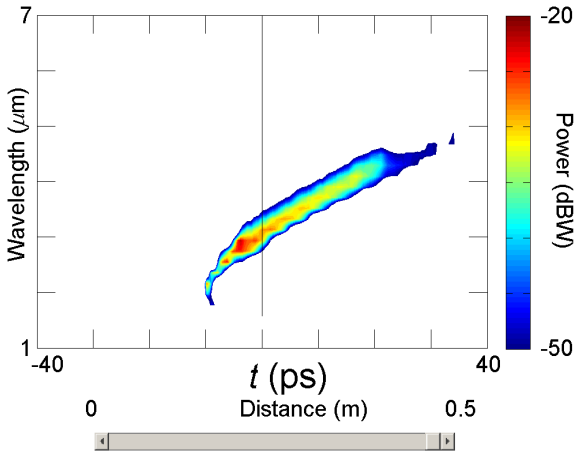

Figure 2.17: Average spectrogram for 1000 samples.

space were statistically uncorrelated, we would expect the variance of these fluctuations to reduce with an increasing number of samples in the ensemble proportional to N^{-1}, where N is the number of samples in the ensemble. From the plots of the correlation coefficient in Section 3, we might expect that the highly uncorrelated middle wavelength region would show a reduction in variance that follows this rule. The short wavelength region has a much

broader correlation function, and so we would expect the variance of the fluctuations in this region to reduce more slowly as more realizations are included in the ensemble average.

To test this hypothesis, we computed the variance of the fluctuations in both regions, using the final ensemble-averaged spectrum as a basis for comparison. The variance of the fluctuations in a spectrum is computed as

$$\sigma^2 = \frac{1}{n} \sum_{\lambda=\lambda_1}^{\lambda_n} \left[(X_\lambda - \overline{X_\lambda}) - \mu \right]^2, \tag{2.5}$$

where n is the number of wavelengths, or the size of the region, under consideration, X_λ is the amplitude of the spectrum at wavelength λ, and $\overline{X_\lambda}$ is the amplitude of the full ensemble-averaged spectrum at that wavelength, and μ is the mean value of $X_\lambda - \overline{X_\lambda}$. For the short wavelength region, $\lambda_1 = 1000$ nm and $\lambda_n = 2700$ nm. For the intermediate wavelength region, $\lambda_1 = 2700$ nm and $\lambda_n = 4600$ nm. Again, the values of λ are separated by 1 nm.

The variances of the fluctuations in the short and middle wavelength regions are shown in Fig. 2.18 and Fig. 2.19, respectively. In both cases, the variance decreases at a similar rate, approximately equal to $N^{-5/6}$. The variance decreases rapidly as the number of samples approaches 10^6 because the data are being compared to the ensemble average with 10^6 samples. While both regions have a similar overall rate of decrease, the decrease in variance is relatively smooth for the middle wavelength region compared to the short wavelength region. The variance of the fluctuations in the short wavelength region decreases in jumps, with a seemingly self-similar pattern that repeats approximately two times every decade. We attribute the lack of smoothness in this case to the high correlation in this wavelength range and the residual spectral structure that does not average out, which is due to a combination of material loss and four-wave mixing resonances.

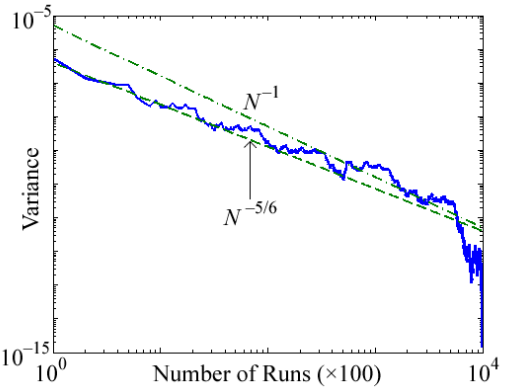

Figure 2.18: Variance of the fluctuations in the short wavelength region. Lines corresponding to $N^{-5/6}$ and N^{-1} are also shown for comparison.

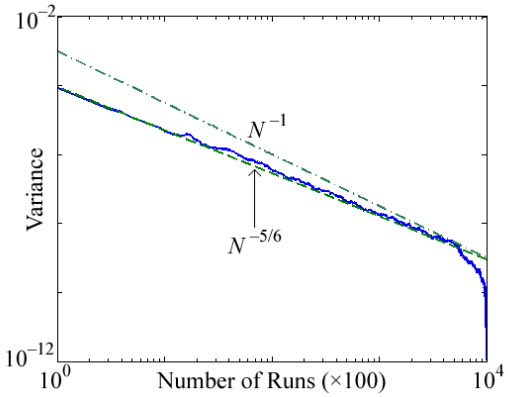

Figure 2.19: Variance of the fluctuations in the middle wavelength region. Lines corresponding to $N^{-5/6}$ and N^{-1} are also shown for comparison.

The $N^{-5/6}$ rate of reduction for the middle wavelength region implies that with 5000 samples, the variance of the fluctuations has reduced by approximately two orders of magnitude from its original value. This reduction is sufficient to yield a good quantitative estimate of the shape, smoothness, and amplitude of the experimentally-expected output spectrum. A comparison of the ensemble average including 5000 realizations and 10^6 realizations is shown in Fig. 2.20. The corresponding spectra match almost exactly. The differences between the output spectra are small scale fluctuations that are almost imperceptible.

Because the rate of decrease for the middle wavelength region is slower than N^{-1}, we infer that there are residual correlations between the realizations due to fluctuations as a function of wavelength that never average out. These residual fluctuations are visible in Fig. 2.20 in both large-scale fluctuations that vary slowly as a function of wavelength and small-scale fluctuations that vary rapidly as a function of wavelength. We attribute these residual correlations to the restricted number of solitons that make up the spectrum and

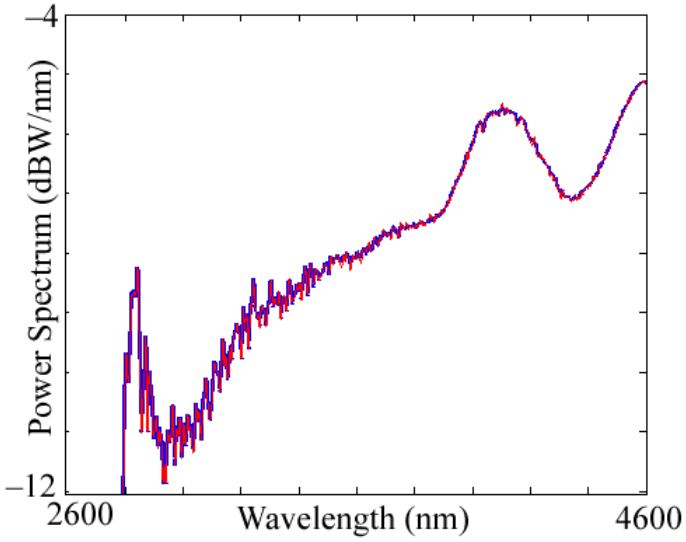

Figure 2.20: Ensemble average output for 5000 samples (red) and 10^6 samples (blue).

are visible in Figs. 2.16 and 2.17. The presence of these residual correlations is consistent with the Pearson correlation coefficients in Fig. 2.12. The correlation coefficient does not approach zero and diminishes slowly for separations greater than about $\Delta\tau = \pm 2$ fs in pulse duration or $\Delta P = \pm 2$ W in pulse peak power.

2.3.5 Long wavelengths and bandwidth convergence Figure 2.21 shows the bandwidth of the ensemble-averaged output spectrum as the number of samples in the ensemble increases. While the bandwidth comes within 5 nm of its final, converged value after about 1000 realizations, it does not reach its final value until around 5000 realizations. Even though there is still some settling down after 5000 realizations, the fluctuation in the bandwidth is small after that point. This value of 5000 realizations is consistent with the convergence of the middle wavelength region of the spectrum as described in the previous section. We also found similar bandwidths using different sets of 5000 realizations.

In comparing Fig. 2.15, the histogram of bandwidths, and Fig. 2.21, we find that

the bandwidth of the average spectrum is not the same as the average bandwidth. The average bandwidth is around 2700 nm, while the bandwidth of the average spectrum is close to 2900 nm. This difference indicates that, as expected, the ensemble average behavior in the long-wavelength region is dominated by the large-bandwidth rogue events, even though they occur much less frequently than the average-bandwidth output spectra. It is the bandwidth of the average spectrum that would be observed in an experiment.

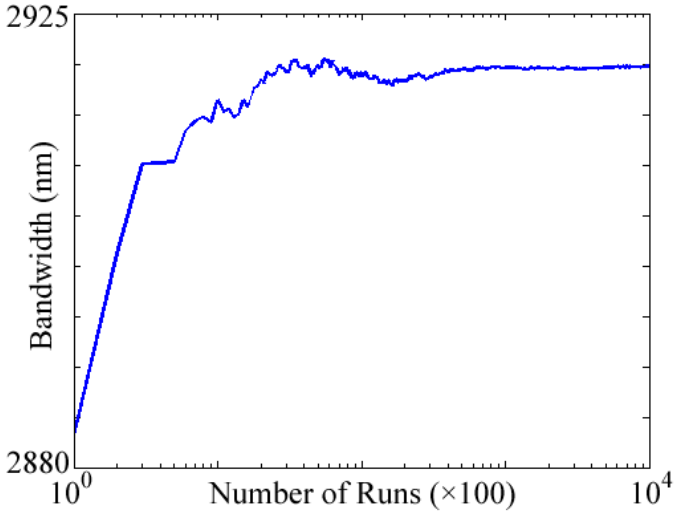

Figure 2.21: Average bandwidth versus number of samples in the ensemble average.

Chapter 3

Moth-eye structures

It has been known since the time of Lord Rayleigh that microscale structures on the surface of optical interfaces are effective at reducing Fresnel reflections [32]. Periodic antireflective (AR) microstructures are called "moth-eye" structures because of their similarity to the microstructures on the eyes of nocturnal moths [33]. Figure **??** compares scanning electron microscope (SEM) images of the so-called "corneal nipple array" from a moth's compound eye and a moth-eye structure imprinted onto a chalcogenide optical fiber.

Moth-eye structures are a biomimetic microstructured AR surface structure that are effective at reducing Fresnel reflections [34]. In the long wavelength limit, they work by providing a gradual change of the effective refractive index as light propagates across the air-glass interface. They are especially useful for high-index materials, which includes most mid-IR materials, such as chalcogenide glasses. Reducing Fresnel reflections from optical interfaces is important in mid-IR applications where high power and low loss are needed. High power laser radiation that reflects from interfaces can damage instruments, while insertion or coupling losses can be major contributors to overall losses in a system [35]. Hence, mid-IR systems can greatly benefit by using moth-eye structures to reduce reflections from and to increase transmission through interfaces. They are useful in a number

of applications, including laser systems [35], photovoltaics [36], LEDs [37], automotive glass [38], electronics displays [39], and fiber optics [8].

Sanghera et al. [8] and MacLeod et al. [40] recently demonstrated a direct stamping method for imprinting these moth-eye structures on the end-faces of chalcogenide optical fibers, where AR interfaces are particularly useful because of the large refractive index difference between air and As_2S_3 ($\sim$2.45 at a wavelength of $\lambda = 2$ μm). The direct stamping method allows structures to be accurately replicated, and the reflection as a function of wavelength depends sensitively on the structures and their parameters [9], which means that they must be accurately modeled. Because in the structures studied in this work, the microstructure feature dimensions are on the same order as the wavelength of the incoming radiation ($\sim$1 μm), the light in adjacent features interacts, and thus neither the long-wavelength average refractive index model nor the short-wavelength ray optics model is appropriate to describe transmission through moth-eye structures. Hence, they must be modeled using rigorous computational methods [41], such as the finite-element method (FEM), the finite-difference time-domain method (FDTD) [42, 43], or rigorous coupled-wave analysis (RCWA) [44,45], where the results become exact in principle as the grid size and step size tend to zero (FEM and FDTD) or the number of harmonics becomes infinite (RCWA). We have simulated moth-eye structures using three methods, FEM, FDTD and RCWA. We find that they agree perfectly, but that RCWA is the fastest and most accurate method.

Moth-eye structures have several advantages over traditional thin-film AR coatings, including environmental tolerance, surface adhesion, single material fabrication, minimal surface preparation, and self-cleaning via the lotus effect [8, 38]. Additionally, it has been shown in recent years that in many cases periodic moth-eye structures have a higher laser-induced damage threshold (LIDT) than do traditional AR-coated surfaces [46–48].

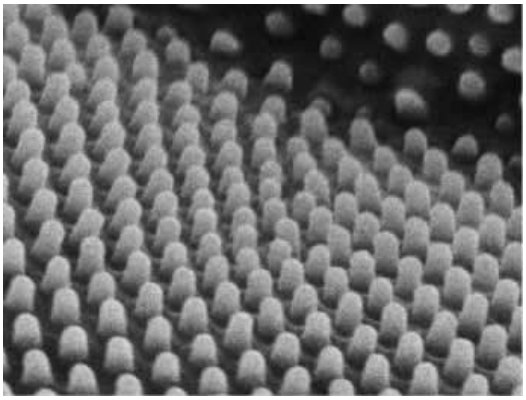

(**a**) SEM of a moth's eye (from [49]).

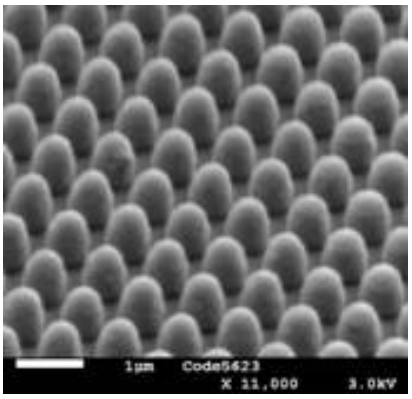

(**b**) Moth-eye structure (from [8]).

Figure 3.1: Comparison of a moth's eye and a moth-eye structure.

3.1 Comparison of theory and experiment

The preliminary goal of the work described in this section is to create and validate a theoretical model that agrees with the results for a particular moth-eye structure that was experimental studied at the Naval Research Laboratory by Sanghera et al. [8]. We calculate the transmission of the structured surface by simulating a plane-wave incident upon the structured surface using the open-source finite-difference time-domain (FDTD) computer software MEEP [50]. The simulation propagates a wave-packet of specific bandwidth through the microstructure and then calculates the transmission and reflection spectra by taking a harmonic transform of the time-domain flux through measurement surfaces that are situated above and below the microstructured surface. We utilize the periodicity of the structure and only solve for the fields in a single unit cell, using Floquet-Bloch boundary conditions. The calculated transmission spectra have been verified by comparison with the commercial software package DiffractMOD by RSOFT, which uses the rigorous coupled wave algorithm (RCWA).

The experimental shape is modeled by a truncated cone with a hemispheric cap that is

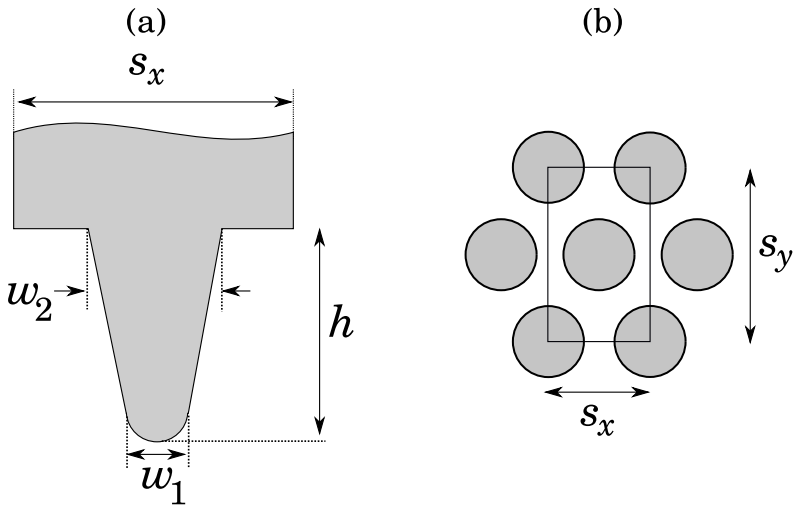

Figure 3.2: Schematic view of a moth-eye cone structure with parameters. (a) Side cross-section view; (b) top view showing a unit cell.

fully determined by specifying the cone height, h; the base diameter, w_2; the tip diameter, w_1; and the lattice constant of the packing, s_x. Since the features are hexagonally packed, $s_y = \sqrt{3}s_x$. These geometric parameters are shown diagrammatically in Fig. 3.2. The cone approximation to the experimentally implemented feature has parameters $w_1 = 0.2$ μm, $w_2 = 0.7$ μm, and $h = 0.9$ μm. For all theoretical models, we set the refractive index n of As_2S_3 to be equal to $n = 2.45$, which is a good approximation to the experimentally-measured value over the wavelength range of interest.

The calculated transmission spectra is shown in Fig. 3.3 for light that is coupled into and out of an optical fiber. The spectra are very similar at longer wavelengths and differ for shorter wavelengths for reasons that will be explained shortly. The output coupling exhibits a sharp falloff at short wavelengths, while the input coupling does not. The transition from high to low transmission as the wavelength decreases is called the diffraction edge, is sharp, and occurs at 1.9 μm for this structure.

Figure 3.3 also shows that the experimentally-measured transmission for light coupled

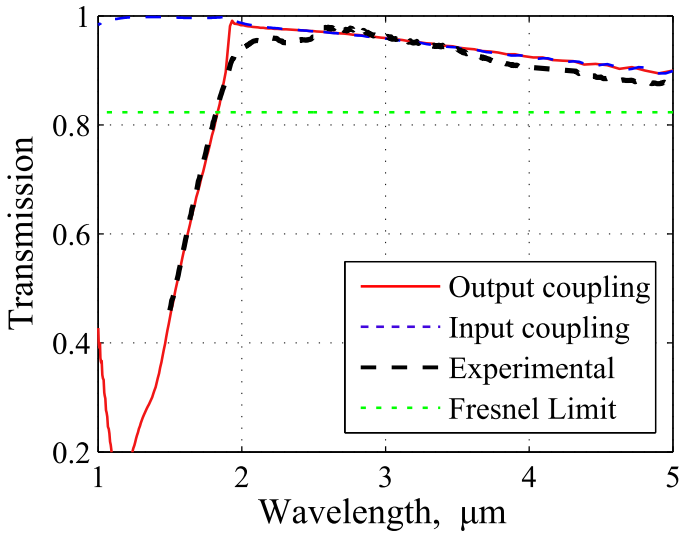

Figure 3.3: The theoretical transmission spectra of light coupled into and coupled out of the fiber. The experimental transmission spectra of light coupled out of the fiber is also shown. The Fresnel limit is the transmission spectra from a plane-wave coupling into or out of a fiber with a flat end-face.

out of the fiber and the drop-off in transmission for shorter wavelengths match the theoretical result. The measured transmission spectrum is somewhat lower at longer wavelengths, which could be caused by a slightly different cone shape in the experimental system than in our theoretical model and/or by material losses, which are not included in our theoretical model.

Finally, Fig. 3.3 shows the transmission through a bare fiber end-face with no AR structure for comparison. The Fresnel-limited transmission depends only on the refractive indices of the incident and transmitting medium and, in this case, is approximately 83%.

3.1.1 Coupling into and out of a fiber The coupling of light into the fiber and the transmission out of the fiber are two different problems, as schematically shown in Fig. 3.4(a). For long wavelengths, the behavior of both input and output coupling can be expected to be similar, as the electro-magnetic field will average over the moth-eye surface,

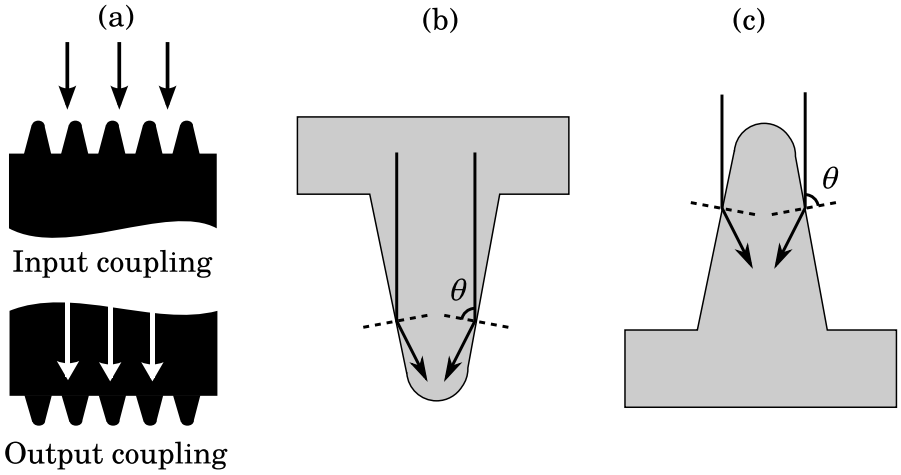

Figure 3.4: (a) Coupling of light into and out of the fiber represented graphically. The ray-optics pictures of light coupling (b) out of the structure, and (c) into the structure.

effectively homogenizing the refractive index transition and leading to similar transmission properties in both directions.

For shorter wavelengths, we expect the transmission properties to be very different. In the ray-optics limit, normally incident light will be totally internally reflected inside the cones in the output coupling case, whereas light will be refracted directly into the fiber in the input coupling case, as shown in Figs. 3.4(b) and 3.4(c). Total internal reflection occurs when the angle that the incident light ray makes with the cone surface, θ, is greater than the critical angle, 24°, as is the case with all of the practical cone designs considered.

This argument gives an intuitive picture of how a structured surface can yield very different behavior for light coupled into and out of the high index material. However, the coupling at wavelengths close to the size of the structure is complicated due to the interaction of the electromagnetic field in adjacent cone structures. The wavelength at which the input and output coupling differ is called the diffraction edge, because for wavelengths below the diffraction edge, diffracted orders greater than zero exist in the transmitted spec-

trum. Full numerical simulations of Maxwell's equations are therefore required to obtain a qualitative picture of the transmission spectra as well as a quantitative result.

3.2 Changing the dimensions

Next, we investigate changing the dimensions of the truncated cone to determine the effect on the transmission spectrum. We vary each parameter independently, starting with the tip width.

3.2.1 Tip width The calculated transmission spectra for input and output coupling for different values of the cone tip diameter, w_1, are shown in Fig. 3.5. All other parameters are kept fixed at $w_2 = 0.7$ μm, $h = 0.9$ μm, $s_x = 0.92$ μm, and $s_y = 1.59$ μm.

As the cone tip diameter is increased from $w_1 = 0.1$ μm to $w_1 = 0.7$ μm, the transmission for wavelengths above 3.5 μm increases. However, for wavelengths around 2.8 μm, the transmission correspondingly decreases. For output coupling, the transmission drop-off near 2 μm does not change significantly for different values of w_1. For input coupling, the transmission decreases below 2 μm as the tip diameter increases.

3.2.2 Base width In the second parameter study, we varied the diameter of the base of the cone, keeping the other parameters fixed at $w_1 = 0.2$ μm, $h = 0.9$ μm, and $s_x = 0.92$ μm. The resulting transmission spectra versus wavelength are shown in Fig. 3.6. We see that for very narrow cones, with $w_2 = 0.3$ μm, the transmission is only slightly increased above the Fresnel limit of a flat interface, which is approximately 83%. For both input and output coupling the slopes of the transmission spectra become increasingly steep, decreasing from almost 100% transmission near 2.5 μm to around 92% transmission near 5 μm at the largest base diameter that we consider, $w_2 = 0.9$ μm, where the base of

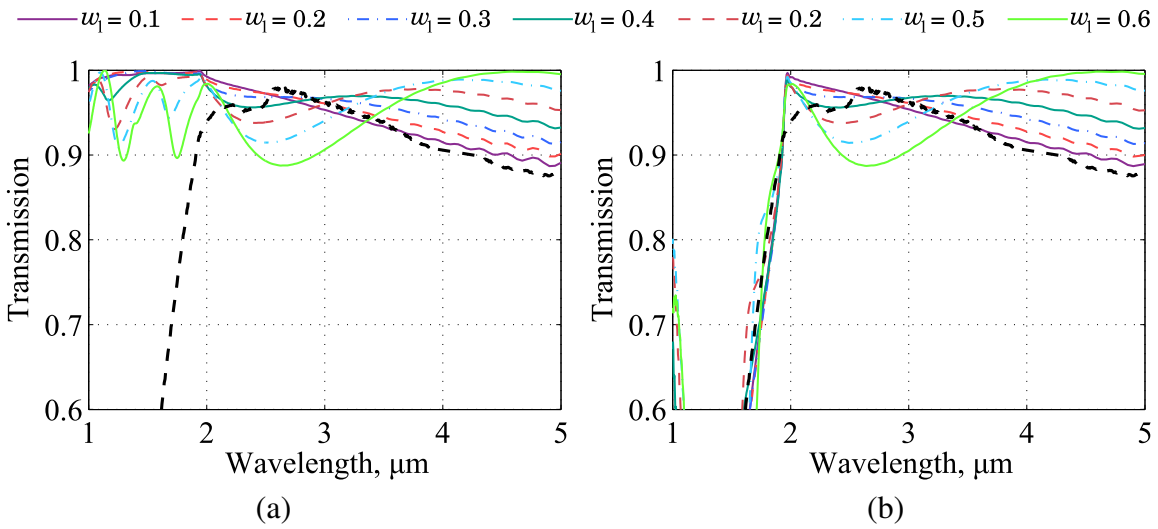

Figure 3.5: The transmission spectra of light coupled (a) into and (b) out of the fiber versus the cone tip diameter w_1. The other geometric parameters are $w_2 = 0.7$ μm, $h = 0.9$ μm, and $s_x = 0.92$ μm.

the cones would be almost touching. For input coupling we see that as w_2 increases, the transmission increases for all wavelengths. Furthermore, for output coupling, we find that as w_2 increases, the cutoff at 2 μm becomes stronger.

3.2.3 Height The transmission spectra versus wavelength for different cone heights, h, keeping the other parameters fixed, are shown in Fig. 3.7. The transmission above 3.5 μm increases as the cone height increases; however, the transmission also decreases slightly with increasing h near a wavelength of 3 μm. The same behavior is seen for both input and output coupling. The height does not greatly affect the transmission below 2 μm for input coupling; for output coupling the transmission increases, although it is still considerably below the Fresnel limit of 83%, and the sharp cutoff is still present.

3.2.4 Period The final geometric parameter that we change in our model is the lattice spacing or the period of the cones, s_x. The lattice packing is kept hexagonal; deviations

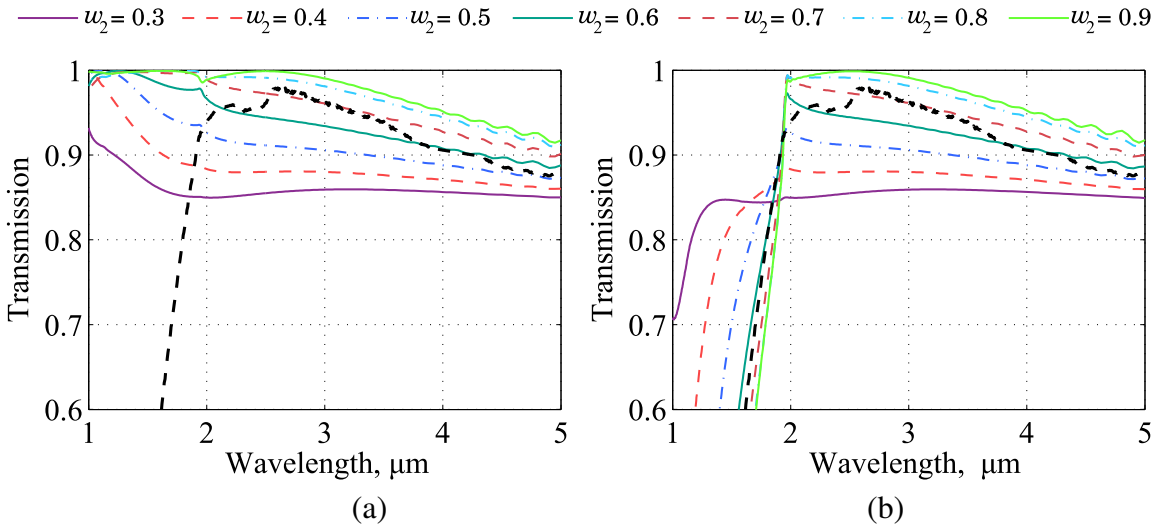

Figure 3.6: The transmission spectra of light coupled (a) into and (b) out of the fiber versus the cone bottom diameter w_2. The other geometric parameters are $w_1 = 0.2$ μm, $h = 0.9$ μm, and $s_x = 0.92$ μm.

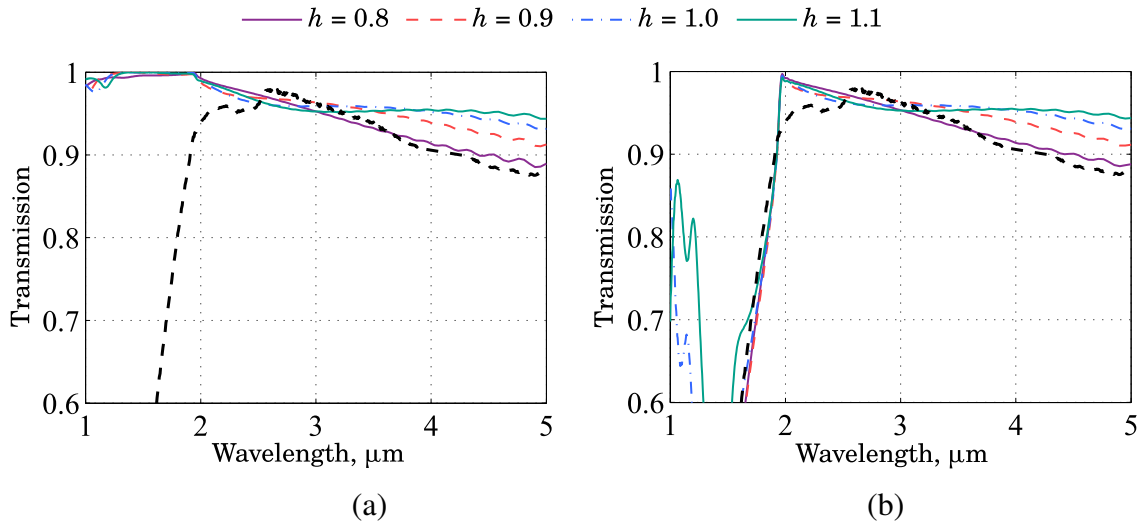

Figure 3.7: The transmission spectra of light coupled (a) into and (b) out of the fiber versus the cone height h.

from this packing by choosing s_y differently would cause different polarizations of light to have different transmission spectra. The results are shown in Fig. 3.8. We find that the transmission increases with decreasing s_x. This result qualitatively agrees with the re-

sults of changing the cone base diameter: In both cases, the packing density of the cones increases, causing the interaction of the fields between cones to increase, which in turn increases the resulting transmission. The results for output coupling are shown in Fig. 3.8(b). In this case, we find that changing the lattice constant changes the cut-off or diffraction edge wavelength, which increases as s_x increases.

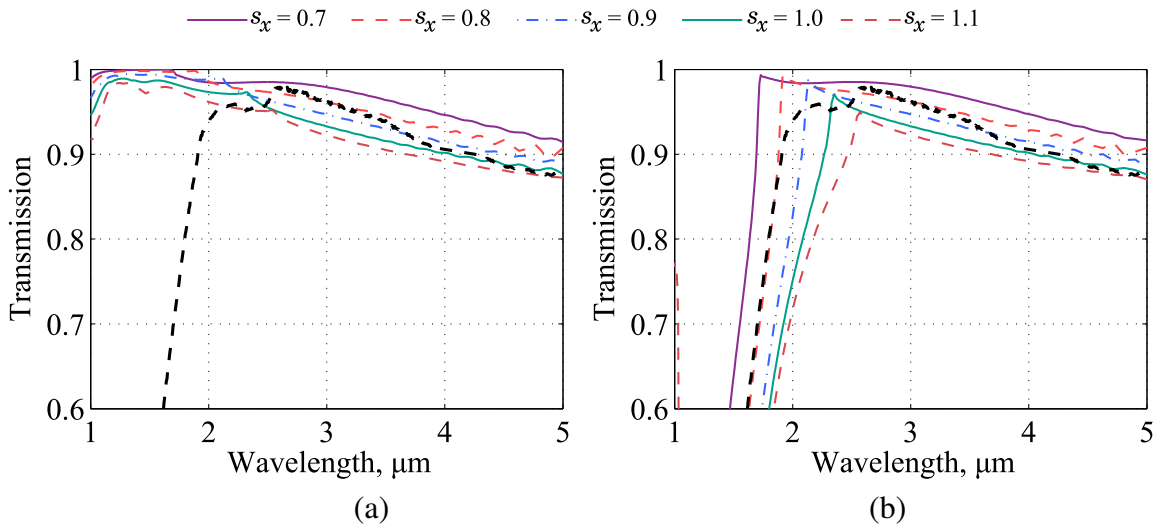

Figure 3.8: The transmission spectra of light coupled (a) into and (b) out of the fiber versus the cone hexagonal packing spacing s_x.

3.3 Angle of incidence

The effect of changing the angle of incidence of the input plane wave is shown in Fig. 3.9 for angles up to 30° for the same moth-eye structure that was discussed in the previous section. For input coupling, the transmission spectra is almost unaffected by changes in the angle of incidence. This result makes sense conceptually, as argued previously from the ray picture in Fig. 3.4(c). For output coupling, the transmission drops significantly for

angles of incidence above $10°$, going to zero for wavelengths above 2 μm for an incidence angle of $30°$.

For single mode fibers the low transmission at non-normal incidence for output coupling would not be a problem since the angle of incidence for the fundamental mode would be close to normal; however, for multimode fibers this issue should be taken into consideration.

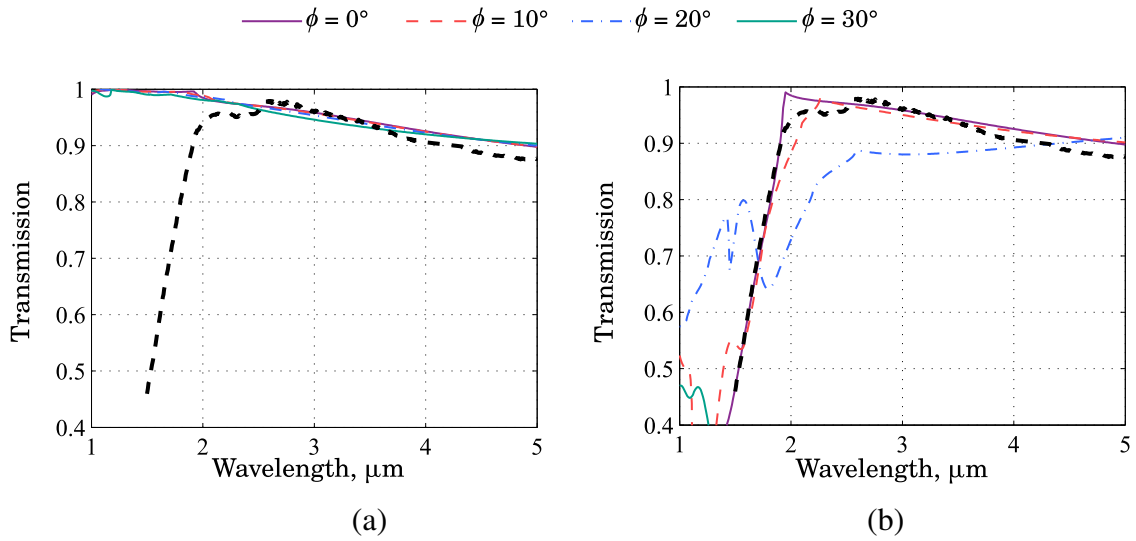

Figure 3.9: The transmission spectra of light coupled (a) into and (b) out of the fiber versus the incidence angle of the input plane-wave, ϕ.

3.4 Changing the shape

In this section, we study the effect of changing the shape of the moth-eye structure element. The shapes we study are a half-ellipsoidal shape, a sinusoidal shape, and a truncated pyramid. The truncated pyramid element is a flat-sided square pyramid with the top cut off. The half-ellipsoid structure is the upper half of an ellipsoid oriented along the z-axis,

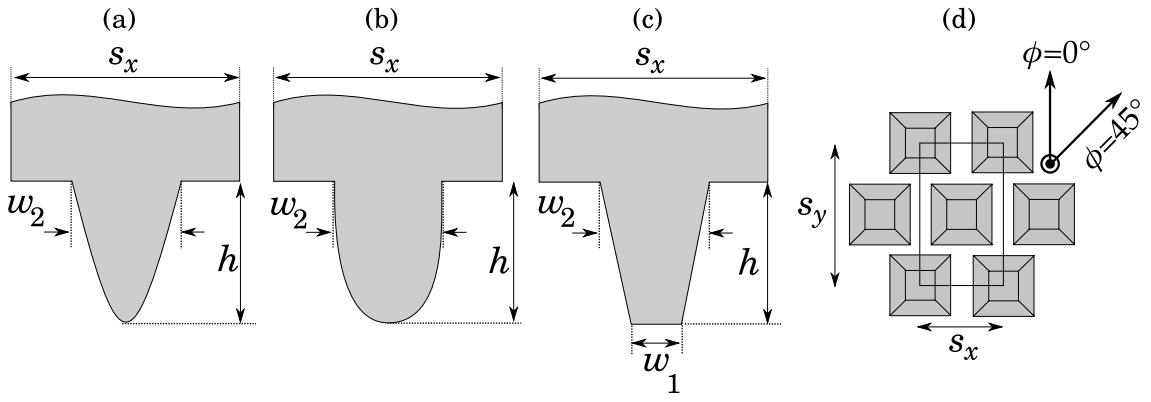

Figure 3.10: Cross-section of (a) a sinusoidal structure, (b) a half-ellipsoid structure, and (c) a truncated pyramid structure. (d) The pyramidal surface from the top, showing the polarization angles used in the simulations.

whose height is given by the equation

$$z(x,y) = h\left[1 - \left(\frac{x}{w_2/2}\right)^2 - \left(\frac{y}{w_2/2}\right)^2\right]^{1/2}, \tag{3.1}$$

where x and y are the axes parallel to the surface, z is the height perpendicular to the surface, h is the element height, and w_2 is the base width. The sinusoidal shape is given by the upper half of a cosine rotated around the z-axis, which has a height

$$z(x,y) = h\cos\left\{\frac{\pi}{w_2}\left[\left(\frac{x}{w_2/2}\right)^2 + \left(\frac{y}{w_2/2}\right)^2\right]^{1/2}\right\}, \tag{3.2}$$

where again x and y denote the axes that are parallel to the surface, z denotes the height perpendicular to the surface, h is the element height, and w_2 is the base width. We show cross sections of each feature shape in Fig. 3.10(a)–(c).

3.4.1 Positive structures First, we studied positive structures formed from these element shapes. Positive structures correspond to the gray areas in Fig. 3.10 being As_2S_3, with

the white areas (background) being air. We compare the transmission spectra for positive elements of three different heights $h = 0.8$ μm, 1.2 μm, and 1.6 μm and two base widths of $w_2 = 0.7$ μm and 0.9 μm. The pyramidal element has an extra parameter compared to the sinusoidal and half-ellipsoid elements, which is the top width w_1; for the following calculations, we set $w_1 = 0.15$ μm. The pyramidal structure is also not rotationally symmetric about the z-axis, unlike the other two structures, and will therefore have different transmission properties depending on the polarization of the incident light.

The calculated transmission spectra in the case of output coupling for the sinusoidal and half-ellipsoid surfaces are shown in Fig. 3.11(a) and Fig. 3.11(b) respectively. For the sinusoidal surface, the transmission is greater for larger base widths. The transmission is generally flatter for taller elements, although there is little change between $h = 1.2$ μm and $h = 1.6$ μm. For the half-ellipsoid surface, the transmission is greater for larger base widths and is flatter for taller elements, and the highest transmission is obtained when the element is widest and has a height $h = 1.2$ μm or $h = 1.6$ μm. However, for the half-ellipsoid surface with $w_2 = 0.7$ μm, as the height is increased, the transmission actually drops below the transmission for shorter elements. A similar dip occurs with the sinusoid surface, but it is less significant.

The calculated transmission spectra for the pyramidal surface are shown in Fig. 3.12(a). The highest and widest pyramidal structure of $h = 1.6$ μm and $w_2 = 0.9$ μm performs the best of all the shapes considered and has a transmission of almost unity across the wavelength range $\lambda = 2$–5 μm.

Figure 3.12(b) shows the transmission for different polarization states of the incoming electric field. A polarization angle of $\phi = 0^\circ$ corresponds to the electric field parallel to the sides of the base of the pyramidal and a polarization angle of $\phi = 45^\circ$ corresponds to the electric field aligned diagonally to the base of the pyramidal, as shown in Fig. 3.10(d). The

transmission drops slightly when $\phi = 45°$ compared to when $\phi = 0°$. We expect that the transmission for all other polarizations lies in between these extreme cases.

In most cases, we found that increasing the base width and height of the element increased the transmission across the wavelength range. However, this behavior was not found for all element shapes in all height ranges; for example, the transmission for the half-ellipsoid with base width of $w_2 = 0.7$ μm is worse for taller elements. Also, for both the sinusoidal and half-ellipsoid elements, there is no improvement in transmission when the height increases from $h = 1.2$ μm to $h = 1.6$ μm. In fact, the transmission only increases for the pyramidal element with a base width $w_2 = 0.9$ μm when the height is increased from $h = 1.2$ μm to $h = 1.6$ μm. For the tallest and widest pyramid shape, the transmission is greater than 99.5% when the polarization angle $\phi = 0°$ and 99% when $\phi = 45°$ over the wavelength range $\lambda = 2$–5 μm. This transmission is the highest for all element shapes considered; however, with shorter element heights, the transmission for the pyramidal shape is not better than the other structures at longer wavelengths.

Different shapes have significantly different transmission spectra, even for two relatively similar smooth shapes like the sinusoid and the half-ellipsoid. Therefore, the exact shape of the elements is required to match experimental and theoretical calculations.

3.4.2 Negative structures Here, we consider two different negative structure shapes, sinusoidal and half-ellipsoid holes, which are shown schematically in Fig. 3.13. These are similar to those as considered previously for positive surfaces, and the shapes are again specified by Eqs. 3.3 and 3.2; however, now z specifies the depth of the hole below the surface, rather than the height above it.

The holes are parameterized in the same way as the bumps, using the base width, w_2, and the depth, h. The lattice parameter is the same as previously used, $s_x = 0.9$ μm, and

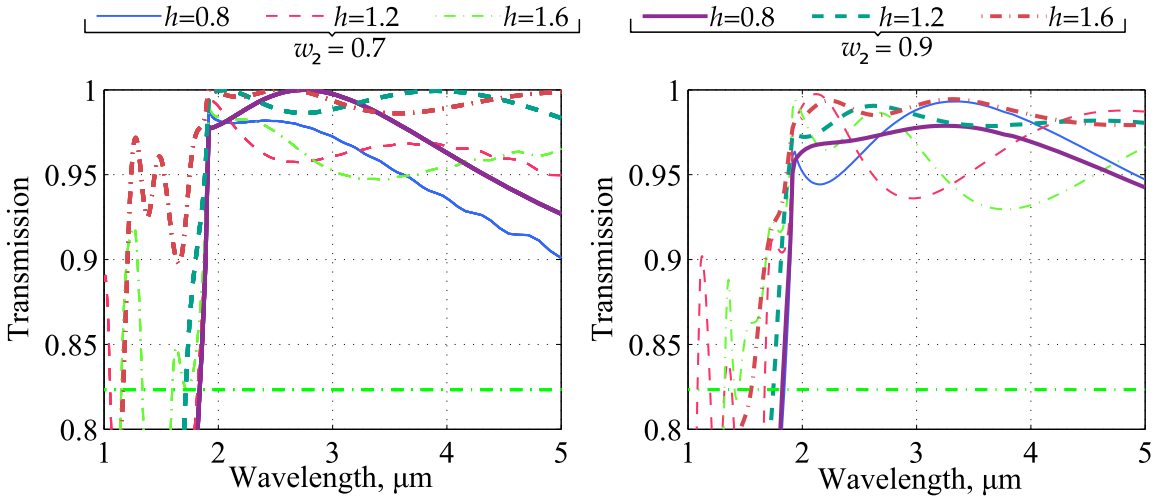

Figure 3.11: The theoretical transmission spectra through a surface consisting of positive (a) sinusoidal structures and (b) ellipsoid structures, both with $w_2 = 0.7$ μm (thin lines) and $w_2 = 0.9$ μm (thick lines). The Fresnel transmission at around 83% is also shown for reference in both figures.

the holes are again hexagonally packed.

The results for the transmission in the case of coupling out of the fiber for the sinusoid and half-ellipsoid holes is shown in Figs. 3.14(a) and 3.14(b) respectively. The transmission is higher for the holes with width $w_2 = 0.9$ μm than the holes with $w_2 = 0.7$ μm for both shapes. The transmission also increased as the width increased for the positive surface, but this increase is even more significant here. Increasing the hole depth does not significantly increase the transmission for most shapes. The notable exception is the half-ellipsoid surface with $w_2 = 0.9$ μm, where the transmission increases markedly as the hole depth increases, reaching a transmission of almost unity across the wavelength range above $\lambda = 2$ μm for the deepest hole considered.

The surface with sinusoidal holes has a cut-off that is around 1.2 μm rather than 1.9 μm, as is seen in the positive surface case, leading to a higher transmission in the wavelength range $\lambda = 1.2$–1.9 μm for the sinusoidal surface, so that for the tallest and

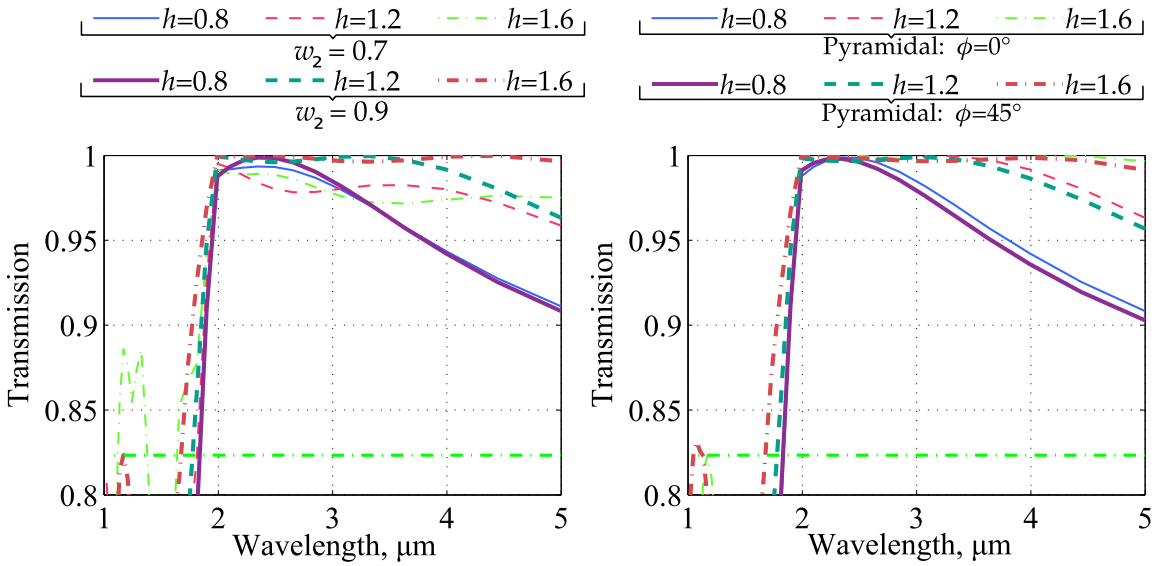

Figure 3.12: The theoretical transmission spectra for a surface with positive pyramidal structures with $w_1 = 0.15$ μm, with (a) the electric field polarized fixed at $\phi = 0$ and the parameters $w_2 = 0.7$ μm (thin lines) and $w_2 = 0.9$ μm (thick lines); (b) the incident electric field polarized at $\phi = 0$ (thin lines) and $\phi = 45°$ (thick lines) and the base width fixed at $w_2 = 0.9$ μm. The Fresnel transmission at around 83% is also shown for reference in both figures.

widest hole the transmission remains above 95% when $\lambda > 1.3$ μm. This increased cut-off is notable as the cut-off is tied to the periodicity of the lattice, and is not changed by any other factor for the positive surfaces. The tallest and widest half-ellipsoid holes also display an increased transmission in the cut-off region, as compared to the positive surface, only decreasing below 85% for wavelengths below 1.3 μm.

The calculated transmission for coupling into the fiber for the two negative shapes is shown in Figs. 3.15(a) and 3.15(b) respectively. The transmission is the same as for coupling out of the fiber at wavelengths above 2 μm, but the spectra for input and output coupling diverge below 2 μm.

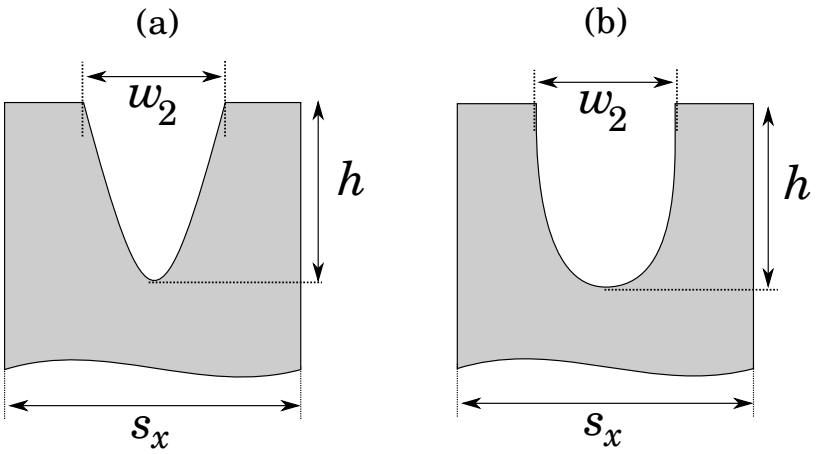

Figure 3.13: Schematic view of a negative structured surface consisting of holes with (a) sinusoidal and (b) half-ellipsoid shapes.

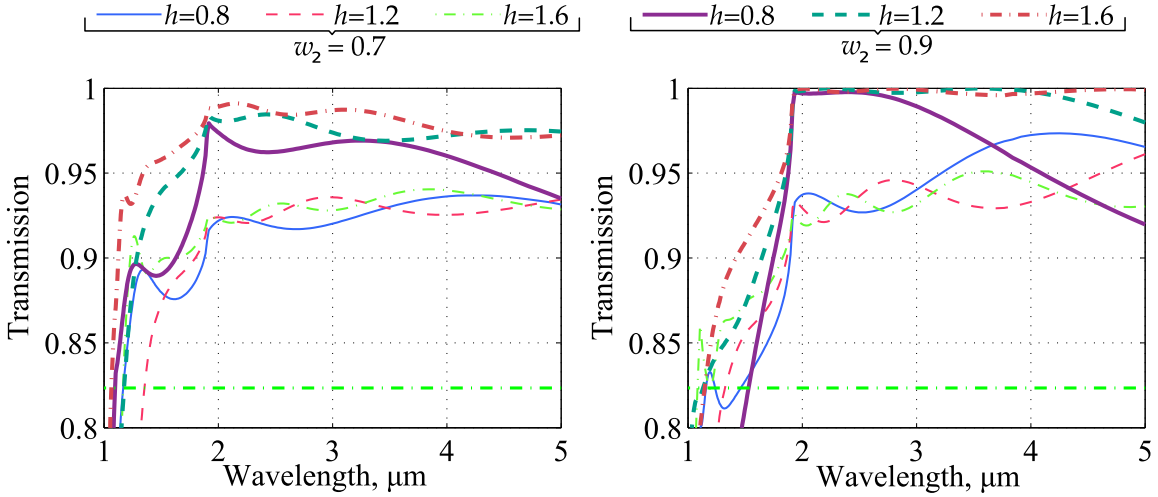

Figure 3.14: The theoretical transmission spectra for *output* coupling through a dimpled surface consisting of holes with (a) sinusoidal and (b) half-ellipsoid shapes.

3.5 Optimized cusp-like moth-eye structures

In this section, we computationally study two different moth-eye structure shapes, half-ellipsoids and pyramids, to design an ideal moth-eye structure for maximum transmission in the wavelength range 2–5 μm. We find that the ideal structure, whether positive or negative, has a cusp-like glass tip and a smoothly increasing cross-sectional width that be-

comes equal to the period of the features. We show two examples of this kind of structure in Fig. 3.16.

In the long wavelength limit, moth-eye structures provide a gradual change of the effective refractive index as light propagates across the air-glass interface, akin to an impedance transformer that matches the impedance of the optical surface to the impedance of the vacuum [51]. This long-wavelength limit picture is inexact, especially as the incident wavelength is on the order of the feature size, but it offers important insights that are useful for designing optimal structures.

The intuition provided by this picture suggests that the effective (average) refractive index of the layer at the highest point of the structure should be as close to that of the low index medium (air or vacuum in this case) as possible. Similarly, the bottom layer should have an effective index as close as possible to the index of the glass substrate. For layers in between, the effective refractive index should increase as gradually and as smoothly as possible. This intuition is consistent with our computational findings from Sec. 3.1–3.4.

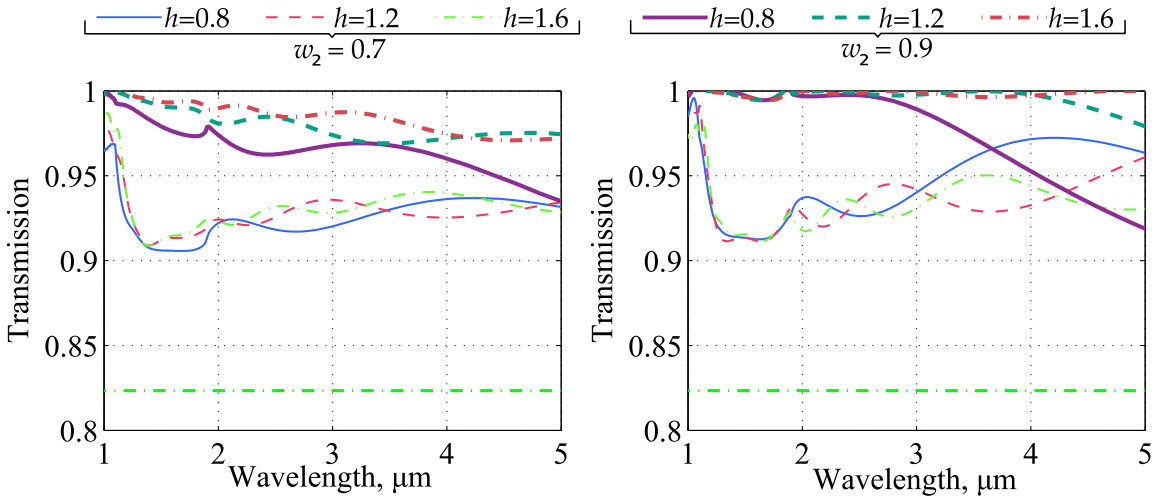

Figure 3.15: The theoretical transmission spectra for *input* coupling through a dimpled surface consisting of holes with (a) sinusoidal and (b) ellipsoid shapes.

3.5.1 Structure shapes One way to create cusp-like structures is to imprint a negative structure in the glass with a positive mold that has a packing ratio $w_2/s_x = 1$, i.e. the width at the base of the mold (w_2) matches its feature spacing (s_x). Such a structure using a half-ellipsoid shape is shown in Fig. 3.16(a). The half-ellipsoid structure is the upper half of an ellipsoid oriented along the z-axis whose height is given by the equation

$$z(x,y) = h\left[1 - \left(\frac{x}{w_2/2}\right)^2 - \left(\frac{y}{w_2/2}\right)^2\right]^{1/2}, \tag{3.3}$$

where the x and y dimensions are the axes parallel to the surface, z is the height perpendicular to the surface, h is the element height, and w_2 is the base width. Another way to create such a cusp is to imprint a positive structure that comes to a fine point at its tip. One such structure, defined by Southwell [52] but without a closed-form expression, is shown in Fig. 3.16(b). This structure is not rotationally symmetric, and hence its transmissivity is anisotropic, but the anisotropy is small, as shown in Sec. 3.4.1.

(**a**) Hexagonally-packed negative half-ellipsoid structures.

(**b**) Square-packed positive pyramid structures.

Figure 3.16: Cusp-like moth-eye structure feature shapes.

3.5.2 Results Figure 3.17 and Fig. 3.18 show the transmission spectra found by rigorous coupled wave analysis (RCWA) for different element heights or depths and different ratios of base width to element period (w_2/s_x). Figure 3.17 shows the results for negative

half-ellipsoids, and Fig. 3.18 shows the results for positive pyramids. Qualitatively, the highest transmissivity is obtained with the tallest/deepest elements and for the highest ratio of w_2/s_x, which makes the negative features more cusp-like.

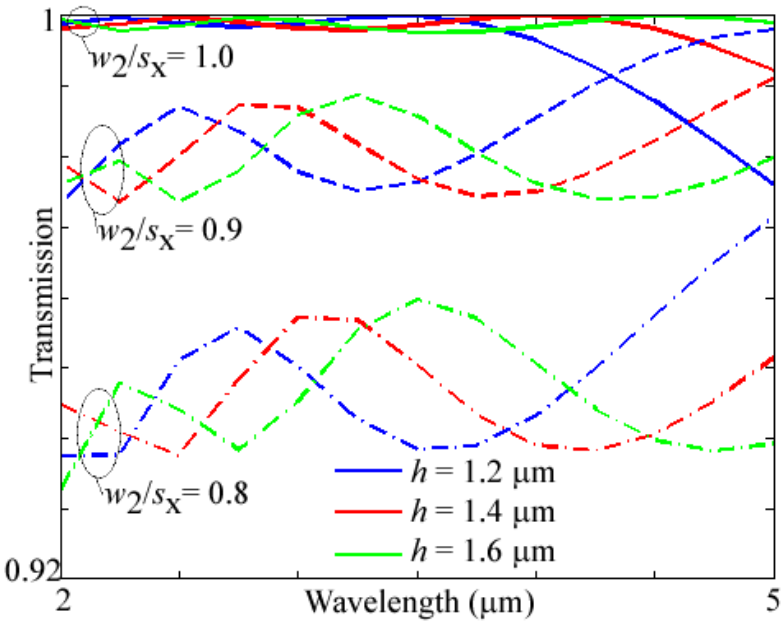

Figure 3.17: Negative half-ellipsoid transmission for depths of 1.2 μm, 1.4 μm, and 1.6 μm, and packing ratios of 0.8, 0.9, and 1.0.

We introduce a quantitative metric for evaluating these moth-eye structures: the mean (average) transmissivity for wavelengths between 2–5 μm. The average transmission for each structure is shown in Table 3.1. Using this metric, we find that positive pyramids of height 3.0 μm have an average transmissivity from 2–5 μm of 0.99878. Similarly, negative half-ellipsoids of height 1.6 μm have an average transmissivity from 2–5 μm of 0.99885. While both structures can achieve similarly high performance, positive pyramids require much taller structures for optimal transmission.

Our results demonstrate that while these ideal cusp-like half-ellipsoid structures would perhaps be difficult to achieve exactly in practice, they can provide excellent performance

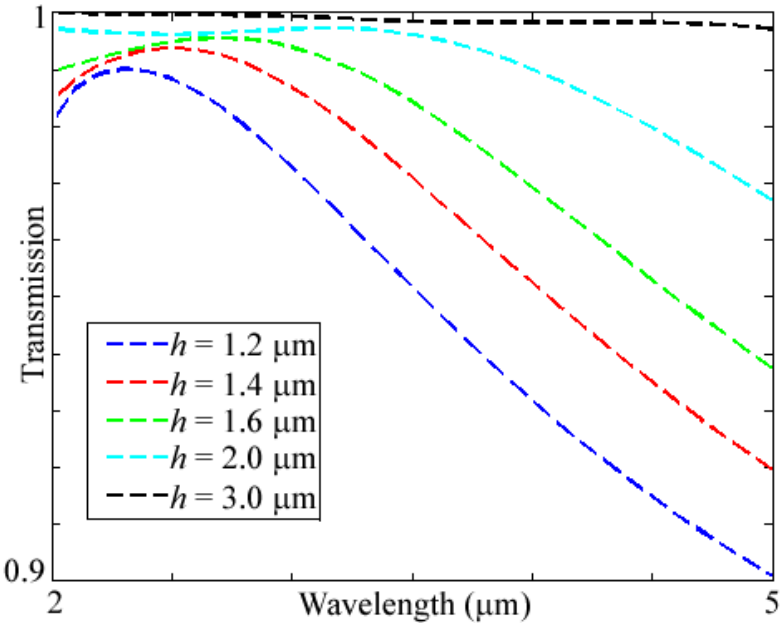

Figure 3.18: Positive pyramid transmission for depths of 1.2 μm, 1.4 μm, 1.6 μm, 2.0 μm, and 3.0 μm. The packing ratio is 1.0.

Packing	Height (μm)	Positive pyramid	Negative half-ellipsoid
$w_2/s_x = 1$	1.2	0.95033	0.99452
	1.4	0.96518	0.99813
	1.6	0.97635	0.99885
	2.0	0.99011	
	3.0	0.99878	

Table 3.1: Average transmission for each structure type from 2–5 μm.

with a reduced depth requirement compared to pyramid structures.

3.6 Increased laser-induced damage threshold

As previously mentioned, moth-eye structures have several advantages over traditional thin-film AR coatings, including environmental tolerance, surface adhesion, single material fabrication, minimal surface preparation, and self-cleaning via the lotus effect [8, 38].

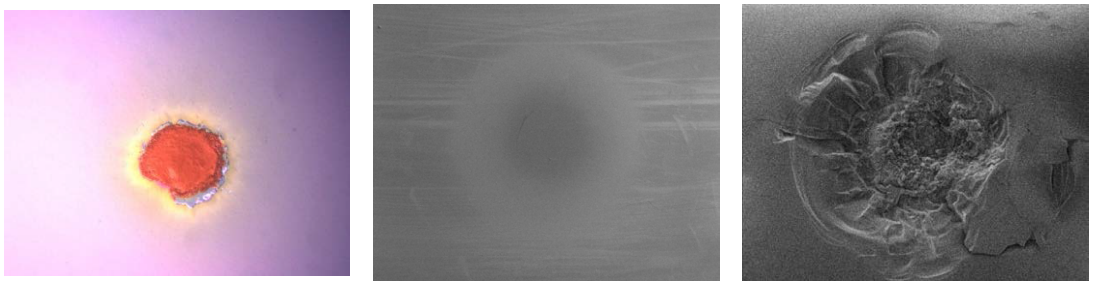

(**a**) Thin-film AR coating showing catastrophic damage at $20\,\mathrm{J}\cdot\mathrm{cm}^{-2}$.

(**b**) Moth-eye structure showing localized melting at $100\,\mathrm{J}\cdot\mathrm{cm}^{-2}$.

(**c**) Untreated optical interface showing catastrophic damage at $170\,\mathrm{J}\cdot\mathrm{cm}^{-2}$.

Figure 3.19: Comparison of damage mechanisms in AR coated optics (from [13]).

Additionally, in recent years it has been shown that in many cases periodic moth-eye structures have a higher laser-induced damage threshold (LIDT) than do traditional AR-coated surfaces [46–48]. In fact, the highest LIDT in fused quartz to date was recently demonstrated using moth-eye structures [13]. While both traditional AR coatings and moth-eye-structured surfaces usually have LIDTs lower than bulk material, damage in traditional AR coatings can occur at low laser fluences due to surface imperfections, thermal coefficient mismatch, and poor layer adhesion. In moth-eye-structured surfaces, however, higher laser fluences cause localized melting of the surface structures before catastrophic damage occurs, often allowing the optics to continue performing albeit with reduced transmission, which can be very important in some applications. Fig. 3.19 shows SEM images compareing damage mechanisms and LIDTs for thin-film AR, moth-eye, and untreated optics.

The increased LIDT in moth-eye structures may seem counterintuitive, since it might be expected that the microstructured surface causes field enhancement. This field enhancement should reduce the amount of energy per unit area required to cause catastrophic damage. In this section, we show results for three particular moth-eye structures and calculate the time-averaged Poynting flux density in and around the microstructured surface to inves-

tigate why moth-eye structures are resistant to laser damage. Similar results with two other structure shapes indicate that these results hold generally for any appropriately designed moth-eye structure, regardless of feature shape or dimensions. We also give a physical explanation for this behavior. We show that this behavior can be understood physically as a consequence of the oblique incidence of the waves on the walls of the moth-eye structure and the standard boundary conditions for electromagnetic waves at an interface.

Much theoretical work has investigated damage mechanisms in traditional thin-film coatings, particularly "nodule" defects, cf. [53, 54]. The exact mechanisms for damage in particular thin-film coatings may be unknown, and possibilities, including avalanche ionization, dielectric breakdown, or thermal effects, can vary depending on the pulse duration, pulse repetition rate, spot size, and peak power of the laser input [55].

Jing et al. [56] studied localized enhancement in two-dimensional (2D) moth-eye structures with a triangular cross-section in the visible spectral region. They showed that the field enhancement is highly dependent on the aspect ratio of the microstructure for the TE polarization, but does not vary significantly for the TM polarization. It can be shown, for a circularly symmetric three-dimensional (3D) microstructure in a square or hexagonal packing scheme, such as the structures we study here, that there should be no dependence on polarization as long as the incident light is normal to the surface [51, 57]. Therefore, in our work, it is sufficient to study a single polarization.

3.6.1 Computer model In our computer model, we study moth-eye surfaces that are either "positive," i.e., raised from the surface, or "negative," i.e., depressed into the surface. We calculate the time-averaged Poynting flux for both positive and negative structure surfaces using RCWA with diffraction orders up to ± 9 included in the calculation. We have verified that increasing the number of harmonics does not influence the results.

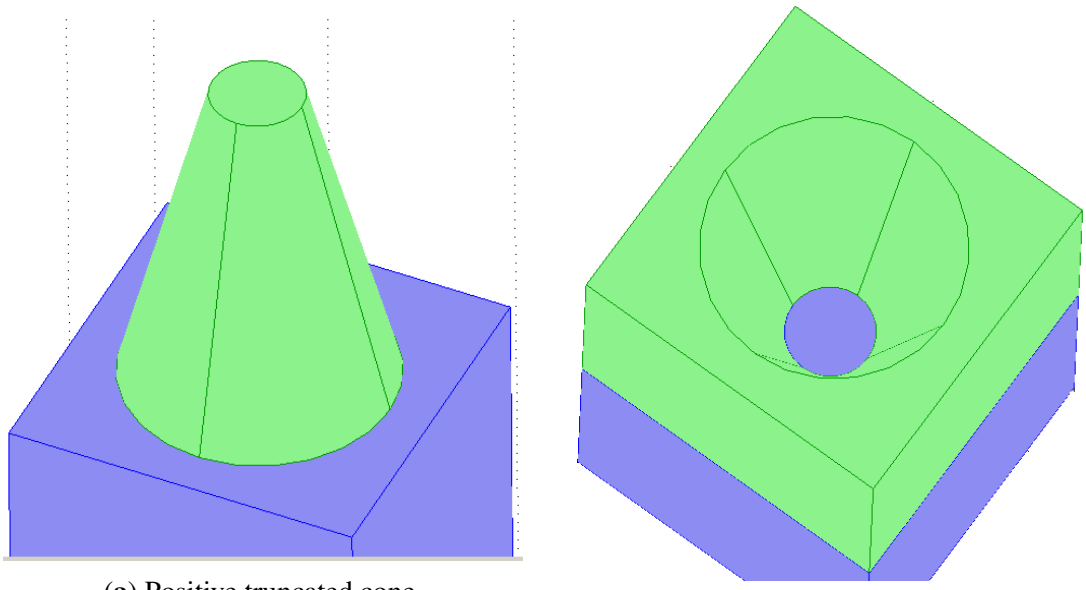

(**a**) Positive truncated cone.

(**b**) Negative truncated cone.

Figure 3.20: Comparison of positive and negative moth-eye structures used in the computer simulation. Green areas indicate the As_2S_3 microstructure, while blue areas indicate the As_2S_3 substrate.

The Poynting flux is given by $\mathbf{S} = \mathbf{E} \times \mathbf{H}$. Its time average over one period is given by $\langle \mathbf{S} \rangle = (1/T) \int_0^T \mathbf{S}(t) \mathrm{d}t$. The time-averaged Poynting flux, also called irradiance, measured in $\mathrm{W\,m^{-2}}$, represents rate of energy transfer per unit area. Areas that experience a higher energy flux density (a higher Poynting flux) should experience damage first.

We first consider a moth-eye structure with the shape of a truncated cone, which has a base width of 400 nm, a height of 800 nm, and a tip width of 200 nm. The features are square-packed with a period of 920 nm. Figure 3.20 shows the shape of the moth-eye structure models used for this study. The computational region includes the incident medium, air, on top of the As_2S_3 microstructure, which sits on an infinitely thick substrate of As_2S_3. The features shown here represent a single unit cell in an infinite two-dimensional array. The positive shape is similar to the structure used to validate our model in Sec. 3.1.

The positive and negative shapes are mirror images; the negative shape is the feature that would be created if the positive shape were stamped into the As_2S_3 glass and vice-versa.

Figure 3.21 shows the total transmission spectrum, including all diffracted orders, of the positive truncated cone features for light incident on the microstructured surface from the air above it. The transmission increases rapidly as the wavelength decreases below 1.8 μm because higher diffracted orders increase in number and intensity as the wavelength decreases. While it is true that diffraction orders greater than zero are predicted to exist for wavelengths below 2.25 μm, we have verified that higher diffracted orders do not carry energy at $\lambda = 2$ μm, the wavelength used for these studies, as described in more detail in Sec. 3.6.5. While other structures have better anti-reflective performance [9, 52], this structure remains partially anti-reflective above 2 μm since the transmission of a plane surface is 0.83.

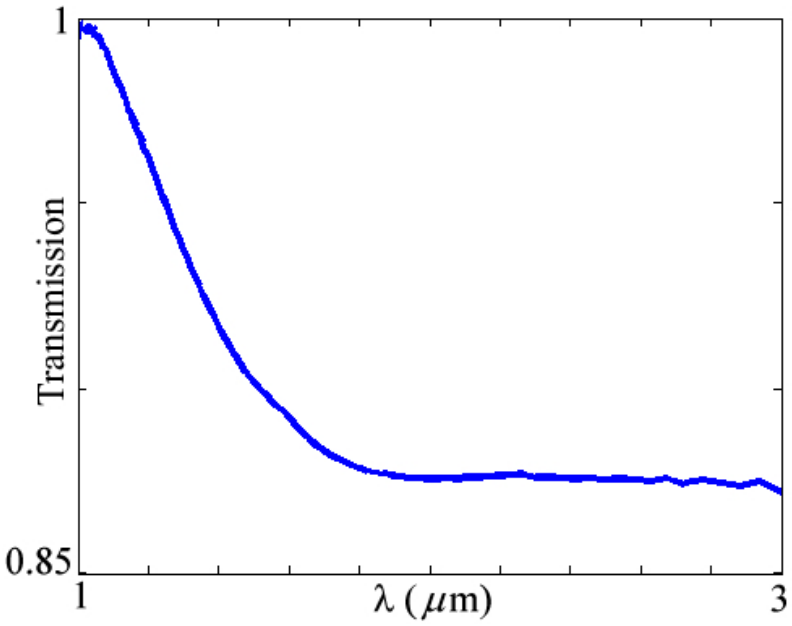

Figure 3.21: Transmission spectrum of the truncated cone moth-eye structure.

The input field is a CW plane wave with a wavelength of $\lambda = 2$ μm, normally incident on the structure in a p-polarization, so that the electric field is oriented in the x-direction. We take the refractive index of As_2S_3 to be $n = 2.45$ at 2 μm. We do not consider absorption in this work, i.e. $\mathrm{Im}(n) = 0$. As_2S_3 has a linear loss at 2 μm of about 0.5 dB/m, which means that a wave traveling through the tallest part of the microstructure considered here would lose a fraction 10^{-7} of its power to absorption over the region considered in this work. Thus, an input with a power of 1 kW would cause absorption of less than 0.1 mW over the region of these calculations.

3.6.2 Results Figure 3.22 shows the time-averaged Poynting flux $\langle \mathbf{S} \rangle$ (irradiance) in the microstructure as a function of position for the two structures. The figures show a slice through the unit cell, with the black lines delineating the microstructure. In all plots, the incoming field propagates downward from the top of the figure — for the negative structures, near the base of the cone, and for positive structures, near the tip of the cone. Figures 3.22(a) and 3.22(b) show the case of the positive cone feature, while Figs. 3.22(c) and 3.22(d) show the case of the negative cone feature. Figures 3.22(a) and 3.22(c) are in the plane of the incoming electric field, while Fig. 3.22(b) and 3.22(d) are oriented along a plane that is orthogonal to the plane of the incoming electric field.

For a positive cone, Figs. 3.22(a) and 3.22(b) show a large enhancement of the irradiance around the outer sides of the cone, with greatly decreased irradiance around the inner sides. For a negative cone, Figs. 3.22(c) and 3.22(d) show the greatest enhancement around the inner sides of the cone, with cool spots outside the depression and inside the As_2S_3 glass. The narrow end of the cone, the deepest part of the negative feature, shows the highest concentration of field energy, whereas, for a positive structure, the opposite is the case. Since the materials in the positive and negative case are inverted, we find in both

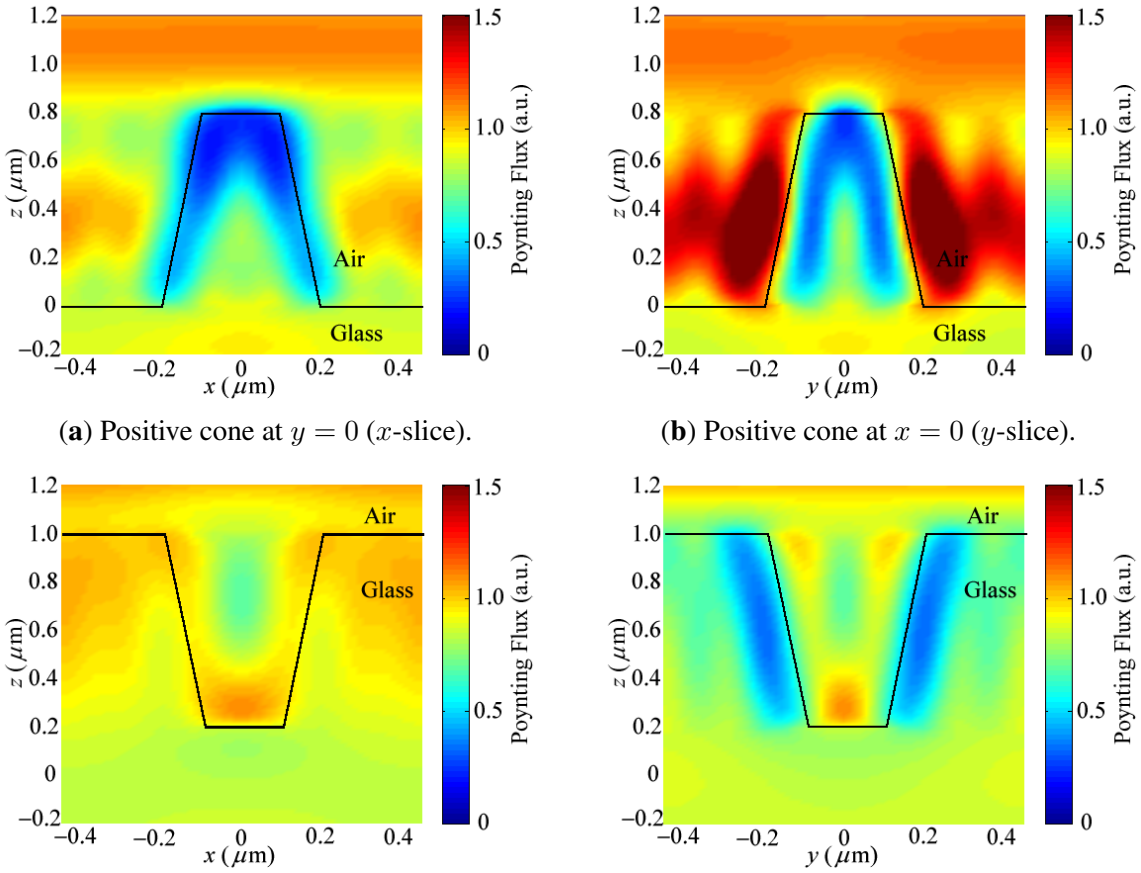

(**a**) Positive cone at $y = 0$ (x-slice).

(**b**) Positive cone at $x = 0$ (y-slice).

(**c**) Negative cone at $y = 0$ (x-slice).

(**d**) Negative cone at $x = 0$ (y-slice).

Figure 3.22: Average Poynting flux density in truncated cone structures with p-polarized incident light (electric field oriented along the x-direction)

cases that the air sides of the lateral cone surface have the greatest Poynting flux, while the glass sides of the lateral cone surface have the lowest Poynting flux. Additionally, there is a small area of slightly increased Poynting flux near the center of the glass part of the microstructure, corresponding to the center of the base of the cone in the positive structure.

We find that the positive truncated cone structure shows greater localization of the enhancement compared to the negative structure. The slices out of the plane of the incoming electric field also show greater localization of enhancement.

To demonstrate how the flux density changes from one orthogonal plane to another, we show a top-down view of the irradiance corresponding to a horizontal slice through the middle of the cone structure at $z = 0.4$ μm in Fig. 3.23. This view should be compared to Fig. 3.22(a) and (b), which show the same result in the other two orthogonal planes.

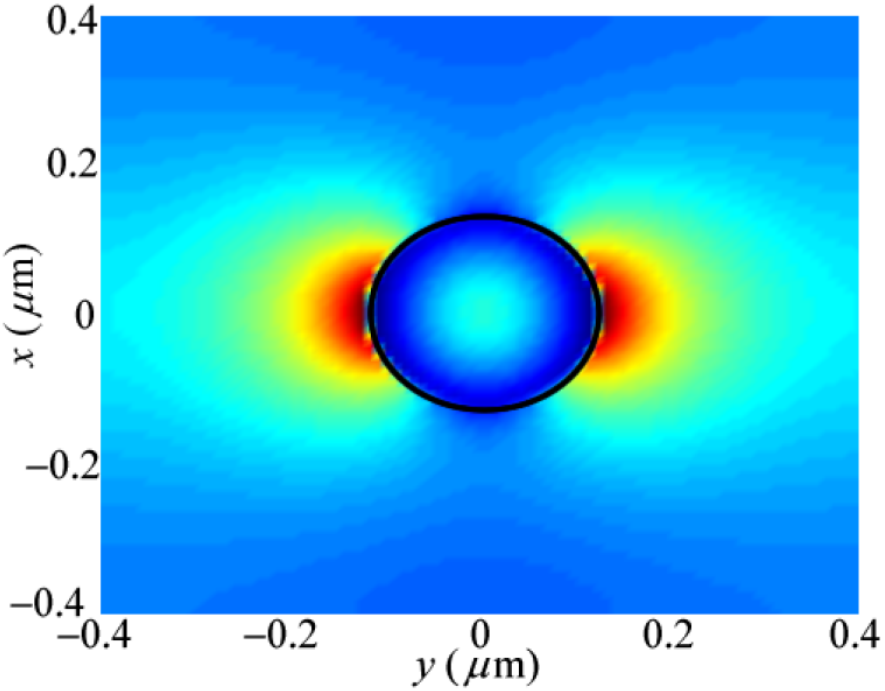

Figure 3.23: Top-down view of the average Poynting flux density for a positive cone at $z = 0.4$ μm (x-y slice).

3.6.3 Physical explanation We may physically understand the decreased irradiance inside the glass by first noting that the propagation is highly oblique with respect to the sides of the microstructures, i.e., the angle of incidence with respect to the normals is nearly 90°. We next recall that the normal displacement field $\mathbf{D}$ will be continuous across an interface, so that the electric field $\mathbf{E} = \mathbf{D}/\epsilon$ is reduced in the higher index material. Since the irradiance or Poynting flux $\mathbf{S}$ is proportional to the electric field according to $\mathbf{S} = \mathbf{E} \times \mathbf{H}$,

it will be reduced in the lower index material in the plane of the electric field, regardless of whether the microstructures are positive or negative. Conversely, the irradiance will be enhanced out of the plane of the electric field since the total irradiance is fixed. This principle is used to guide radiation in the low-index region of slot waveguides [58]. These results are consistent with experimental results, which show catastrophic damage at higher laser fluences; the glass part of the microstructure is subjected to less irradiance as a result of the field enhancement.

3.6.4 Additional results To verify the intuition that similar results will hold for other moth-eye structures with different feature shapes and dimensions, we calculated the time-averaged Poynting flux $\langle \mathbf{S} \rangle$ in a positive half-ellipsoidal element with the same base width, height, and feature spacing, using the same input source and model setup. The results, shown in Fig. 3.24, are similar to those for the truncated cone: The areas of highest irradiance are on the air side of the air-glass interface on the lateral sides of the microstructure. We have seen similar results with pyramids and sinusoidally-shaped elements. Hence it is reasonable to conclude that any properly designed moth-eye structure will exhibit similar behavior.

For an ideal thin-film AR coating, there will be no reflection at the design wavelength, and all of the flux density will be equal through the air above the coating, each layer of the coating, and the substrate below. In an ideal case, there will be no enhancement of the irradiance, which also means no decrease in irradiance in the coating, as is seen in moth-eye structures. This ideal behavior is shown in Fig. 3.25 for a two-layer thin-film coating. However, in the case of a defect in the coating, there will be enhancement around that defect [54]. Also, if the layers of the coating expand at different rates, gaps may occur between the layers or the substrate, and these gaps may experience irradiance enhancement.

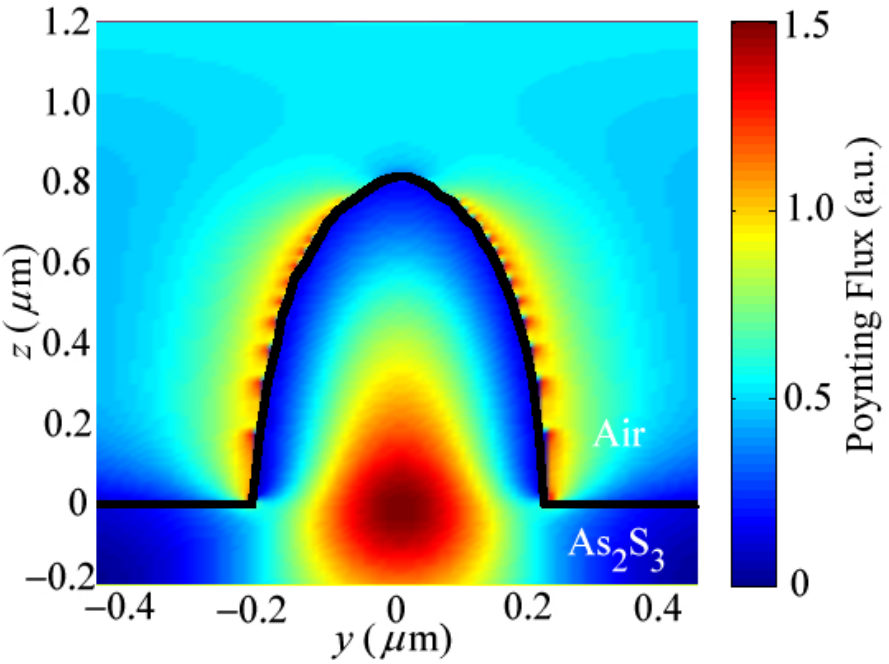

Figure 3.24: Average Poynting flux density in a half-ellipsoidal structure at $x = 0$ (y-slice).

3.6.5 Is this enhancement a diffraction effect? According to the theory of diffraction gratings [59], the one-dimensional scalar diffraction equation, given by

$$\lambda = \frac{n_i d}{m}, \tag{3.4}$$

predicts that, for an element spacing of $d = 0.92$ μm and refractive index of $n_i = 2.45$, in addition to the $m = 0$ order, diffracted orders of $m = \pm 1$ will in principle be transmitted in this structure for wavelengths below $\lambda = 2.25$ μm, which includes the $\lambda = 2.0$ μm wavelenth used in this study. However, this fact does not imply that those higher diffracted orders will carry any energy. In fact, we will show here that only the zeroth (on-axis) diffracted order has energy.

First, Fig. 3.21 shows the transmission spectrum of a wave traveling into the positive

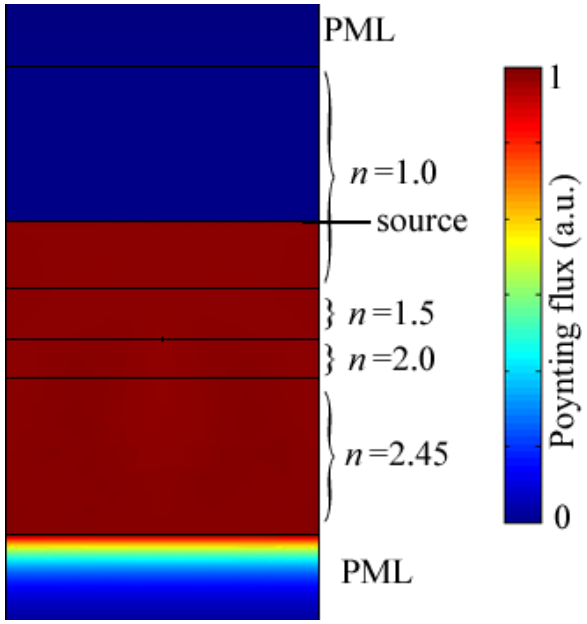

Figure 3.25: Average Poynting flux density in a two-layer thin-film coating. The top layer has a refractive index $n = 1.5$ and the second layer has $n = 2.0$. Both of these layers have a quarter wavelength thickness, which is refractive index dependent. The top and bottom layers in the structure are perfectly-matched layers (PMLs) to eliminate reflections from the edges of the simulation.

truncated cone features that we study in this Sec. 3.6.1. The transmission is approximately constant for wavelengths between 1.8–3 μm and increases as the wavelengths decreases below 1.8 μm. The reason for this increase is that higher diffracted orders, which are readily coupled into the higher index material, increase in number and intensity for shorter wavelengths. The transmission spectrum for the case of output coupling, where the wave is traveling from the higher index material to the air, shows the opposite effect; higher diffracted orders that exist for shorter wavelengths cannot couple out of the microstructure, and the transmission decreases in this case for wavelengths less than 1.8 μm. This result shows that even though higher diffracted orders are predicted to exist for wavelengths below about 2.2 μm, they have no effect on the transmission (because they carry no energy) until the wavelength decreases below 1.8 μm.

Second, the electric field below the microstructure maintains the plane-wave nature of the input. Figure 3.26 shows a plot of the electric field propagating in the high index material below the microstructure. There is no change in the electric field below the microstructure along the y-direction. A horizontally alternating electric field in the y-direction would indicate the influence of a grating momentum, and hence higher diffracted orders, but this behavior is not evident in Fig. 3.26.

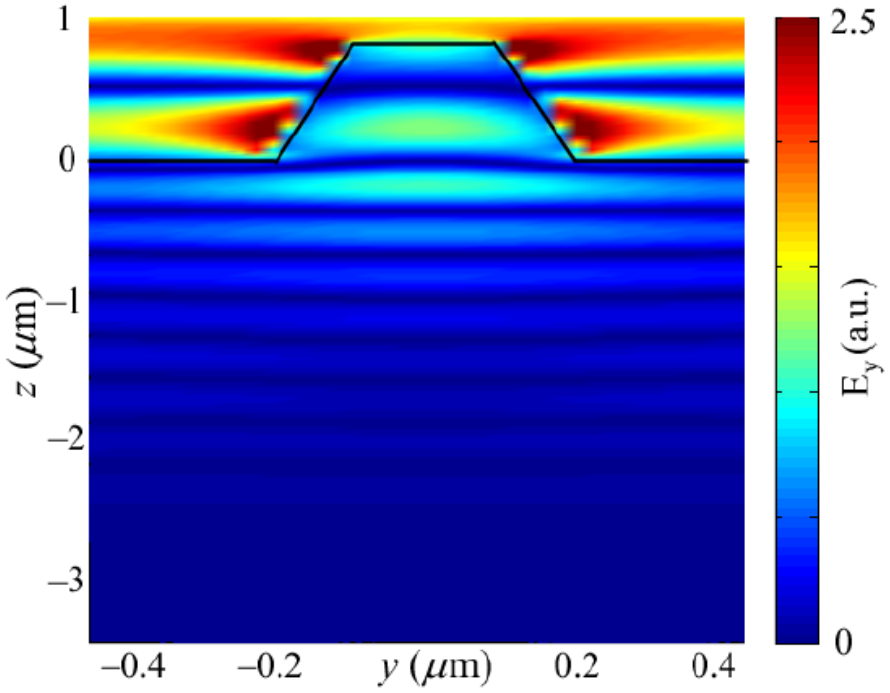

Figure 3.26: Electric field distribution at $x = 0$ (y-slice).

Finally, if higher diffracted orders were present in the transmitted spectrum and were causing the irradiance enhancement by an interference effect, we would expect different results for wavelengths longer than the longest wavelength where nonzero diffracted orders are predicted to be present, for example, $\lambda = 2.5$ μm. Fig. 3.27 shows the irradiance for a positive cone in out of the plane of the electric field for a wavelength of 2.5 μm. This plot

can be compared to Fig. 3.22(b), which is the same except that the wavelength is $\lambda = 2.0$ μm in Fig. 3.22(b). Fig. 3.27 shows qualitatively the same irradiance enhancement as the shorter wavelength, with approximately the same position and intensity of the enhancement. Therefore, the irradiance enhancement effect is not due to higher-order diffraction.

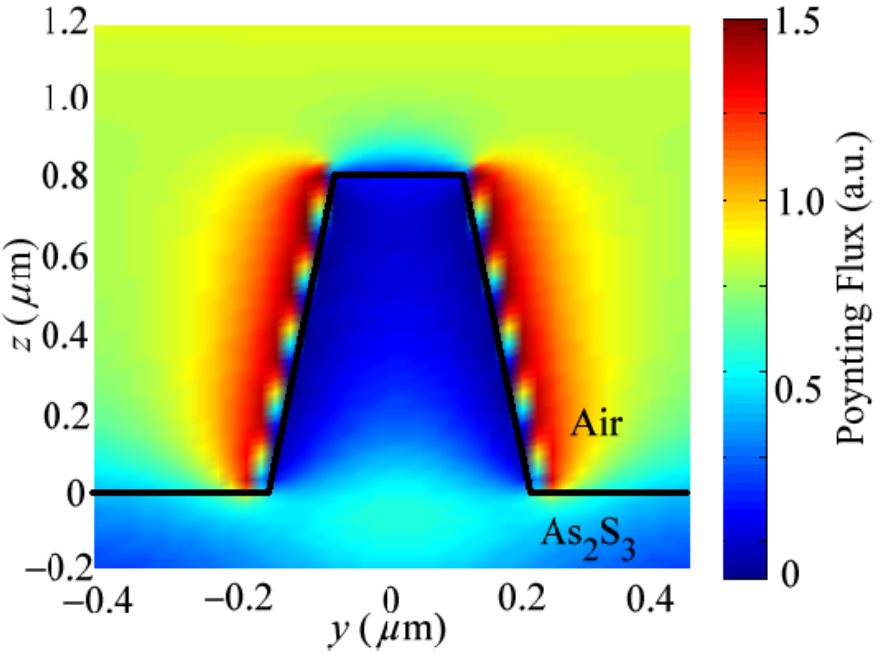

Figure 3.27: Time-averaged Poynting flux density for a positive cone at x = 0 for a wavelength of 2.5 μm.

All these results lead to the conclusion that, although the ± 1 transmitted diffraction orders exist for a wavelength of 2 μm, they carry no energy and therefore have no effect on the results or the calculation.

3.6.6 Further considerations This work may have practical applications beyond explaining the increase in laser damage threshold. For example, surface-enhanced Raman scattering (SERS) is due to the field enhancement facilitated by the microstructuring of the

surface. Using this method, SERS structures could be designed to increase the enhancement and optimize its location.

In the future, a careful study should be conducted to determine if these enhancement results hold for different feature shapes, dimensions, pitches/spacings, materials, and input wavelengths and angles. In this dissertation, we explained these enhancement results in terms of the boundary conditions for Maxwell's equations, and an important part of our interpretation of the results is that the sidewalls of the structure were nearly orthogonal to the direction of the incident electric field. This condition would not hold for angles of incidence much larger than normal or for structures with curved sides, such as hemispheres, or structures with a very wide base and narrow tip, such as a short perfect cone. However, the resistance to laser damage has been demonstrated in random AR surface structures, where, presumably, our explanation for this resistance no longer applies.

A careful study would include features of various shapes and dimensions from tall to short, narrow to wide, rounded and straight sided, with close and far packing, and different wavelengths and angles of incidence to simulate the entire range of possible AR surface structures. If indeed the results are similar for very different shapes and wavelengths, the physical interpretation may need to be revised. However, if the results are not similar for different structures and there is an optimal shape or size, this information would be important to the scientific community.

A quantitative analysis of the energy flux density for different feature shapes and sizes would also be useful. Particular questions include:

1. How does the intensity of the enhancement change as the features change?

2. How does the location of the enhancement change as the features change?

3. How does the location/intensity of the enhancement change as the angle of incidence changes?

4. How does the location/intensity of the enhancement change as the wavelength changes?

Answers to these questions could be useful for applications such as surface-enhanced Raman scattering, where the location and intensity of the enhancement can be optimized for better operation.

3.7 Optimal structures for short and long wavelengths

A trade-off exists in moth-eye structures between the location of the diffraction edge, which, for a particular material, depends only on the feature spacing or pitch, and the optimal properties of a wide base and gradually increasing refractive index profile. Transmission rapidly decreases for output coupling and rapidly increases for input coupling for wavelengths below the diffraction edge. Additionally, it is advantageous for the moth-eye structure feature to have as wide a base as possible, especially for positive features. However, when the feature spacing increases, for example to accommodate a wider-based structure, the diffraction edge moves to longer wavelengths, which effectively decreases the transmission for short wavelengths.

An ideal AR surface structure would have very high transmission and no diffraction edge. It would be useful to investigate is whether the diffraction edge can be pushed to shorter wavelengths or even eliminated by changing the structure. We now describe several approaches for achieving such a structure.

Very tall structures with a very small period have been shown to perform well over the range from near-IR wavelengths to mid-IR wavelengths. Huang et al. [60] showed

random silicon nanotips could increase transmission from air to silicon to over 99% from the visible to near-IR. The nanotips were characterized by a base width of 200 nm and a height of 1–16 μm. It should be investigated if similar nanotip arrays on fused silica or As_2S_3 can provide similar transmission properties over the wavelength range of interest. This possibility could be efficiently investigated using an approximate method, particularly effective medium theory (EMT).

It is also possible that a moth-eye structure that achieves good performance from 2–5 μm can have the effect of the diffraction edge mitigated in some way, possibly by adding a small-scale random variation on top of the underlying moth-eye structure. It has been observed experimentally that adding small-scale height fluctuations to a moth-eye anti-reflective surface adds oscillations to the transmission below the diffraction edge, eliminating its monotonic decrease for short wavelengths. This behavior indicates it may be possible to reduce the effect of the diffraction edge through an appropriate small-scale structuring of the moth-eye surface. Given the possibly random nature of the small-scale structuring necessary for this effect, this study might lend itself well to optimization by a genetic algorithm. The important parameters to investigate are the optimal underlying large-scale moth-eye structure and the location and height/depth of the small-scale variation on top of it.

Chapter 4

Chalcogenide antiresonant fibers

The concept of antiresonance has long been understood as a method of confining light in a low refractive index material [61]. However, with recent advances in PCFs and microstructured optical fibers, there is renewed interest in using this guidance mechanism to realize low-loss, broadband, hollow-core optical fibers. Several such antiresonant fibers (ARFs) have been studied since the perfection of production methods for PCFs in the late 1990s, including those described in [62, 63].

Recent hollow-core antiresonant fibers are mostly "tube-lattice" fibers, meaning that the fiber is constructed of a hollow core surrounded by a circular array of hollow tubes. These fibers are sometimes called "negative-curvature" fibers, or negative-curvature hollow-core fibers, meaning that the surface normal vectors at the wall of the microstructured cladding are anti-parallel to a radial unit vector. The negative wall curvature changes the boundary conditions between core modes and cladding modes so that coupling between them is far weaker than is the case with positive curvature. As a consequence of this "inhibited coupling" effect, the core mode is guided, rather than leaking out [64].

The recent resurgence in interest in antiresonant fibers dates to 2010 when Wang et al. [14] discovered that silica Kagome fibers with a hypocycloid core shape had much lower

loss than structures with a normal circular core shape. An example of the hypocycloid Kagome fiber geometry is shown in Fig. 4.1. This fiber geometry leads to a relatively low loss of around 150 dB/km, which was comparable to state-of-the-art photonic-bandgap hollow-core PCFs at the time, yet over a much wider bandwidth, from ∼1–1.7 μm — a measurement that was limited by the bandwidth of the OSA used in the experiment. In this work, the authors found a trade-off between bandwidth and loss. That is, by reducing the thickness of the walls of the web of supporting structures in the cladding, the bandwidth could be increased at the expense of increased loss.

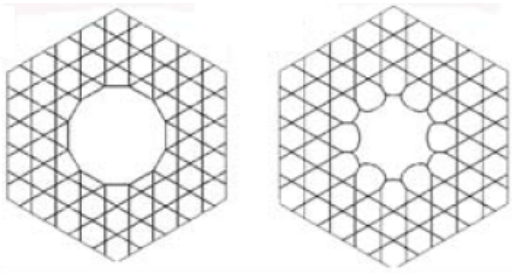

Figure 4.1: Hypocycloid Kagome fiber geometry from Fig. 1 of [14].

The next advance came when Pryamikov et al. [15] at the Russian Academy of Sciences showed that the Kagome lattice was unnecessary for wave guidance if the core shape had a negative curvature. This work used a circular outer jacket supporting a cladding of eight adjacent circular silica capillaries, leaving a hypocycloid air-core wall with a negative curvature, as shown in Fig. 4.2. In this work, transmission bands of relatively low loss were found from approximately 0.8–4 μm in wavelength, but the loss was higher than in [14], on the order of several dB/m. Although the loss was higher, the pioneering advance of this work was to demonstrate that a relatively simple geometry could support guided modes over a broad wavelength range. The authors also argued that the physical reason for guid-

ance was the negative curvature of the core wall, which weakens the coupling between the core and cladding modes. Further, this work coined the term “negative curvature fiber.”

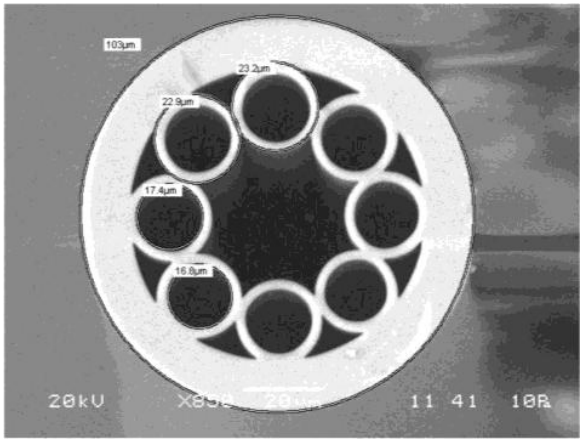

Figure 4.2: NCHCF geometry from Fig. 4 of [15].

Later, Yu et al. [16] demonstrated a low-loss structure using silica for 3–4 μm using a noncircular cladding structure, as shown in Fig. 4.3. This work showed two geometries: one optimized for low loss and one optimized for mid-IR transmission. The low-loss optimized geometry resulted in a loss of 34 dB/km at 3 μm. The fiber optimized for mid-IR transmission had a loss of 0.5 dB/m at 4 μm. This work also explored the effect of fiber bends on the loss and showed that loss was low for bend radii greater than 40 cm. Additionally, the authors explained the spectral dependence of the transmission in terms of resonances between core modes and cladding modes created by the core wall and gave a mathematical expression for the dependence of these resonant wavelengths as a function of the core wall thickness.

More recently, Kolyadin et al. [65] showed that eliminating intersections of the cladding structure elements further reduces the loss in negative-curvature ARFs. The geometry in this paper is similar to the geometry in [15], except that the silica capillaries are smaller in diameter relative to the diameter of the outer jacket so that the capillaries do

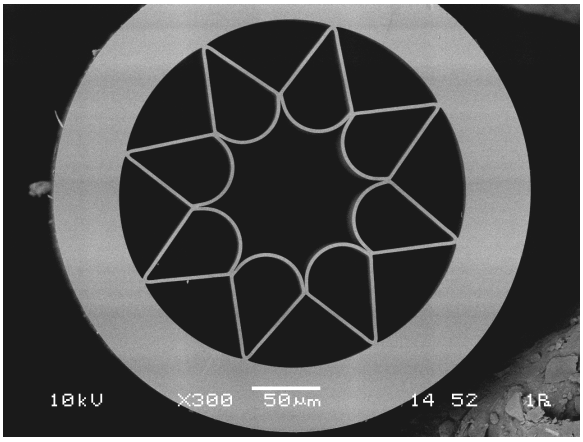

Figure 4.3: NCHCF geometry from Fig. 1 of [16].

not touch each other, as shown in Fig. 4.4. Hence, the capillaries create a negative curvature core wall, while reducing the thickness of the cladding structure. This reduction of the cladding structure thickness reduces the optical density of states in the cladding, weakening the coupling between core and cladding modes, which reduces loss. In comparing similar geometries with touching and non-touching capillaries, the authors showed that both exhibit a similar band-structure in the transmission spectrum, but within those bands, the non-touching capillaries had an order of magnitude lower loss.

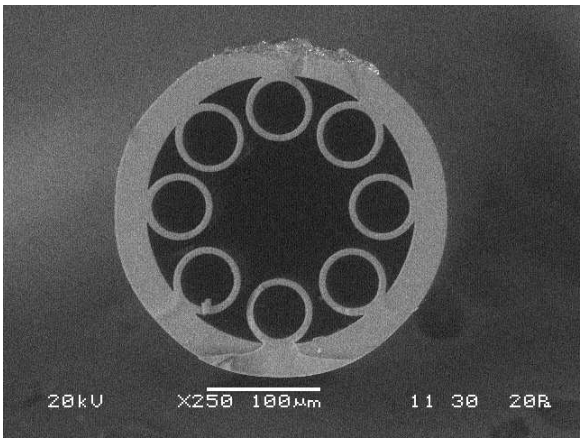

Figure 4.4: NCHCF geometry from Fig. 3 of [65].

Also recently, Belardi and Knight [66] computationally investigated the effect of changing the curvature of the core wall in silica teardrop cladding fibers similar to the one shown in Fig. 4.3. They showed again that the negative curvature of the core wall is essential for guidance and showed that as the negative curvature of the core-wall increases, the guidance improves. They also showed that loss peaks in the transmission spectrum are due to resonances between degenerate modes in the air core, in the silica cladding, and in the air cores of the cladding tubes. While previous work [65] had suggested this physical origin for the loss peaks, it had not been demonstrated experimentally.

Belardi and Knight [67] have also recently investigated the bending loss of these silica ARFs using a geometry of circular capillaries (see Fig. 4.5) similar to the geometry described in [65]. They showed that they could design and build a fiber with an optimized geometry to realize a low bending loss of 0.25 dB per turn at a wavelength of 3.35 μm and a bend radius of 2.5 cm. The fiber also had less than 200 dB/km loss from 2.8 μm to 3.5 μm.

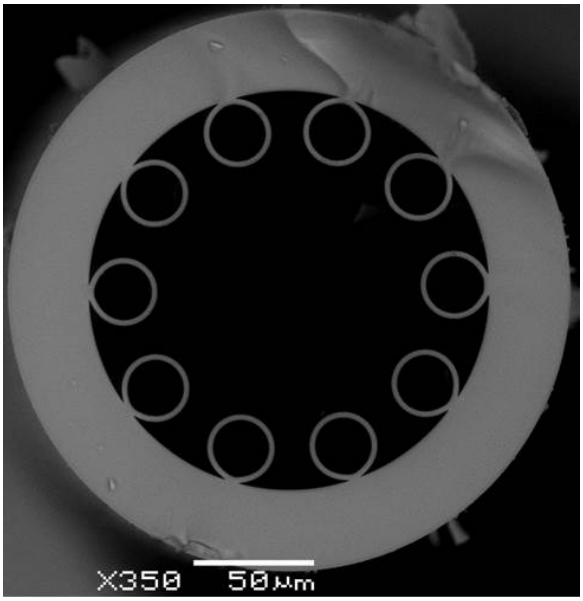

Figure 4.5: NCHCF geometry from Fig. 4 of [67].

More recently, Poletti [68] demonstrated that the loss of NCHCFs could be further reduced by orders of magnitude by introducing more, smaller cladding tubes nested in the larger ones, as shown in Fig. 4.6. These new tubes increase the geometric dissimilarity of the core mode and the cladding air modes, which reduces their coupling. Poletti also showed that further nesting cladding tubes inside of the nested cladding tubes, making a so-called "doubly-nested" ARF can decrease the loss even more.

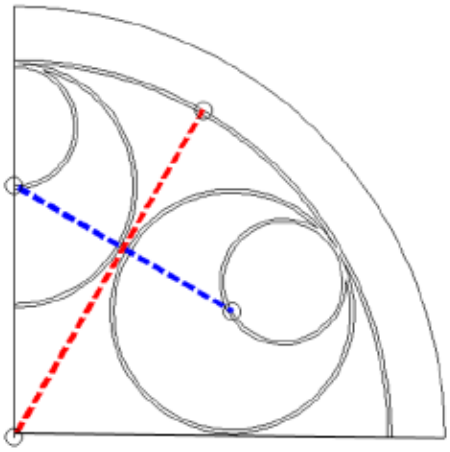

Figure 4.6: Singly nested antiresonant fiber geometry (quarter section) from Fig. 10 of [68].

Later, Habib et al [69] showed that the loss of of singly-nested fibers can be further reduced to levels below the doubly-nested fiber by adding two more nested cladding tubes, not inside the nested tubes, but adjacent to them. An example of these so-called "adjacent-nested" ARFs are shown in Fig. 4.7.

Since negative curvature ARFs are a relatively recent advance, significant advances using chalcogenide materials for fabrications have yet to be realized. Only one experimental study to date [17] used a chalcogenide ARF, and it was only designed for use at around 10.6 μm, although there have been theoretical studies at shorter wavelengths [70]. The ge-

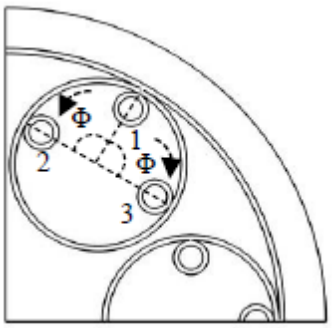

Figure 4.7: Adjacent nested antiresonant fiber geometry (quarter section) from Fig. 4 of [69].

ometry of the fiber used in [17] is shown in Fig. 4.8. The eccentricity of the capillaries in Fig. 4.8 compared with, for example, Fig. 4.2 demonstrate the difficulty in working with chalcogenide materials, in this case $Te_{20}As_{30}Se_{50}$. The authors of this work computationally designed an optimized geometry to theoretically obtain loss that is less than 1 dB/m near the CO_2 laser radiation wavelength of 10.6 μm. The experimentally-realized fiber has a loss of about 11 dB/m at this wavelength and a loss of less than 17 dB/m over the wavelength range of 8–11 μm.

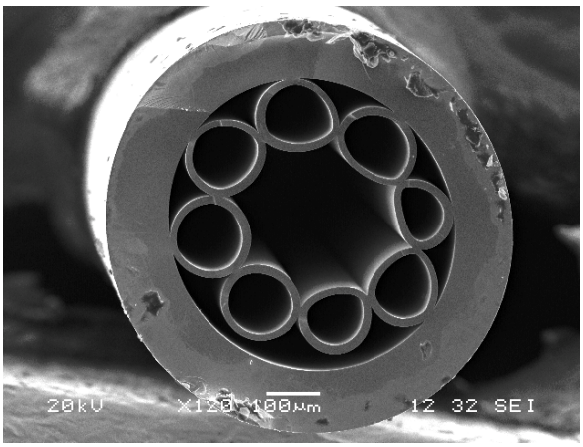

Figure 4.8: NCHCF geometry from Fig. 3 of [17].

An optimal structure in chalcogenide glass has yet to be found for the wavelength range of 1–10 μm. In the proceeding chapter, using lessons learned from fabrication of ARFs in silica, we optimize the fiber structure to find a low loss As_2S_3 ARF in the mid-IR spectral range by simulating different geometries in COMSOL. We will also investigate the tolerance of these designs to perturbations in the parameters.

4.1 Simulation methodology

To simulate these fibers, we use COMSOL Multiphysics, a finite-element mode solver. COMSOL approximates the two-dimensional wave equation by discretizing the entire geometry with finite elements and solving the resulting eigenvalue equation for the propagation constant of a limited number of modes. We simulate one quarter of the circular geometry and use periodic boundary conditions to reduce the computation requirements of the model, which can be extremely high, due to the fine spatial discretization necessary to obtain accurate results.

A typical geometry is composed of an outer jacket, or cladding support, which is a cylindrical shell made of As_2S_3, that keeps a number (usually 6–8) of cladding tubes, which are smaller cylindrical shells also made of As_2S_3, in place. Further, there may be more cladding tubes of smaller radius inside the larger cladding tubes. Between the largest cladding tubes is a hollow air-core which supports guided modes because of the antiresonant geometry. We take the refractive index of the air-cores to be the same as the lossless vacuum, $n = 1$.

The jacket layer of the fiber is set as a "perfectly-matched layer," a lossy element that simultaneously 1) reduces the size of the model by eliminating the need for an infinite transverse extent and 2) simulates the fiber's confinement loss. The refractive index and loss of the material, As_2S_3, is set as a function of wavelength according to data measured

at NRL. The loss of a particular mode is computed by transforming the imaginary part, k_i of its effective refractive index, $n_{\text{eff}} = n + ik_i$, according to the equation

$$\text{Loss (dB/m)} = \frac{40\pi k_i}{\lambda_0 \ln 10}. \tag{4.1}$$

The set of modes in these fibers is dense because of the large number of air-cores and the large radii of the cladding tubes. The cladding tube walls support many modes of high azimuthal mode order due to their circular shell geometry. Additionally the air-cores of the cladding tubes support modes that are similar in effective index to the core mode, which is an avenue for increased loss in ARFs. Examples of some low-order modes are shown in Fig. 4.9. In order to efficiently discriminate between the central, lowest-order HE_{11} core mode and other modes with a similar effective refractive index, it is necessary to design an automated algorithm for tracking the central core mode in these fibers. Here, in $\text{HE}_{\mu\nu}$, the parameter μ corresponds to the numbers of periods in the azimuthal direction, while ν corresponds to the number of maxima and minima in the radial direction.

The first approach is to find the mode with the largest fraction of its power in the center of the central core. This method will discriminate between the HE_{11} core mode, which has a spatial profile proportional to J_0, the zeroth-order Bessel function of the first kind, as shown in Fig. 4.9(a), and the HE_{21}, TE_{01}, and TM_{01}, which have a spatial profile proportional to J_1, the first-order Bessel function of the first kind, as shown in Fig. 4.9(c)–(d). This method may fail, however, when the core mode is strongly coupled with a cladding tube air mode, as shown in Fig. 4.10.

A second approach is to choose the mode with the lowest loss. However, this method also fails when the core mode couples strongly to either cladding-tube air-core modes or cladding tube dielectric wall modes. A third approach is to choose the mode with the

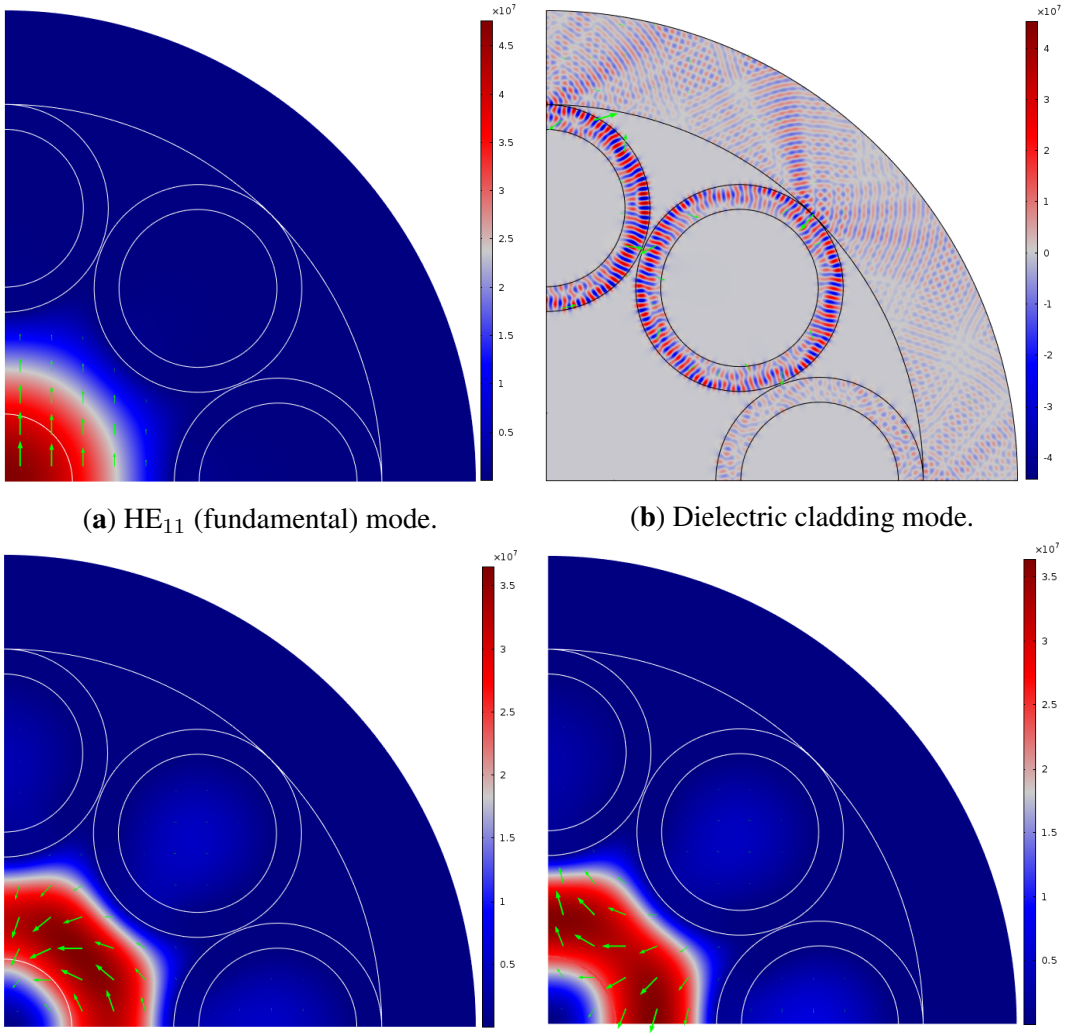

(**a**) HE_{11} (fundamental) mode.

(**b**) Dielectric cladding mode.

(**c**) TM_{01} mode.

(**d**) HE_{21} mode.

Figure 4.9: Low order modes in a typical ARF showing the x-component of the electric field (color) and the transverse magnetic field (arrows): (a) HE_{11} with $n_{\text{eff}} = 0.99979$, (b) dielectric cladding mode with high azimuthal mode order with $n_{\text{eff}} = 0.99937$, (c) TM_{01} with $n_{\text{eff}} = 0.99907$, and (d) HE_{21} with $n_{\text{eff}} = 0.99907$. Note in (c)–(d) the relatively large amount of mode energy in the air cores of the cladding tubes compared to (a).

highest real part of the effective refractive index. Again, this method will fail, even if only modes with effective refractive index less than one are considered, when a cladding dielectric mode with low azimuthal order is close in effective index to the central core

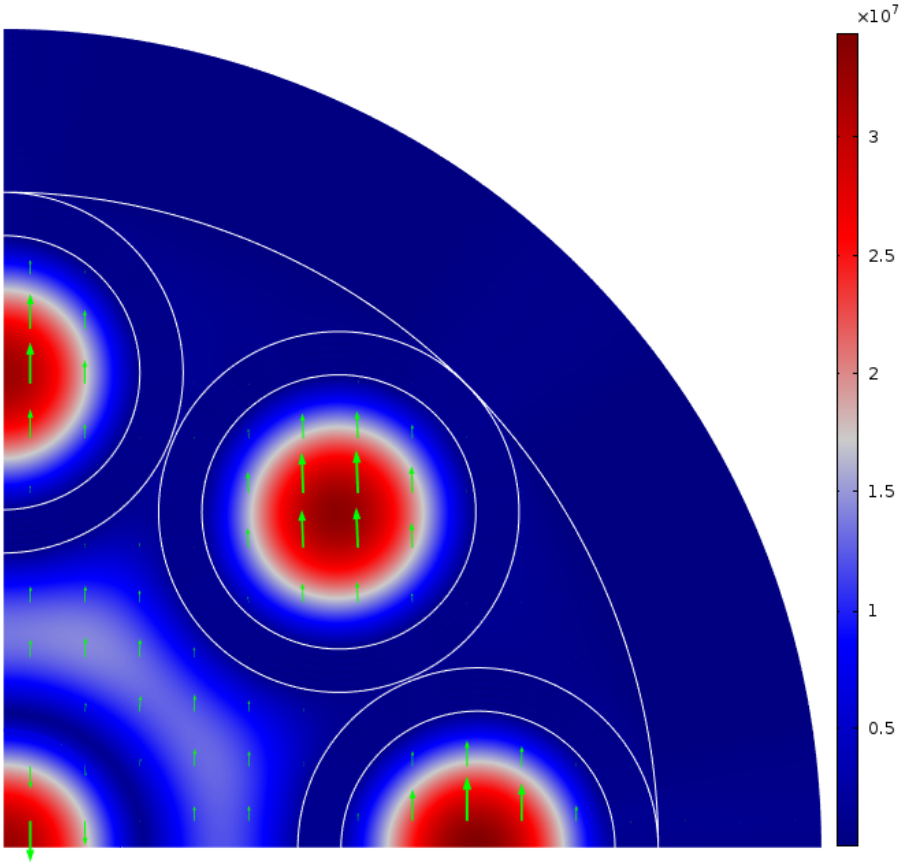

Figure 4.10: A cladding tube air-core mode that couples strongly with modes in the central air core with $n_{\text{eff}} = 0.99897$ showing the x-component of the electric field (color) and the transverse magnetic field (arrows).

mode, as shown in Fig. 4.9(b), or if the central core mode couples strongly with cladding air-core mdoes, as shown in Fig. 4.10. Cladding dielectric tube wall modes have higher effective refractive indices because they are guided in a dielectric of a higher refractive index.

We find that the most accurate method is to consider the two modes with the highest percentage of power in the central air core, and then choose the one with the lowest loss.

Care must also be taken to search for modes that are near the appropriate value of n_{eff}. To do this, we begin by setting the eigenvalue solver shift to a number slightly less than one

and search for a relatively large number of modes, e.g. 12, so that the solver is certain to return the fundamental core mode. For subsequent solutions for the same fiber at different wavelengths, we set the eigenvalue solver shift to be equal to the real part of n_{eff} of the core mode that was previously found, and we search for a reduced number of modes, e.g. 6, in order to reduce the computation time.

We have validated these models using published results for silica fibers [15, 68, 71].

4.2 Geometric considerations

Fig. 4.11 shows a quarter of a typical negative curvature antiresonant fiber geometry. The most important quantities, shown in the figure and discussed here, are the core radius, R_{core}, the cladding tube radius, R_{clad}, the cladding tube wall thickness, t, the cladding tube separtion, d, and the core-to-nested-tube distance, z. Another important quantity, not expressly designated in the figure, is the number of cladding tubes in the fiber, N_{tubes}. The following sections describe each of these parameters in detail.

4.2.1 Cladding tube wall thickness The thickness of the cladding tube walls, t, affects both the overall confinement loss of an ARF and the locations of resonant absorption peaks in the transmission spectrum. In general, the cladding tube thickness should be as small as possible. This reduces the loss in two ways. First, it reduces the number of resonant absorption peaks in the spectrum, and second, it reduces the optical density of states, or the number of modes in the cladding tube walls that can overlap with the core mode. The second consideration is the most important for reducing the overall loss of an ARF.

At certain wavelengths, the mode in the core of an ARF will leak out to the cladding tubes through a resonant tunneling effect [72]. This results in resonant absorption peaks in the transmission spectrum of an ARF. According to the anti-resonant reflecting optical

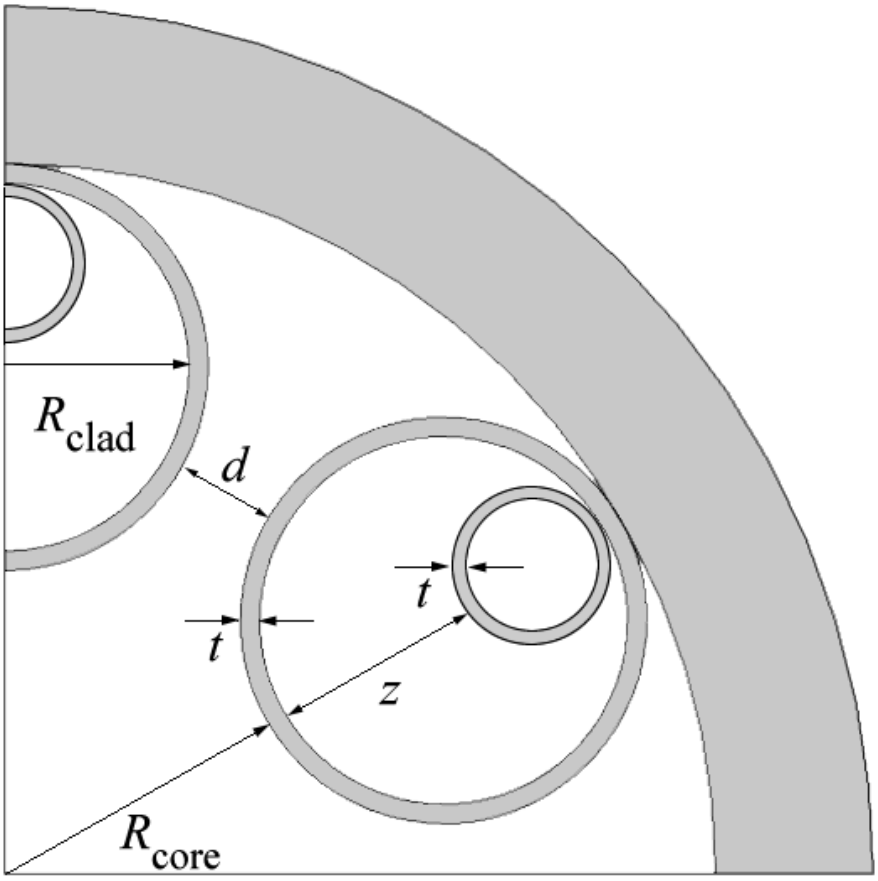

Figure 4.11: A quarter section of a typical fiber geometry with important parameters.

waveguide (ARROW) model of Litchinitser et al. [72], the wavelengths, λ_m, at which these peaks appear depend only on the cladding tube thickness, t, and on the refractive index of the material ($n \approx 2.44$ in the case of As_2S_3 used in this work), according to the equation

$$\lambda_m = \frac{2t\sqrt{n^2 - 1}}{m}, \tag{4.2}$$

where m is an integer denoting the resonant peak. Guided modes with low loss exist for wavelengths longer than the first absorption peak, albeit with potentially increased loss,

and for wavelengths between absorption peaks, but they do not exist for wavelengths close to these peaks. Thus, since guidance occurs over a broad spectrum, the best way to mitigate the impact of these absorption peaks is to reduce the thickness of the cladding tube walls until the first resonant peak, corresponding to $m = 1$, is at a wavelength shorter than the shortest wavelength of interest. However, reduction to this limit is often not practical, especially with a high-index material, such as As_2S_3, in which case the impact of these peaks can be reduced by aligning them with absorption peaks in the atmosphere, i.e. at wavelengths where transmission is already highly lossy due to the absorption of atmospheric gases.

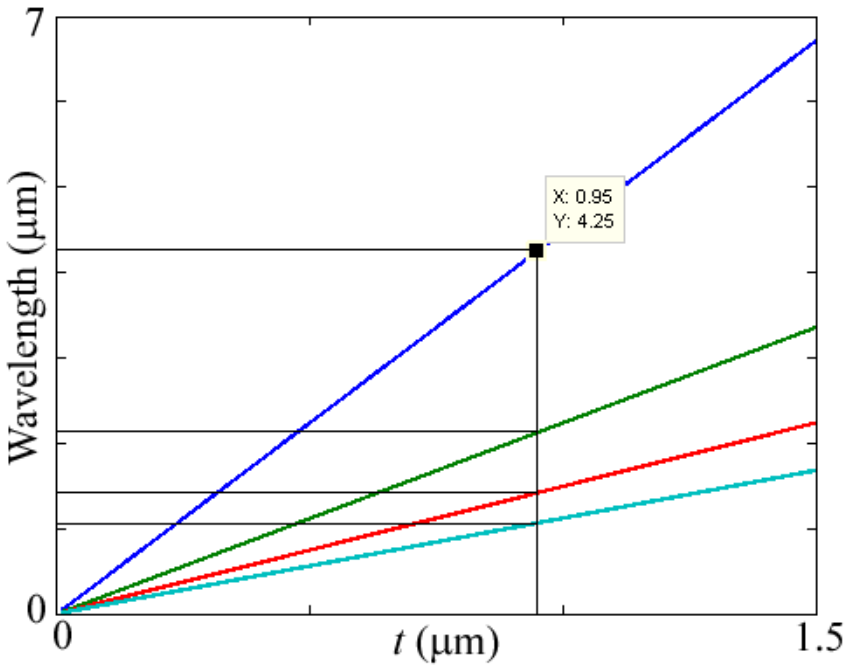

Figure 4.12: Wavelength of absorption peaks λ_m as a function of cladding tube wall thickness t, for $m = 1$ (blue), $m = 2$ (green), $m = 3$ (red), $m = 4$ (cyan). The wavelengths for a thickness of 0.95 μm are delineated with black lines.

Fig 4.12 shows the location of absorption peaks as a function of thickness for a refractive index of $n = 2.45$. It can be seen that the first two absorption peaks can be roughly

aligned with absorption peaks of CO_2 at 4.25 μm and 2.5 μm by choosing a thickness of $t = 0.95$ μm. This value of t yields a good trade-off between the necessity to keep the cladding tube thickness low and the desire to align loss peaks with already-existing atmospheric peaks.

In the case of a low-index glass, such as silica with $n = 1.44$, the resonant absorption peaks occur at shorter wavelengths and more closely together than is the case for As_2S_3, as shown in Fig. 4.13. Hence, it is easier to operate exclusively in the long wavelength transmission band in silica.

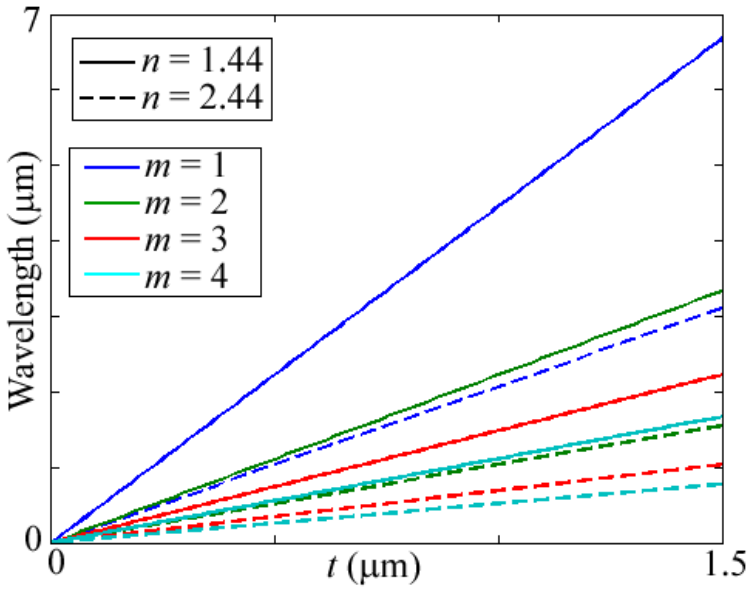

Figure 4.13: Wavelength of absorption peaks λ_m as a function of cladding tube wall thickness t, for $m = 1$ (blue), $m = 2$ (green), $m = 3$ (red), $m = 4$ (cyan) for refractive indices of $n = 1.44$ (dashed lines) and $n = 2.44$ (solid lines).

4.2.2 Cladding tube separation If there is no separation of the cladding tubes, i.e. $d \leq 0$, the optical density of states in the cladding will be high and more cladding modes

will overlap with the core mode, causing increased loss. Therefore, in general, it is advantageous to have some separation between the cladding tubes. Fibers for which the cladding tube separation $d > 0$ are called "nodeless" [68] because the intersection points of the cladding tubes form nodes that are detrimental to the overall loss of the fiber.

Increasing the cladding tube separation presents a trade-off, as it increases the overall bandwidth of the fiber, but simultaneously increases the minimum loss. The opposing effects are 1) that the separation eliminates nodes, whose presence leads to more modes that can couple to the core mode, and 2) increasing the separation allows energy from the core mode to leak out to the jacket through the gaps. An acceptable balance between these effects [68] is achieved for a ratio of $1 < d/t < 6$. For the designs presented in this work, we chose a value of $d/t = 4.2$ or $d = 4.0$ µm.

4.2.3 Cladding tube number The question of how many cladding tubes to include in an ARF is still open. To some degree, the debate is about the trade-off between decreasing the minimum loss and increasing the higher-order mode extinction ratio (HOMER). Many previous studies used 8 cladding tubes because the original design of Pyramikov et al. used eight cladding tubes, but most state-of-the-art designs use six tubes because such designs increase the distance between the core and the jacket, which increases the loss of higher-order modes and may reduce the overall loss.

For an ARF with no separation between the cladding tubes, i.e. $d = 0$, the cladding tube radius depends only on the core radius according to the equation

$$R_{\text{clad}} = \frac{R_{\text{core}}}{(\sin \alpha/2)^{-1} - 1}, \tag{4.3}$$

where α is the angle between tubes, or $360°/N_{\text{tubes}}$. We find $\alpha = 45°$ for ARFs with 8

cladding tubes and $\alpha = 60^\circ$ for ARFs with 6 cladding tubes. Specifically, the ratio of $R_{\text{clad}}/R_{\text{core}} = 1$ for $N_{\text{tubes}} = 6$ and $R_{\text{clad}}/R_{\text{core}} \approx 0.62$ for $N_{\text{tubes}} = 8$. Thus, it can be seen that a design with six cladding tubes has a greater distance between the lossy jacket or cladding support and the core mode than a design with eight cladding tubes.

While a greater distance between the jacket and the core increases the computational complexity of the simulation, it should also decrease the overall loss. However, six-tube designs also have larger cladding air-cores, which may support more modes, thus increasing the overlap with core modes, which may also increase loss. This additional effect is expected to be more evident in fibers without nested elements, since core modes will couple more readily to cladding air-core modes in that case.

A ratio of core-radius to cladding-radius of about 0.65 — close to the value found in an eight-tube fiber — can be shown to be theoretically optimal according to a semi-analytical Bragg reflection theory [71]. However, simulations and experiments have shown that this value is not ideal [68, 71]. A different theoretical and numerical investigation [73] showed that fibers with seven cladding tubes have a lower minimum loss than do six- or eight-tube designs. Also, it has been shown that designs using six cladding tubes also have a larger HOMER [68].

Using a cladding tube thickness of $t = 0.95$ μm, we investigate the effect of using six or eight As_2S_3 cladding tubes, both with and without nested elements. Figure 4.14 shows the results for fibers with six and eight cladding tubes without nested elements. The core size is 54 μm, and the separation between cladding tubes is $d = 4.0$ μm. Thus, the six-tube design has a cladding radius $R_{\text{clad}} = 48$ μm, while the eight-tube design has $R_{\text{clad}} = 31.25$ μm.

Contrary to previous published results for fibers with nested elements [68], when there are no nested cladding tubes, the loss is lower for a fiber with eight cladding tubes com-

pared to six cladding tubes. Note that loss values near the absorption peak are difficult to determine accurately, due to the mixing of modes that occurs there. The loss is lower on the short wavelength side of the absorption peak because this area marks what is traditionally known as the "first" transmission band of the fiber according to the ARROW [72] model, even though guidance (transmission) is possible at longer wavelengths.

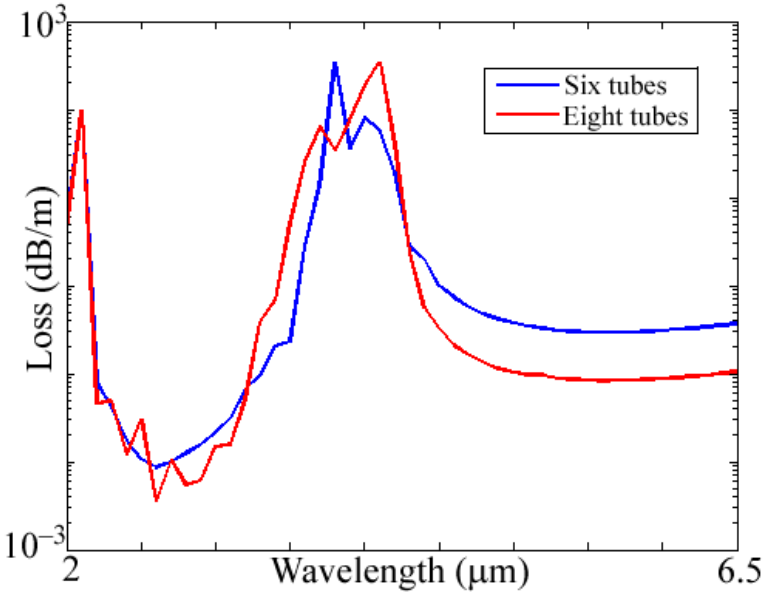

Figure 4.14: Loss as a function of wavelength for an ARF with 6 tubes (blue) and 8 tubes (red) both without nested elements.

This result can be expected since, as mentioned previously, without nested elements, core modes are more likely to couple to cladding-air core modes, especially if those cladding air-cores have a larger radius, as is the case with a six-tube fiber.

Figure 4.15 shows the results for six and eight cladding tubes with nested elements. The results are calculated for a distance between the outer cladding tube and the nested element of $z/R_{\text{core}} = 0.5$, $z/R_{\text{core}} = 0.7$, and $z/R_{\text{core}} = 0.9$. The remaining parameters are the same as for Fig. 4.14. For $z/R_{\text{core}} = 0.5$ and $z/R_{\text{core}} = 0.7$, the differences between

the six-tube design and the eight-tube design are minimal. However, when $z/R_{\text{core}} = 0.9$, the 8-tube fiber has much higher loss, especially for long wavelengths. This result contrasts strongly with the results of [68], which shows orders of magnitude less loss for six-tube fibers than for eight-tube fibers if they both contain nested elements.

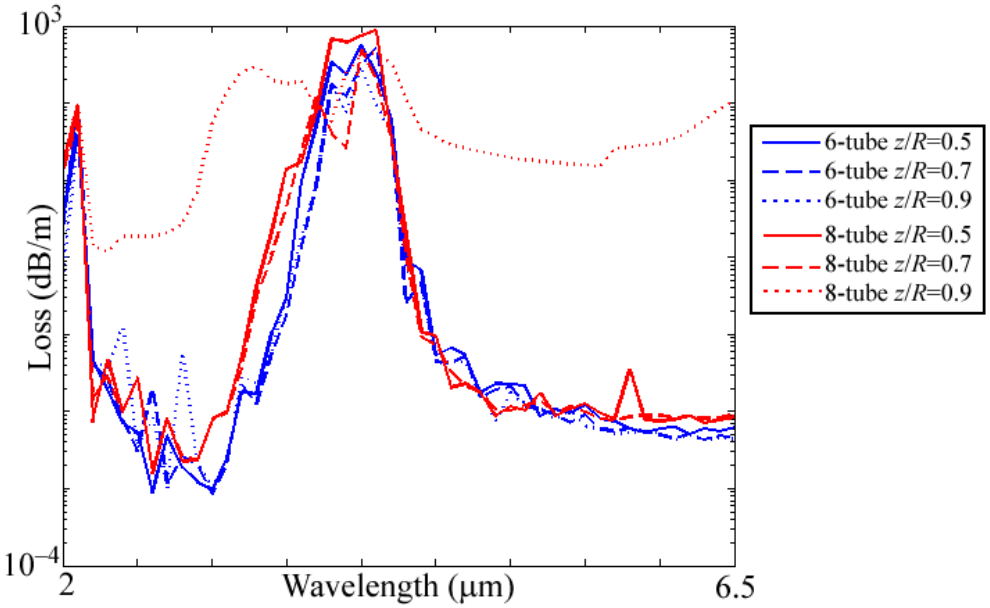

Figure 4.15: Loss as a function of wavelength for an ARF with 6 tubes (blue) and eight tubes (red) that both have nested elements. The distance between the outer cladding tube and the nested elements are $z/R_{\text{core}} = 0.5$ (solid), $z/R_{\text{core}} = 0.7$ (dashed), and $z/R_{\text{core}} = 0.9$ (dash-dot).

One reason for this discrepancy may be the lower loss of As_2S_3 compared to silica. When an ARF contains nested elements, the loss of the central core mode comes mostly from coupling to modes in the cladding dielectric tube walls, rather than modes in the cladding air-core. If the absorption loss of the dielectric (glass) cladding tube walls is significantly lower than the confinement loss, which may be about the same for the two

geometries, the confinement loss will dominate and there will be little difference between fibers with a different number of cladding tubes.

The loss for the fibers with nested elements are lower in both cases than for the fibers without nested elements. Since the results are approximately the same for all cases with nested elements, except the eight-tube fiber with nested elements and $z/R_{\mathrm{core}} = 0.9$, all fibers used in the rest of this work will use six cladding tubes.

An additional advantage is that six-tube fibers are much easier to fabricate than eight-tube fibers due to the reduced geometric complexity.

4.2.4 Nested elements Poletti [68] showed that including so-called "nested" elements, or additional, smaller cladding tubes nested inside of the larger cladding tubes can reduce the overall loss of an ARF by 1–2 orders of magnitude.

Figure 4.16 shows the effect of including nested elements. Indeed, in the chalcogenide case, the minimum loss is reduced by about 1.5 orders of magnitude, and the overall loss is consequently also reduced. We therefore find that nested elements are essential to a low-loss ARF.

Figure 4.17 shows a particularly lossy case of the fundamental core mode for a fiber with and without nested elements. It is clear that the loss in the fiber with nested elements is due to coupling of the core mode with modes in the glass walls of the cladding tubes, while in the fiber without nested elements, the core mode couples to modes in the air-core of the cladding tubes, which have a greater spatial extent. This greater spatial extent means there is more mode energy in the lossy jacket of the fiber, which increases the loss compared to the nested element fiber. An additional advantage is that the locations of the mode coupling to glass structures is closer to the center of the fiber for the fiber with nested elements than for the fiber without nested elements. This fact also reduces the loss since the absorption

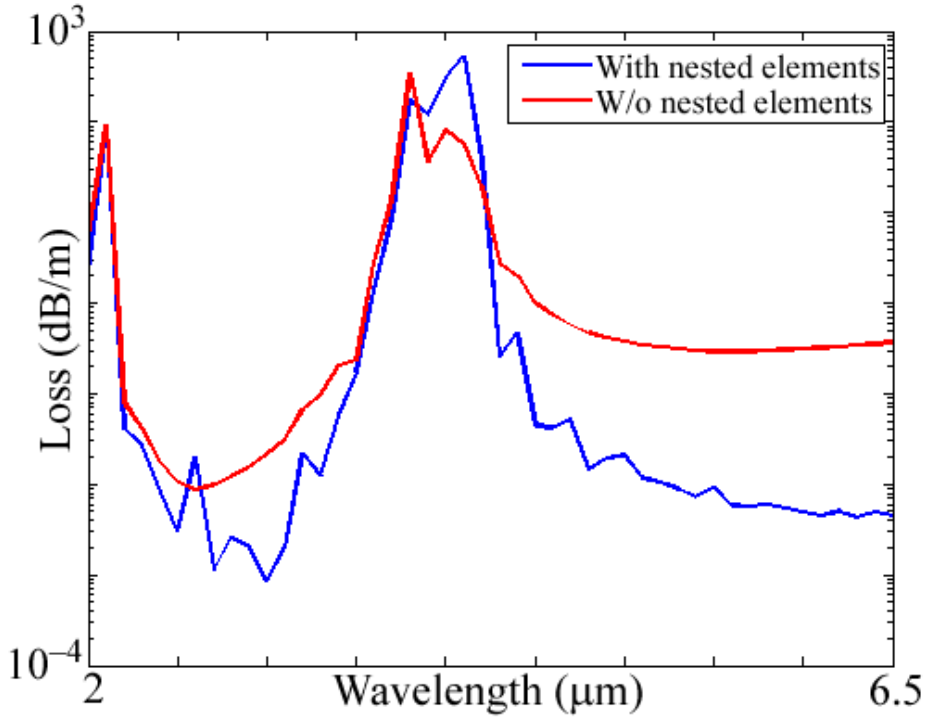

Figure 4.16: Loss as a function of wavelength for an ARF with 6 tubes with nested elements (blue) and without nested elements (red). The distance between the outer cladding tube and the nested elements is $z/R_{\text{core}} = 0.7$ in both cases.

in the glass is fixed and independent of its spatial location, while the loss in the jacket is greater for modes closer to the outer edge of the fiber.

4.2.5 Core radius In general, increasing the core radius increases the bandwidth of an ARF, especially for longer wavelengths, because it increases the distance between the core and the lossy jacket. However, increasing the core radius also decreases the mode quality of the fiber by allowing more higher-order core modes. These higher-order modes will also couple more readily to cladding modes due to their spatial proximity, which increases the overall loss of a fiber. Therefore, we expect that there should be a decreasing marginal

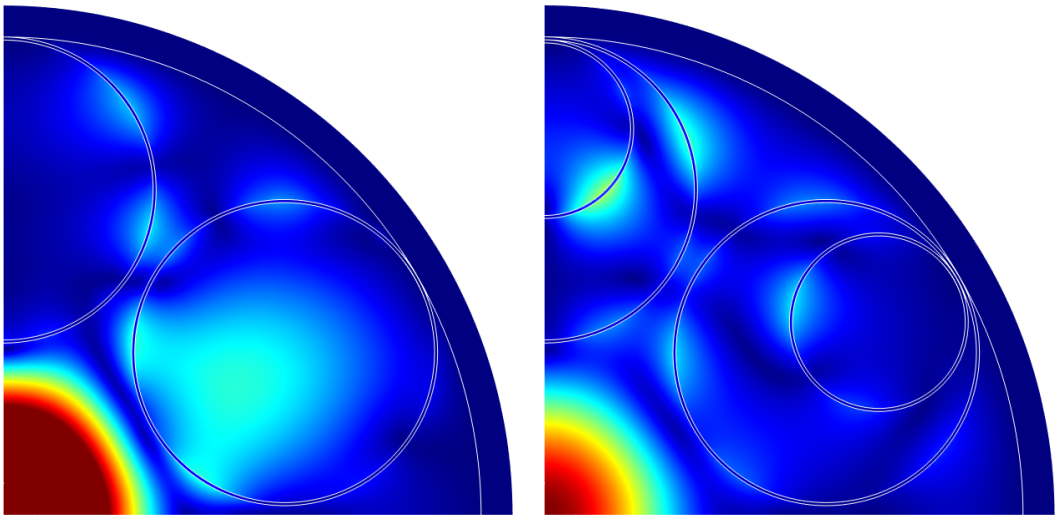

(**a**) Without nested elements. (**b**) With nested elements.

Figure 4.17: Fundamental core mode (the norm of the electric field) for a fiber with and without nested elements at $\lambda = 3.9$ µm. The color scale is the same for both figures.

efficacy to increasing the core size.

Figure 4.18 shows the effect of increasing the core size for a fiber with a geometry similar to the 8-cladding tube design originally presented by Pyramikov et al. [15], except with As_2S_3 instead of silica. The ratio of the inner cladding tube diameter to the outer cladding tube diameter, which sets the thickness, t, of the cladding tubes, is kept fixed at 0.76. Additionally, the ratio of the cladding tube diameter to the core diameter is also fixed. Although this cladding tube wall thickness is not optimal and the fixed ratio increases the cladding tube thickness as the core radius is increased, which increases the number of absorption peaks, this figure does exhibit the predicted behavior. Both the average loss, shown in Fig. 4.19, and the minimum loss decrease, but at a decreasing rate, as the core size is increased. The average loss increases for a core radius of 250 µm due to the increased number of absorption peaks present for a larger cladding tube thickness. The diminishing returns would not be so pronounced in Fig. 4.19 if the cladding tube thickness was kept

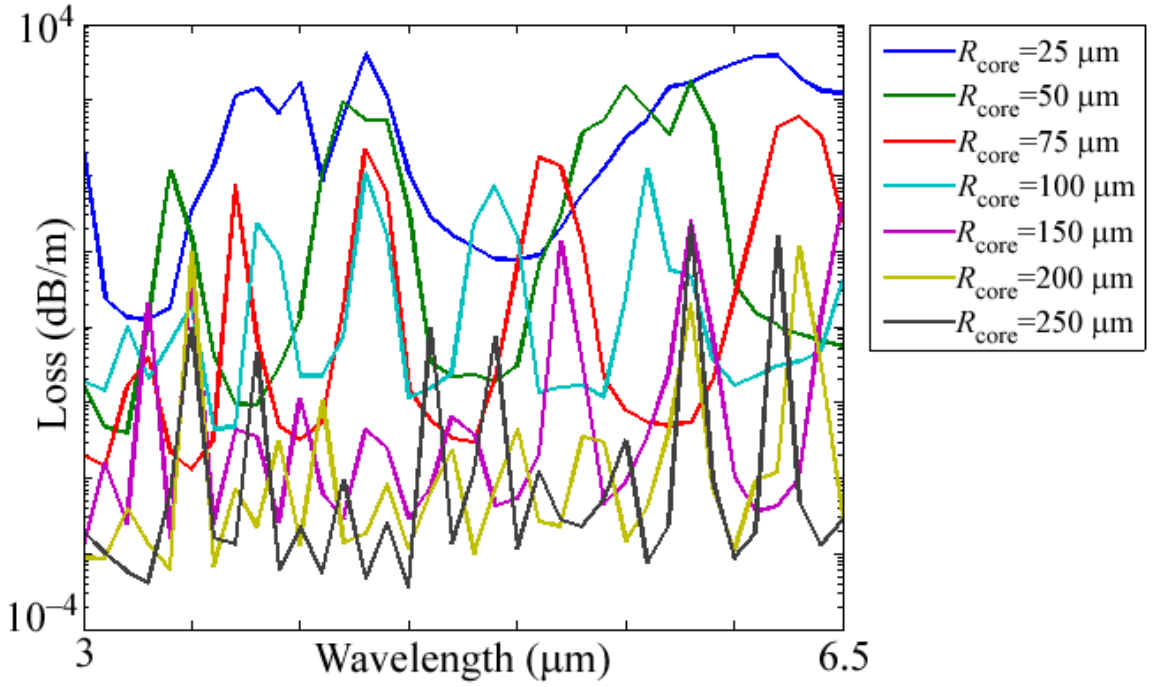

Figure 4.18: Loss as a function of wavelength for different core radii for fiber parameters taken from [15].

constant.

Figures. 4.18 and 4.19 show that the benefit of increasing the core size of an eight-tube fiber levels off after $\sim$ 200 μm. It is important to note that modeling an eight-tube ARF with a core size greater than 200 μm is very difficult and cannot yield accurate results for short wavelengths. For six-tube designs, this limitation is even stronger because of the increased size of the cladding relative to the core radius.

Again, the fiber parameters taken from [15] are not optimal. Particularly, the fixed ratio of the inner to outer cladding tube diameters increases the cladding tube thickness as the core radius increases. This parameter choice increases the number of absorption peaks present in the spectrum and increases the overall loss. Thus, to truly isolate and elucidate the effect of increasing the core radius, the cladding tube thickness should be kept constant.

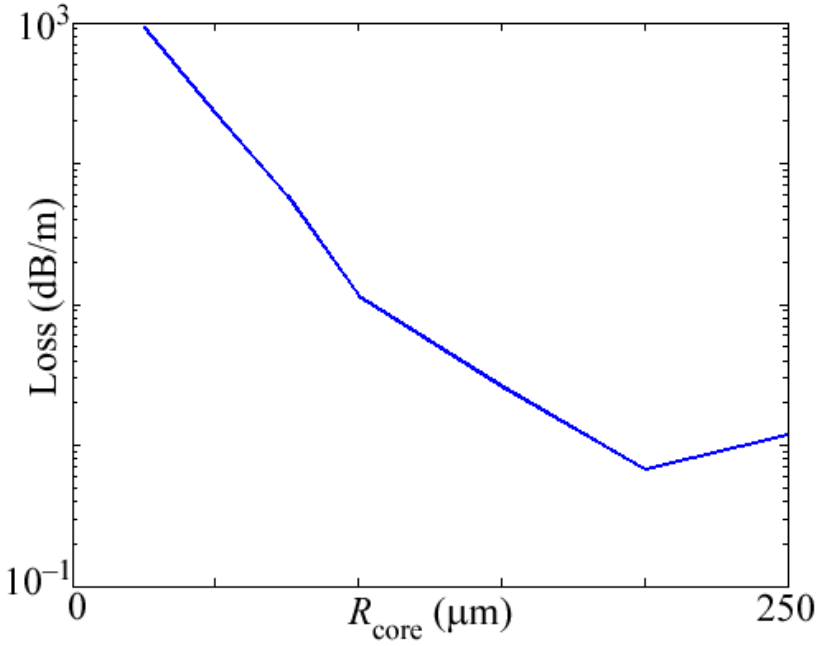

Figure 4.19: Average loss over 3–6.5 μm as a function of core radius for the suboptimal fiber design, which increases t as R_{core} increases.

Figure 4.20 shows the effect of increasing the core radius for a fiber with six cladding tubes, containing nested elements with $z/R_{\text{core}} = 0.7$, and with a constant cladding tube wall thickness of $t = 0.95$ μm. The loss decreases as the core radius increases from 25 μm to 100 μm, but, again, at a decreasing rate.

The saturation of the loss as the core radius increases is especially visible in the first transmission band between 2.2–4μm. In this band, the decrease in minimum loss saturates for core radii of $R_{\text{core}} > 50$ μm. That is, increasing the core radius past 50 μm does not significantly decrease the minimum loss over this wavelength range.

However, increasing the core radius does increase the bandwidth of this transmission band. This increased transmission bandwidth is due to decreased coupling between core modes and cladding tube wall dielectric modes for larger core radii. This effect is demon-

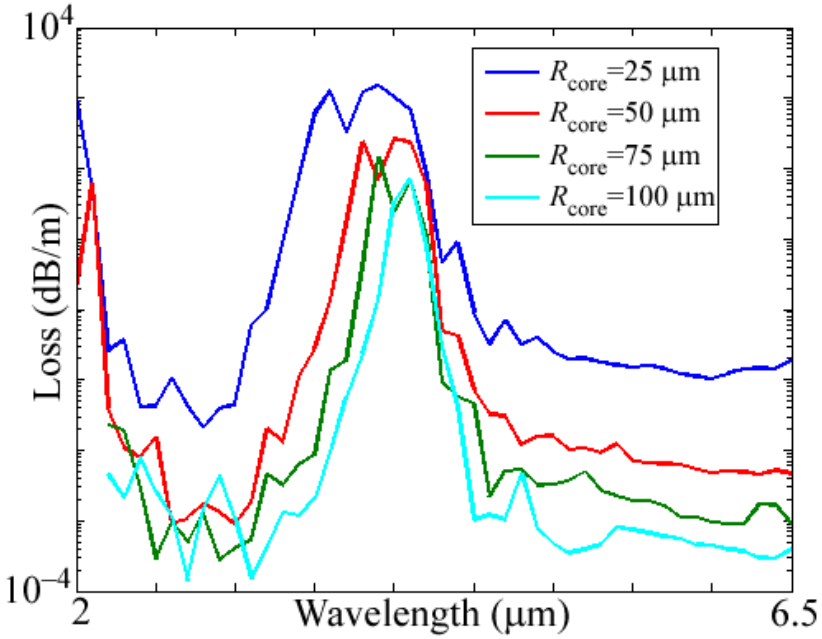

Figure 4.20: Loss as a function of wavelength for the lowest-loss mode of a six-tube fiber with different core radii and $t = 0.95$ μm, $z/R = 0.7$, and $d = 4.0$ μm.

strated by Fig. 4.21, which shows the fundamental core mode for a wavelength of 3.6 μm for a fiber with a 25 μm core radius and fiber with a 100 μm core radius. Though the mode in the 100 μm fiber extends farther toward the cladding tubes, the mode is relatively well confined to the central core and does not couple strongly to cladding tube wall dielectric modes, as in the case of a 25 μm core.

It should be recalled that the effective refractive index of a mode is always less than the refractive index of the medium in which it is confined, in this case, $n_{\text{eff}} < 1$. The degree to which the effective index is less than the guiding medium (vacuum) index indicates how well-confined the mode is. Therefore, the mode in Fig. 4.21(a), which has an effective refractive index $n = 0.99882$, is less well-confined than the mode in Fig. 4.21(b), which has an effective refractive index $n = 0.99992$.

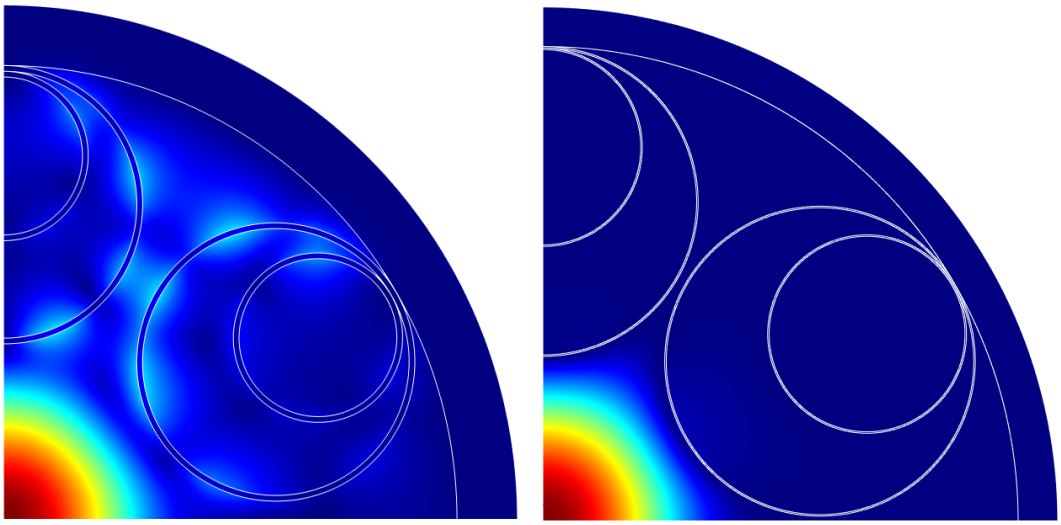

(**a**) Fundamental mode for $R_{\text{core}} = 25$ µm and $\lambda = 3.6$ µm.

(**b**) Fundamental mode for $R_{\text{core}} = 100$ µm and $\lambda = 3.6$ µm.

Figure 4.21: Fundamental core mode for a fiber with a core radius of (a) 25 µm and (b) 100 µm (not to scale). The wavelength in both cases is $\lambda = 3.6$ µm.

4.2.6 More nested elements As demonstrated by [68,69], including more nested elements in some configuration can significantly reduce the confinement loss of an ARF. This effect is achieved by further reducing the overlap between core modes and modes in the cladding tube air-cores and cladding tube dielectric walls. Figure 4.22 shows the effect of including doubly-nested elements and adjacent nested elements. In this study, all geometric parameters are the same as for the previous studies for each fiber, except that different numbers of nested elements are included. For the fiber with doubly-nested elements, the second nested elements have a diameter that is equal to half of the diameter of the first nested element. For the adjacent nested element fiber, the ratio of the radius of the inner adjacent nested tubes, R_i, to the radius of the larger, outer tubes is given by

$$\frac{R_i}{R_{\text{clad}}} = \frac{1}{2(1+\sqrt{2})}. \tag{4.4}$$

From this nominal value, the radius is decreased by 1 µm, to eliminate nodes. This adjacent nested ARF has very similar dimensions to the fiber proposed in [69].

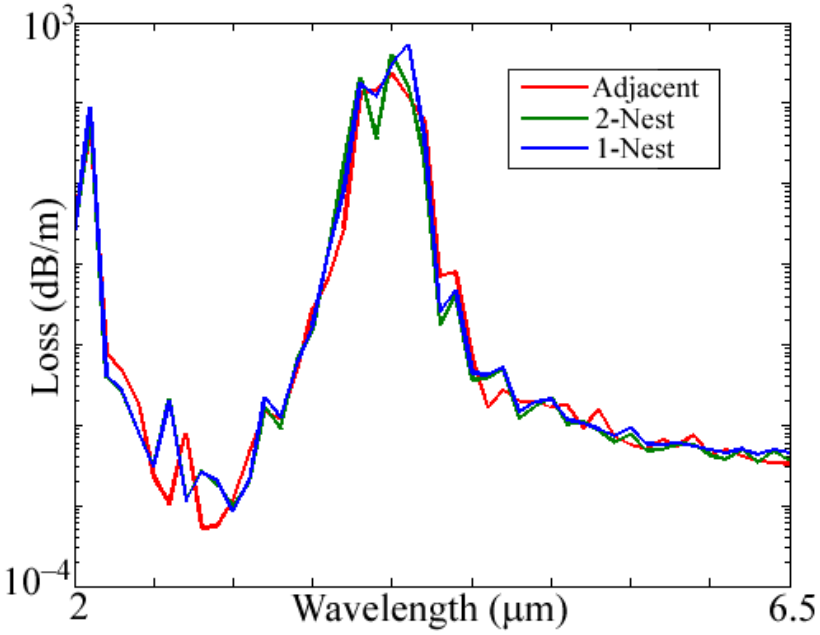

Figure 4.22: Loss as a function of wavelength for a fiber with double-nested elements (green) and adjacent nested elements (red) and single-nested elements (black).

It can be seen that including these further nested elements does not significantly decrease the overall loss of the fiber. A similar result was found in [69], which showed that, while including doubly-nested or adjacent-nested tubes does indeed decrease the confinement loss of the fiber, the overall loss of the fiber was dominated by material absorption in silica. Hence, reducing the confinement loss could not significantly reduce the overall loss of the fiber. The same appears to be true for As_2S_3.

It has also been shown that fibers with adjacent nested elements are robust to variations in the location of the adjacent nested elements [69]. This fact increases the advantage gained by incorporating these elements into a fiber design, compared to a fiber with singly-

nested elements. However, these results show that the best way to decrease the loss of an As_2S_3 ARF is to increase the core radius, rather than to add complexity to the geometry, especially for longer wavelengths.

4.3 An optimal fiber geometry

From the results of the preceding section, a design for an optimal As_2S_3 fiber can be deduced. The fiber parameters chosen for this optimal design are listed in Table 4.1. The core radius was chosen to be as large as possible, while still being manageable on a computer. The cladding radius is approximately equal to the core radius, which is determined by the 6-tube design. The cladding tube wall thickness was chosen to match atmospheric absorption peaks, and the cladding tube separation was chosen to give a balance between the transmission bandwidth of the fiber and its minimum loss.

Parameter	**Value**	**Unit**	**Description**
R_{core}	100	μm	Core radius
R_{clad}	98	μm	Cladding tube radius
t	0.95	μm	Cladding tube wall thickness
d	4.0	μm	Cladding tube separation
d/t	4.2	–	Cladding tube thickness to separation ratio
N_{tube}	6	–	Number of cladding tubes

Table 4.1: Parameter values used for initial ARF design.

This fiber uses single-nested elements, since such a fiber should be easier to fabricate than an adjacent-nested or doubly-nested fiber, with no significant increase in overall loss.

The transmission spectrum of the proposed geometry is shown in Fig. 4.23. As expected, the loss increases rapidly for wavelengths near the designed resonant absorption peak around 4.25 μm.

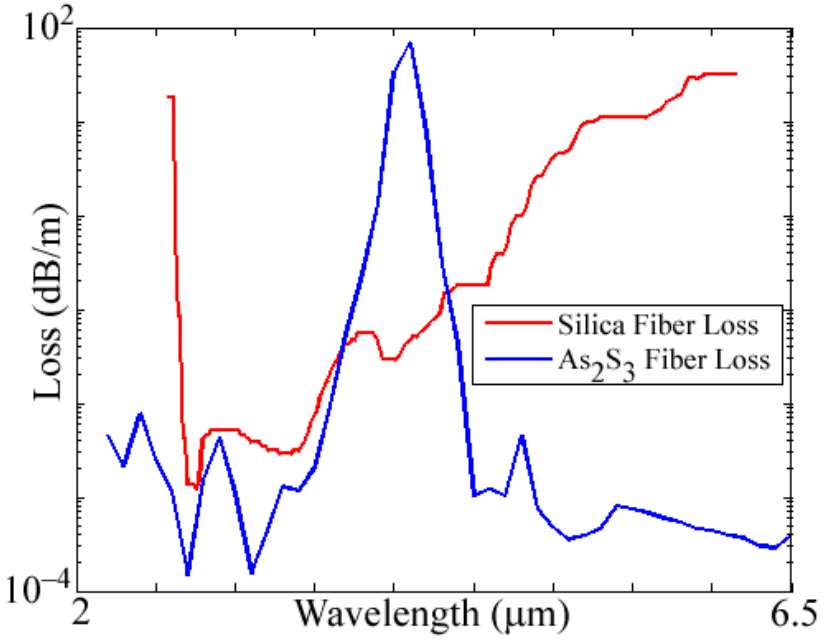

Figure 4.23: Loss as a function of wavelength for the proposed fiber design with parameters shown in Table 1 (blue). The fiber proposed by Habib et al. in [69] (red) is shown for comparison.

Figure. 4.23 also compares this fiber design to the adjacent nested antiresonant fiber (ANAR) design in silica proposed by Habib et al. [69]. The fiber proposed in this dissertation has a larger core radius than the fiber in [69], and it also has single nested elements as opposed to adjacent nested elements. The material differences and the different thickness of the cladding tubes (0.95 μm vs 1.26 μm) also place the resonant absorption peaks at different wavelengths. While the absorption peak for the silica fiber is at 2.5 μm, the absorption peak for the fiber proposed in this dissertation is at 4.25 μm. Aside from this resonant absorption peak at 4.25 μm, the loss for the As_2S_3 fiber proposed here is lower than that in [69], especially for longer wavelenghts. Indeed, at a wavelength of 6 μm, the fiber proposed in this dissertation has a loss that is lower by 5 orders of magnitude. This decrease in loss is mostly due to the decreased absorption in As_2S_3 as compared to silica.

The change in the real part of the effective refractive index of the fundamental core mode for the optimal As_2S_3 fiber is shown in Fig. 4.24. Note that the effective refractive index does not change smoothly near the resonant absorption peak since mode coupling is strong and variable for those wavelengths.

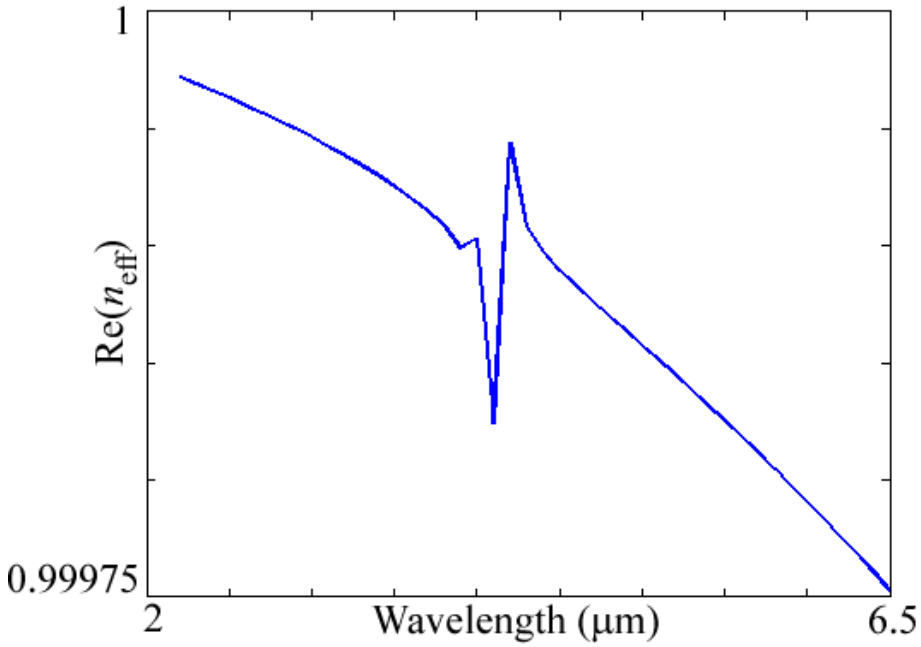

Figure 4.24: Fundamental mode effective refractive index as a function of wavelength for the proposed fiber design.

The change in n_{eff} over the wavelength range considered (2.0–6.5 μm) is less than 0.025%. Thus, the dispersion of this fiber low. Specifically, even including the resonant absorption peak, the group velocity dispersion parameter, D, defined as

$$D = -\frac{\lambda}{c}\frac{\mathrm{d}^2 n}{\mathrm{d}\lambda^2} \tag{4.5}$$

is less than one part in 10^{-10}.

4.4 Fabrication tolerance

In this section, we perturb some parameters of the fiber to study the effect of imperfect fabrication. Imperfect fabrication is more likely to be a problem with soft glasses like As_2S_3 than with silica. Therefore, it is important to know how the performance of a fiber will degrade with perturbations to the parameters. The perturbations we study are 1) a nonconstant cladding tube wall thickness on all cladding tubes, 2) a single cladding tube with a different diameter, 3) a single cladding tube with a different wall thickness, and 4) a "key" structure in the jacket to support the nested cladding tubes.

The fibers we study in this section have a 54 μm core radius. Though this value is suboptimal, the effect of the perturbations on the fiber should be essentially unchanged as the core radius changes. Therefore, to reduce the computational complexity, a smaller diameter fiber was used to study these effects.

4.4.1 Nonconstant cladding tube thickness The first such parameter we study is the thickness of the cladding tube walls. In this study, the thickness of the cladding tube wall is equal to its design value on the core-side of the cladding tube but increases towards the jacket-side of the cladding tube. This imperfect structure is implemented by decreasing the radius of circle that delineates the inner-cladding tube wall and shifting it along the radial direction towards the center of the fiber. Figure 4.25 shows the structure of the fiber for $t_{\text{diff}} = t_2 - t_1 = 4$ μm, where t_2 is the thickness on the jacket-side of the cladding tube, and t_1 is the thickness on the core-side of the cladding tube. In this study, all the cladding tubes have this same imperfection. We study three particular perturbed fibers, where the difference between the thickness on the jacket-side of the cladding tube, t_2, is $t_{\text{diff}} = 1$, 2, and 4 μm thicker than on the core-side of the cladding tube, $t_1 = 0.95$ μm. We study the cases of fibers having these imperfections with and without nested elements.

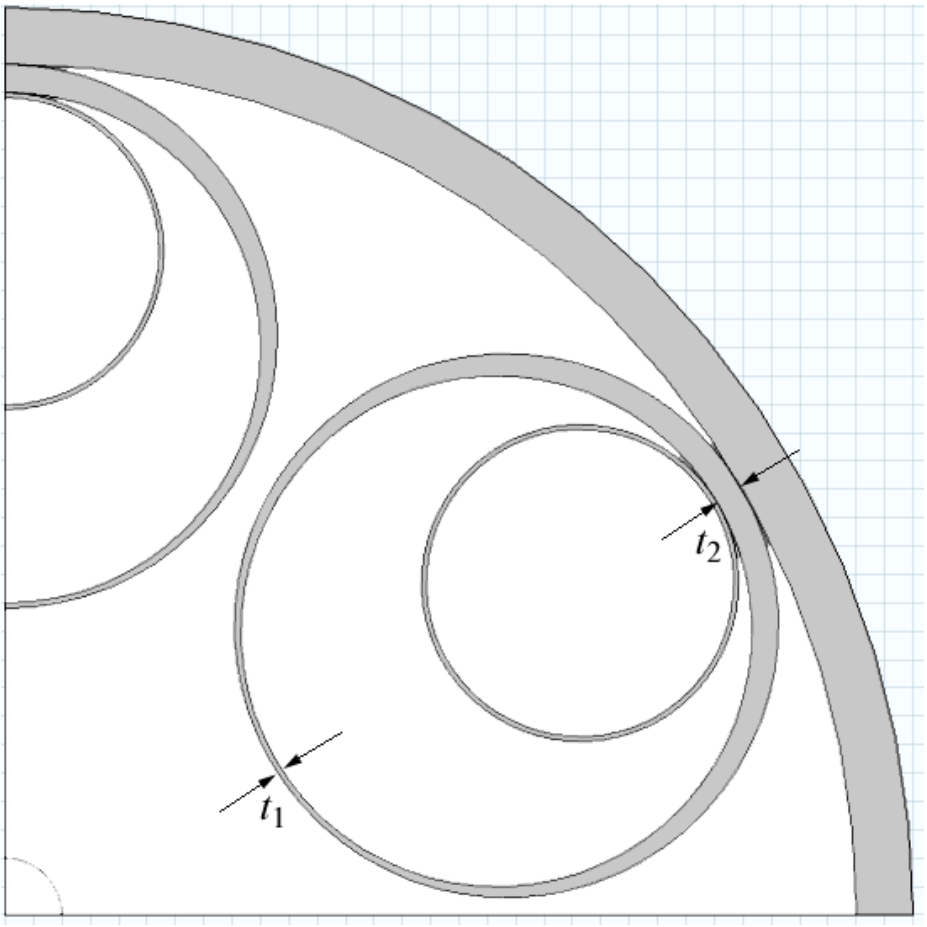

Figure 4.25: Geometry of a fiber with nonconstant tube thickness. The cladding tube wall thickness increases from its nominal value on the core-side of the cladding tube, t_1, towards the jacket-side of the cladding tube where it is equal to t_2.

The results for the fibers without nested elements are shown in Fig. 4.26. Increasing the cladding tube wall thickness on the jacket-side of the cladding tube increases the bandwidth of the high-loss resonant absorption peaks, especially on the long-wavelength side of the peak. Additionally, it increases the minimum loss in the transmission bands between the peaks. As expected, the effect is worse when the thickness difference increases. However, even for a thickness difference of $t_{\text{diff}} = 1$ µm, the minimum loss in the transmission bands increases by almost an order of magnitude over the baseline result, where the wall

thickness is constant over the circumference of the cladding tube.

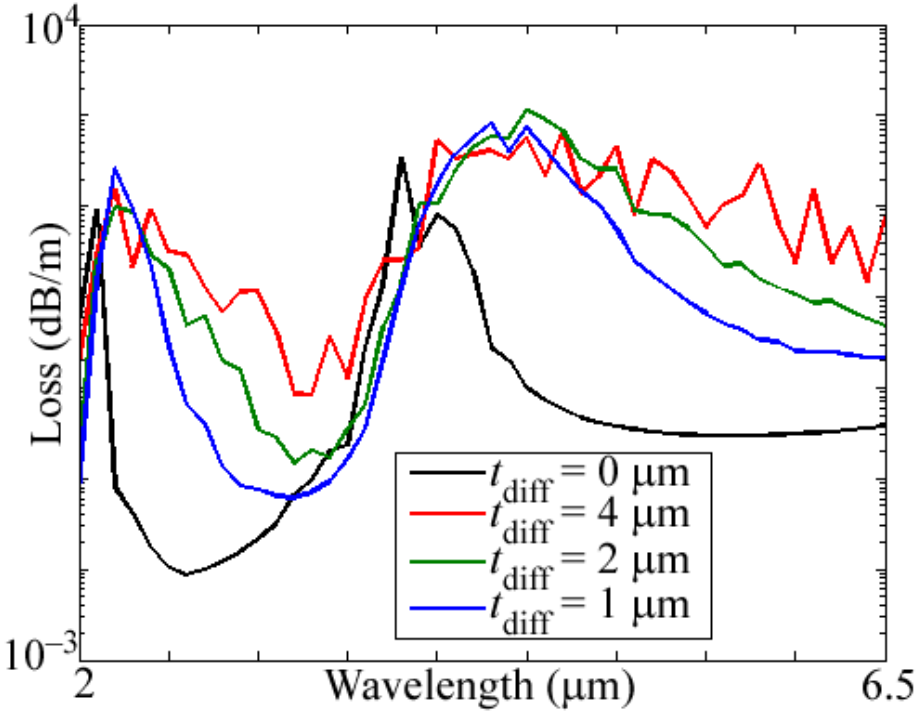

Figure 4.26: Loss as a function of wavelength for the a fiber with a nonconstant cladding tube thickness and no nested elements for $t_{\text{diff}} = 1$ (blue), $t_{\text{diff}} = 2$ (green), $t_{\text{diff}} = 4$ (red), $t_{\text{diff}} = 0$ or a constant wall thickness (black).

This effect is not entirely expected. For core modes to couple to lossy cladding tube modes, they must resonantly tunnel through the cladding tube walls. This tunnelling should only happen on the core side of the cladding tube wall, where the cladding tube thickness is the same as the baseline study. This indicates that for wavelengths in the transmission bands, the core modes couple more readily to modes in the cladding tube walls, as opposed to modes in the cladding tube hollow cores.

The results for the fibers with nested elements are shown in Fig. 4.27. In this case, the nested elements have a constant cladding tube wall thickness, even though the outer cladding tubes do not. Still, as in the case with no nested tubes, a small difference in

the thickness of the cladding tube wall on one side of the cladding tube results in greatly increased loss, especially on the long-wavelength side of the absorption peaks near 2.1 µm and 4.25 µm.

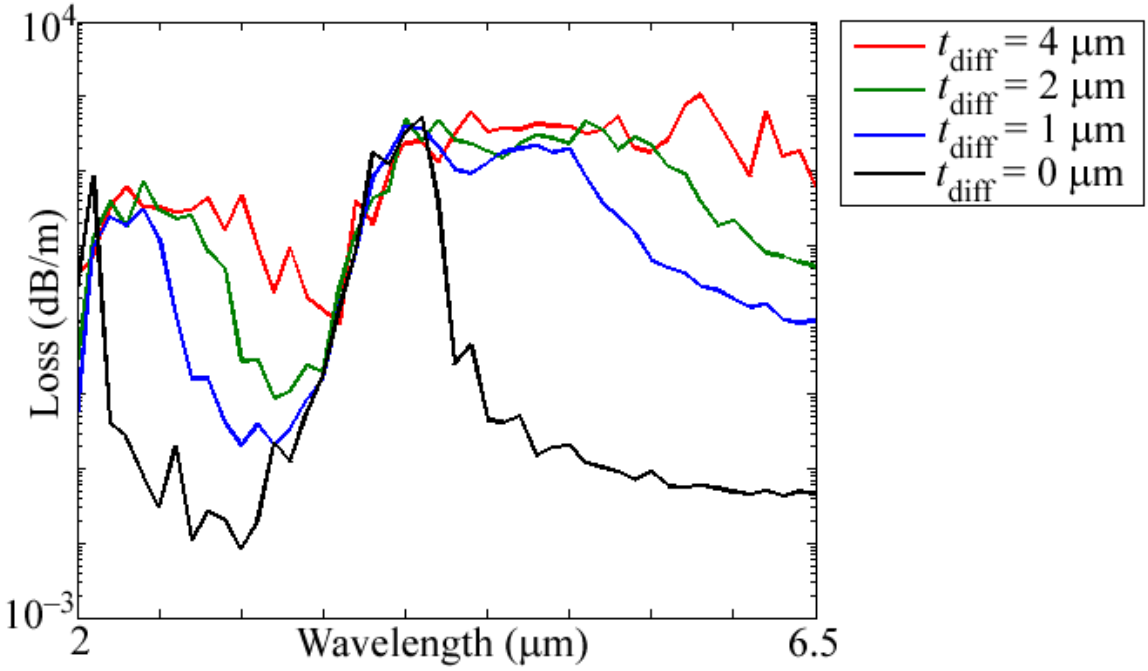

Figure 4.27: Loss as a function of core radius for the a fiber with a nonconstant cladding tube thickness and constant-thickness nested-elements for $t_{\text{diff}} = 1$ (blue), $t_{\text{diff}} = 2$ (green), $t_{\text{diff}} = 4$ (red), $t_{\text{diff}} = 0$ or a constant wall thickness (black).

4.4.2 A single cladding tube with a different diameter In this section, we simulate the effect of having a cladding tube with a diameter that is different from the design value. We simulate this by including half of the geometry with appropriate periodic boundary conditions and change one tube that is half-included in the geometry, so that only one cladding tube in the total geometry has a different size. We show a picture of the simulated geometry, which is half of the actual fiber, showing the different cladding tube dimension in Fig. 4.28. Note, on the left side of the figure, the increased distance between cladding

tubes of different diameter as opposed to cladding tubes of the same diameter. Also, since the ratio of z/R is fixed, the nested tube inside the tube with a different diameter will also have a different diameter than the nested tubes in the rest of the fiber.

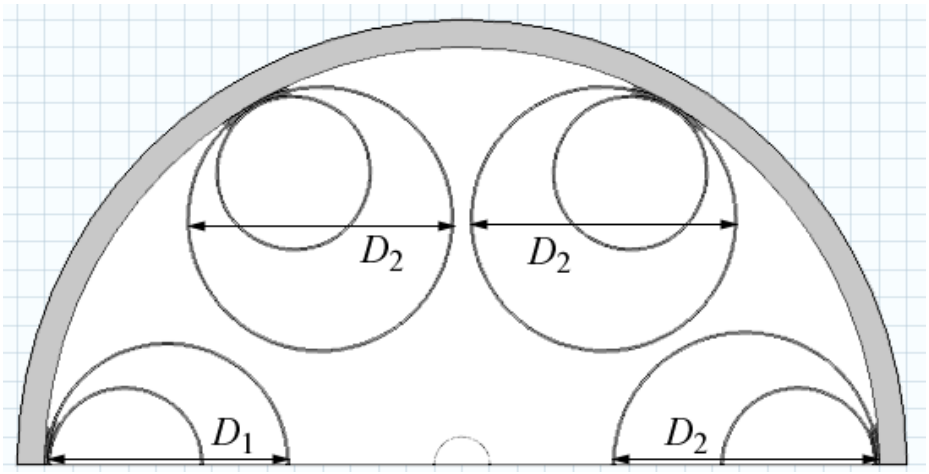

Figure 4.28: Half-fiber geometry with a single differently-sized cladding tube. In this figure $D_1 < D_2$, but we also study the case of $D_1 > D_2$.

Figure 4.29 shows the loss for a fiber with a single cladding tube radius increased by 10%, decreased by 10%, and with no change (for reference). Both the perturbed fibers have a larger loss almost everywhere in the transmission band than does the the baseline fiber. Interestingly, however, the perturbed fiber with a 10% increase in cladding tube radius shows a smaller increase in loss almost everywhere in the spectrum as compared to the perturbed fiber with a 10% smaller cladding tube radius. Also, the loss is only slightly increased at all for certain wavelengths.

This result shows the relative robustness of the cladding tube separation parameter, d, to variations. As shown in [68], loss is minimized for $1 < d/t < 6$, so the increase in cladding tube diameter, which decreases the cladding tube separation between two tubes beyond its design value to $d/t \approx 1$ does not increase the loss significantly. However, when

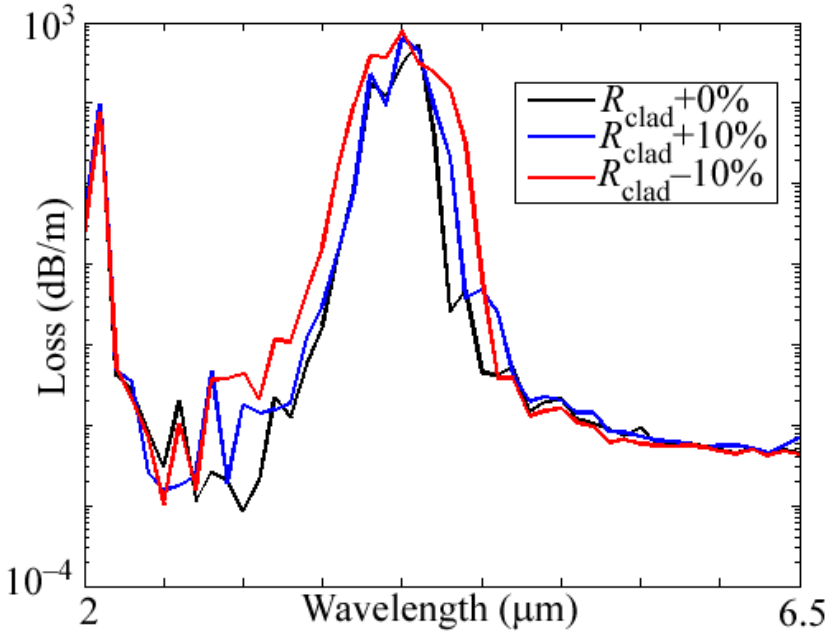

Figure 4.29: Loss as a function of core radius for the a fiber with a single cladding tube of a different size when the cladding tube radius is increased by 10% (blue), or decreased by 10% (red), relative to a fiber with no change in the cladding tube radius (black).

the cladding tube diameter is decreased, we obtain $d/t \approx 8$, which is outside the range of values previously found to be acceptable. Hence, the loss increases by a greater amount, especially at longer wavelengths, which are more likely to leak out through a gap between cladding tubes because of the larger effective mode area.

However, in both cases, the difference between the baseline result and the results for the perturbed fiber are small, especially compared to the effect of a nonconstant cladding tube wall thickness as in Sec. 4.4.1. Further, a varying cladding tube diameter may influence the mode quality of the core mode, so that it is no longer circularly symmetric, which could be detrimental for some applications.

4.4.3 A single cladding tube with a different thickness In this section, we simulate the effect of having a cladding tube with a tube wall thickness, t, that is different from the design value. This study is carried out in a similar manner to the previous study, except that instead of changing the diameter of a single cladding tube, we change its tube wall thickness. In this study, we do not change the tube wall thickness of the nested tube inside the perturbed tube. Figure 4.30 shows the loss for a fiber with a single cladding tube wall thickness increased by 10%, decreased by 10%, and with no change (for reference).

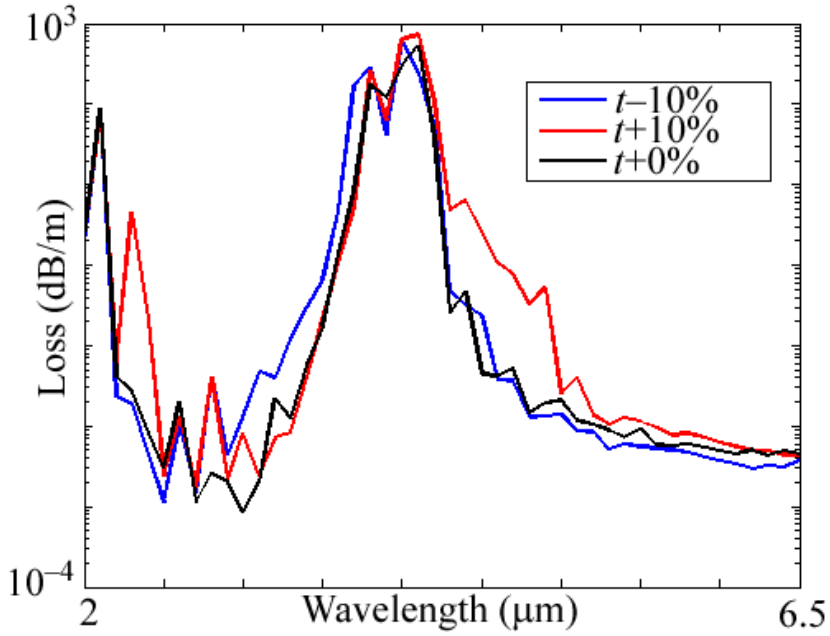

Figure 4.30: Loss as a function of core radius for a fiber with a single cladding tube with a different wall thickness for a cladding tube wall thickness decreased by 10% (blue), increased by 10% (red), or unchanged (black).

As expected, changing the tube wall thickness increases the loss near the transmission band. Increasing the thickness increases the loss on the long-wavelength side of the absorption peak, while decreasing the thickness increases the loss on the short-wavelength

side of the absorption peak. This behavior can be predicted from the ARROW [72] model, as explained in Sec. 4.2.1. In an actual fiber, if the tube wall thickness both increases and decreases for different cladding tubes, the increase in loss will be spectrally broadened on both sides of the absorption peaks, which is a worst-case scenario.

Decreasing the cladding tube thickness should decrease the loss in the transmission bands, because the reduced-thickness cladding tubes support fewer modes that can couple to core modes. This effect is evident in Fig. 4.30, especially for longer wavelengths. However, the decrease in loss at longer wavelengths is still small, and does not compensate for the increase in loss from the broadening of the transmission band. Hence, the fiber with a larger tube wall thickness has significantly higher loss in the transmission bands than either the baseline fiber or the fiber with a smaller wall thickness.

4.4.4 "Key" sections The orientation of the nested tubes inside the cladding tubes can be difficult to maintain in practice while drawing a fiber. A way to minimize the movement of the nested tubes relative to the larger tubes is to include so-called "key" sections in the fiber jacket or outer cladding that hold the nested tubes in place. An example of such a fiber geometry is shown in Fig. 4.31.

In this section, we study the influence of these key sections on the loss of the fiber. We use a fiber with six cladding tubes and a core radius of $R_{\text{core}} = 54$ μm. All the other parameters are the same as in Sec. 4.2.4, except that for the inclusion of the extra key sections. In this model, we take the outer ring of the key section to have a refractive index of $n = 1.5 - i1 \times 10^{-4}$, which approximates the refractive index of silica. The inside circle of the key sections is assumed to be As_2S_3.

Figure 4.32 shows the results for a fiber with and without key sections. Aside from the inclusion of the key sections, all other fiber geometric and material parameters are the

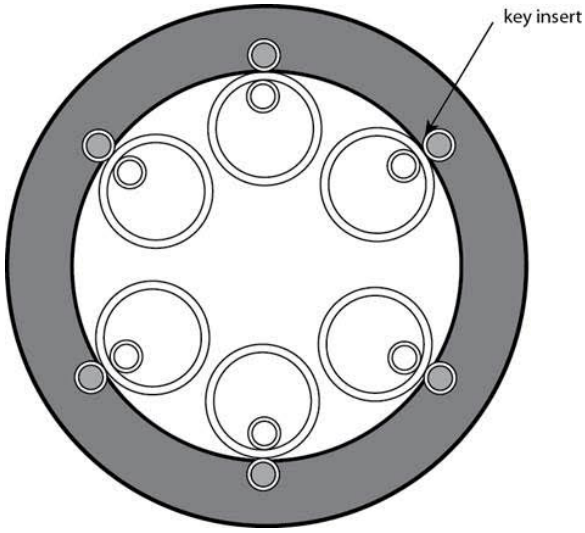

Figure 4.31: Fiber geometry showing nested elements with corresponding "key" sections.

same. Except for a slight broadening of the resonant absorption peak, the key sections do not significantly influence the loss of the fiber. The reason is that the key sections are far away from the central core mode of the fiber and are included in an already lossy section of the fiber. We therefore find that the inclusion of these key sections in a practical fiber design should not greatly influence the loss of the fundamental core mode as compared to a design that does not include these sections.

4.5 Further considerations

Future work should also investigate the higher-order mode extinction ratio, which is important for studying the trade-off between low loss for the fundamental core mode and effectively single-mode operation. The bend loss of these fibers should also be studied for different bending radii to study the effect of bending on the loss of the fiber, in order to design a fiber with minimal bending loss.

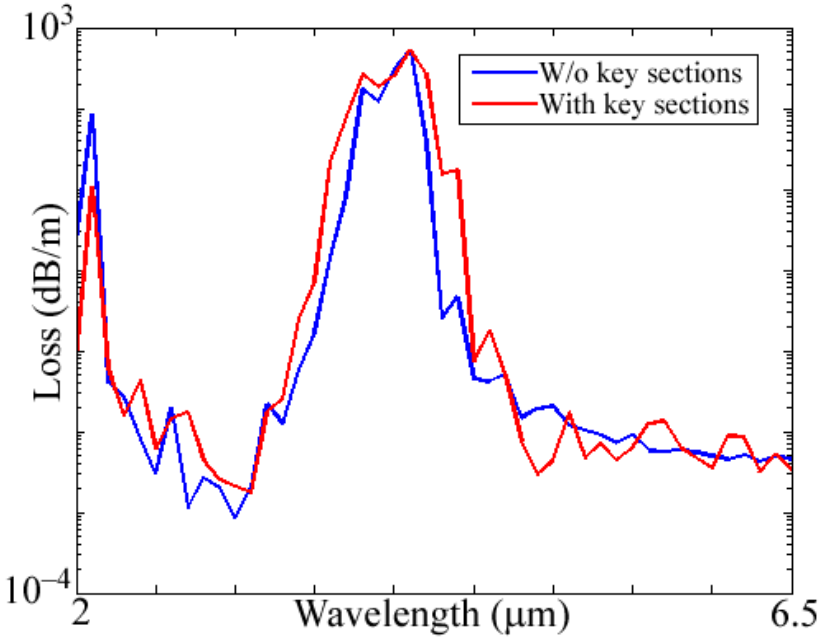

Figure 4.32: Loss as a function of wavelength for a fiber with (red) and without (blue) "key" sections.

Chapter 5

Conclusion

The mid-IR wavelength range is a scientifically interesting region of the electromagnetic spectrum because of the strong resonances of many molecules and the atmospheric transmission windows. These characteristics enable many interesting applications for devices in the mid-IR, especially sensing and defense applications. Many such applications require a broad bandwidth of high power mid-IR radiation. Therefore, technologies that generate broadband mid-IR radiation and methods for directing this radiation efficiently are of great importance.

Supercontinuum (SC) generation can be used to generate a broad bandwidth in the mid-IR using nonlinear chalcogenide optical fibers. Moth-eye structures can be used to couple broadband mid-IR radiation from one medium to another with minimal reflection loss over a wide range of wavelengths and incident angles. Hollow-core antiresonant fibers (ARFs) can be used to guide a broad bandwidth of mid-IR radiation from its generating source to another location with low loss and low spectral aberration. We have studied each of these technologies — SC generation, moth-eye structures, and antiresonant fibers — with the purpose of optimizing the parameters of their operation to obtain broadband, low-loss, and low spectral variance devices.

We investigated SC generation in As_2S_3 PCFs with a 2.8 μm input wavelength to maximize the output bandwidth. We found that it is theoretically possible to generate a 4-μm bandwidth using a PCF with a 4-μm pitch. However, we found that the optimum pulse parameters that give the absolute maximum bandwidth were difficult to determine exactly from numerical simulations, due to the extreme sensitivity of SC generation to small fluctuations in the input parameters.

In order to more accurately determine the experimentally-expected output bandwidth by numerical simulations, we devised a number of methods for calculating the output bandwidth of a SC source that are more robust to small changes in the input parameters. Using these methods, including a new bandwidth definition, spectral smoothing, and an ensemble average over one pulse parameter, we found that we could reduce the uncertainty in the output bandwidth from 22% to just over 10%. However, we still found that fluctuations in the output bandwidth persisted, continuing to make it difficult to find the optimal parameters.

In order to accurately determine the optimal parameters, we used a large ensemble average over pulses with a 10% variation in both the pulse duration and peak power to replicate the output spectrum that would be seen in an experiment. In order to do this, we completely characterized the statistical properties of output spectra from our numerical simulations and studied the effect of increasing the number of samples in the ensemble average. In so doing, we found that we could reproduce the experimentally-expected output spectrum using 5000 samples. This method can be used to determine the optimum pulse and fiber parameters for mid-IR SC generation numerically in a reasonable amount of time.

We built an exact computer model of a moth-eye structure using several different methods — FEM, FDTD, and RCWA — in order to study the anti-reflective properties of these microstructured optical surfaces. We found that we could obtain excellent agreement

between the theoretical results of our model and the experimentally-measured transmission spectrum of moth-eye structures.

We used these computer models to investigate the effect of changing the dimensions, shape, angle-of-incidence, and packing scheme of moth-eye structures on As_2S_3 glass surfaces. We found general rules for maximizing the transmission properties of moth-eye structures, and we used these rules to design and optimize nearly ideal structures that give 99.9% average transmission over a broad wavelength range from 2–5 μm.

We also investigated irradiance enhancement effects in moth-eye structures to determine the reason for the increased laser damage threshold in these structures. We found that irradiance enhancement occurs mostly on the air-side of the air-glass interface, which keeps the irradiance in the glass surface structures low, thereby avoiding catastrophic damage. We found that this effect occurs in all reasonably designed moth-eye structures and that the effect is not due to constructive interference of higher diffracted orders in the structure.

We studied hollow-core antiresonant fibers (ARFs) to design an optimal chalcogenide ARF with low loss over a broad bandwidth in the mid-IR. We determined that we could align the resonant absorption peaks in the spectrum of an As_2S_3 ARF with the naturally occurring absorption peaks in the atmosphere due to gases, such as CO_2. We demonstrated that nested elements in an ARF are essential to achieving low loss. We determined the loss in fibers with both six and eight cladding tubes, both with and without nested elements. We also investigated increasing the core radius of an ARF and explained the physical reason for the decreasing marginal efficacy of increasing the core radius, and we investigated the effect of including more nested elements in an ARF, including doubly-nested ARFs and adjacent nested ARFs. We showed that including such elements would not significantly reduce the overall loss in a fiber, since the loss is dominated by material absorption.

We showed the loss and refractive index as a function of wavelength for the fundamental mode of an optimized fiber. We found that the loss was lower than a state-of-the-art silica ARF and that the dispersion in these fibers is extremely low.

We then investigated fabrication tolerances of these fiber designs by simulating perturbations of ideal fiber structures. We studied the effect of a nonconstant cladding-tube wall-thickness and showed that this this perturbation is detrimental to the low-loss properties of an ARF. We also investigated perturbations to a single cladding tube, including a change in the tube diameter by $\pm 10\%$ and a change in the cladding-tube wall-thickness by $\pm 10\%$. We showed that the effect of these changes is small, but not negligible. Therefore, if these effects were compounded by multiple imperfect cladding tubes, the results could significantly increase the loss of an ARF. Finally, we investigated the effect of including a "key" structure in the fiber cladding support or jacket to maintain the registration between cladding tubes and their nested elements. We showed that including these structures does not significantly change the guidance and or add to the loss of an ARF.

In this dissertation, we did not exactly determine the optimal parameters for SC generation in As_2S_3 PCFs — only a method for doing so. In the future, using this method, a careful investigation into the influence of changing the input and fiber parameters on a mid-IR SC source that is not influenced by the extreme sensitivity of SC simulations could be useful and enlightening.

In the future, an investigation into moth-eye structures that have anti-reflective properties at wavelengths below their diffraction edge would be scientifically interesting and important. This dissertation outlines some possible ways to achieve such structures.

Additionally, future work on irradiance enhancement in moth-eye structures that answers specific questions about the effect of changing the structure parameters on the location and magnitude of the irradiance enhancement effect will be useful for designing

moth-eye structures with an even higher laser damage threshold and for optimizing surface enhancement effects in technologies such as surface-enhanced Raman scattering.

Future work can also investigate the trade-offs in ARFs between obtaining a low, broadband loss spectrum and 1) achieving effectively single-mode operation by higher-order mode out-coupling and 2) optimizing the bending loss.

References

[1] F. K. Tittel, D. Richter, and A. Fried, "Mid-infrared laser applications in spectroscopy," in *Solid-State Mid- Infrared Laser Sources*, I. T. Sorokina and K. L. Vodopyanov, ed. (Springer, 2003).

[2] J. S. Sanghera and I. D. Aggarwal, "Active and passive applications of chalcogenide glass fibers: a review," J. Non-Cryst. Solids **256&257**, 6–16 (1999).

[3] J. S. Sanghera, L. B. Shaw, and I. D. Aggarwal, "Chalcogenide Glass-Fiber-Based Mid-IR Sources and Applications," IEEE J. Sel. Top. Quantum Electron. **15**, 114–119, (2009).

[4] J. Hu, "Analysis of chalcogenide-glass photonic crystal fibers." Ph.D. Dissertation, UMBC (2009).

[5] R. J. Weiblen, J. Hu, C. R. Menyuk, L. B. Shaw, J. S. Sanghera, and I. D. Aggarwal, "Maximizing the Supercontinuum Bandwidth in As_2S_3 Chalcogenide Photonic Crystal Fibers," in Proc. Conference on Lasers and Electro-Optics (CLEO), San Jose, CA, paper CTuX7 (2010).

[6] R. J. Weiblen, A. Docherty, J. Hu, and C. R. Menyuk, "Calculation of the expected bandwidth for a mid-infrared supercontinuum source based on As_2S_3 chalcogenide photonic crystal fibers," Opt. Express **18**, 26666–26674 (2010).

[7] R. J. Weiblen, A. Docherty, C. R. Menyuk, L. B. Shaw, J. Sanghera, I. Aggarwal, "Efficient Calculation of the Mid-Infrared Supercontinuum Spectrum in As_2S_3 optical fibers," *IEEE Photonics Conference*, Bellevue, WA, paper WB4.4 (2013).

[8] J. Sanghera, C. Florea, L. Busse, L. B. Shaw, F. Miklos, and I. Aggarwal, "Reduced Fresnel losses in chalcogenide fibers by using anti-reflective surface structures on fiber end faces," Opt. Express **18**, 26760–26768 (2010).

[9] R. J. Weiblen, C. Florea, A. Docherty, C. R. Menyuk, L. B. Shaw, J. Sanghera, L. Busse, I. Aggarwal, "Optimizing motheye antireflective structures for maximum coupling through As_2S_3 optical fibers," *IEEE Photonics Conference*, Burlingame, CA, paper ThP3 (2012).

[10] R. J. Weiblen, C. Florea, L. Busse, L. B. Shaw, C. R. Menyuk, I. Aggarwal, and J. Sanghera, "Ideal cusp-like motheye antireflective structures for chalcogenide optical fibers," *IEEE Photonics Conference*, Reston, VA, paper WI1.4 (2015).

[11] R. J. Weiblen, C. Florea, L. Busse, L. B. Shaw, C. R. Menyuk, I. Aggarwal, and J. Sanghera, "Increased Laser Damage Threshold in As_2S_3 Motheye Antireflective Structures," in CLEO: 2014, OSA Technical Digest (online) (Optical Society of America, 2014), paper JTh3J.4.

[12] R. J. Weiblen, C. Florea, L. Busse, L. B. Shaw, C. R. Menyuk, I. Aggarwal, and J. Sanghera, "Irradiance enhancment and increased laser damage threshold in As_2S_3 moth-eye antireflective structures," Opt. Lett. **40**, 4999-4999 (2015).

[13] L. Busse, C. Florea, L. B. Shaw, S. Bayya, G. Villalobos, I. Aggarwal, and J. Sanghera, "Anti-Reflective Surface Structures for High Energy Laser Applications," *Annual Directed Energy Symposium*, Santa Fe, NM, paper 13-Symp-053 (2013).

[14] Y. Wang, F. Couny, P. J. Roberts, and F. Benabid, "Low loss broadband transmission in optimized core–shaped Kagome Hollow Core PCF," in Conference on Lasers and

Electro-Optics/Quantum Electronics and Laser Science, Postdeadline Papers (Optical Society of America, 2010), paper CPDB4.

[15] A. D. Pryamikov, A. S. Biriukov, A. F. Kosolapov, V. G. Plotnichenko, S. L. Semjonov, and E. M. Dianov, "Demonstration of a waveguide regime for a silica hollow–core microstructured optical fiber with a negative curvature of the core boundary in the spectral region > 3.5 μm," Opt. Express **19**, 1441–1448 (2011).

[16] F. Yu, W. J. Wadsworth, and J. C. Knight, "Low loss silica hollow core fibers for 34 μm spectral region," Opt. Express **20**, 11153–11158 (2012).

[17] A. F. Kosolapov, A. D. Pryamikov, A. S. Biriukov, V. S. Shiryaev, M. S. Astapovich, G. E. Snopatin, V. G. Plotnichenko, M. F. Churbanov, and E. M. Dianov, "Demonstration of CO_2-laser power delivery through chalcogenide-glass fiber with negative-curvature hollow core," Opt. Express **19**, 25723–25728 (2011).

[18] H. Kano and H. O. Hamaguchi, "Vibrationally resonant imaging of a single living cell by supercontinuum-based multiplex coherent anti-Stokes Raman scattering microspectroscopy," Opt. Express **13**, 1322–1327 (2005).

[19] A. Schliesser, N. Picque, and T. Hänsch, "Mid-infrared frequency combs," Nat. Photonics **6**, 440–449 (2012).

[20] C. S. Colley, J. C. Hebden, D. T. Delpy, A. D. Cambrey, R. A. Brown, E. A. Zibik, W. H. Ng, L. R. Wilson, and J. W. Cockburn, "Mid-infrared optical coherence tomography," Rev. Sci. Instrum. **78**, 123108 (2007).

[21] J. Hu, C. R. Menyuk, L. B. Shaw, J. S. Sanghera, and I. D. Aggarwal, "Maximizing the bandwidth of supercontinuum generation in As_2Se_3 chalcogenide fibers," Opt. Express **18,** 6722–6739 (2010).

[22] J. M. Dudley, G. Genty, and S. Coen, "Supercontinuum generation in photonic crystal fiber," Rev. Mod. Phys. **78**, 1135–1184 (2006).

[23] J. Hu, C. R. Menyuk, L. B. Shaw, J. S. Sanghera, and I. D. Aggarwal, "Computational study of 3–5 μm source created by using supercontinuum generation in As_2S_3 chalcogenide fibers with a pump at 2 μm," Opt. Lett. **35**, 2907–2909 (2010).

[24] O. V. Sinkin, R. Holzlhner, J. Zweck, and C. R. Menyuk, "Optimization of the Split-Step Fourier Method in Modeling Optical-Fiber Communications Systems," J. Lightwave Technol. **21**, 61–68 (2003).

[25] J. P. Gordon, "Theory of the soliton self-frequency shift," Opt. Lett. **11**, 662–664 (1986).

[26] J. Hu, C. R. Menyuk, L. B. Shaw, J. S. Sanghera, and I. D. Aggarwal, "Supercontinuum generation in an As_2Se_3-based chalcogenide PCF using four-wave mixing and soliton self-frequency shift," in Proc. Conference on Optical Fiber Communications (OFC), San Diego, CA, paper OWU6 (2009)

[27] J. Hu, C. R. Menyuk, L. B. Shaw, J. S. Sanghera, and I. D. Aggarwal, "Generating mid-IR source using As2S3-based chalcogenide photonic crystal fibers," in Proc. Conference on Lasers and Electro-Optics (CLEO), paper CThN6 (2009)

[28] J. Dudley and S. Coen, "Coherence properties of supercontinuum spectra generated in photonic crystal and tapered optical fibers," Opt. Lett. **27**, 1180–1182 (2002).

[29] F. G. Omenetto, N. A. Wolchover, M. R. Wehner, M. Ross, A. Efimov, A. J. Taylor, V. V. Kumar, A. K. George, J. C. Knight, N. Y. Joly, and P. S. Russell, "Spectrally smooth supercontinuum from 350 nm to 3 μm in sub-centimeter lengths of soft-glass photonic crystal fibers," Opt. Express **14**, 4928–4934 (2006).

[30] J. H. Price, T. M. Monro, H. Ebendorff-Heidepriem, F. Poletti, F. Vittoria, J. Y. Leong, P. Petropoulos, J. C. Flanagan, G. Brambilla, X. Feng, and D. J. Richardson, "Non-silica microstructured optical fibers for mid-IR supercontinuum generation from 2 μm–5 μm," IEEE J. of Sel. Top. in Quantum Electron. **13**, 738–749 (2007).

[31] D. R. Solli, C. Ropers, P. Koonath, and B. Jalali, "Optical rogue waves," Nature **450**, 1054–1057 (2007).

[32] Lord Rayleigh, "On reflection of vibrations at the confines of two media between which the transition is gradual," Proc. London Math. Soc., **S1–11**, 51–56 (1879).

[33] C. G. Bernhard and W. H. Miller, "A corneal nipple pattern in insect compound eyes," Acta Physiol. Scand. **56**, 385–386 (1962).

[34] S. Chattopadhyay, Y. F. Huang, Y. J. Jen, A. Ganguly, K. H. Chen, and L. C. Chen, "Anti-reflecting and photonic nanostructures," Materials Science and Engineering R **69**, 1–35 (2010).

[35] J. Kulakofsky, W. Lewis, M. Robertson, T. Moore, and G. Krishnan, "Designing high-power components for optical telecommunications," Proc. SPIE **4679**, 198–210 (2002).

[36] S. A. Boden and D. M. Bagnall, "Optimization of moth-eye antireflection schemes for silicon solar cells," Prog. Photovolt: Res. Appl. **18**, 195–203 (2010).

[37] Y. Ou, D. Corell, C. Dam-Hansen, P. Petersen, and H. Ou, "Antireflective sub-wavelength structures for improvement of the extraction efficiency and color rendering index of monolithic white light-emitting diode," Opt. Express **19**, A166–A172 (2011).

[38] D. S. Hobbs, B. D. MacLeod, and J. R. Riccobono, "Update on the development of high performance anti-reflecting surface relief micro-structures," Proc. SPIE **6545**, 65450Y (2007).

[39] T. Hoshino, M. Itoh, and T. Yatagai, "Antireflective grating in the resonance domain for displays," Appl. Opt. **46**, 648–656 (2007).

[40] B. D. MacLeod, D. S. Hobbs, and E. Sabatino, "Moldable AR microstructures for improved laser transmission and damage resistance in CIRCM fiber optic beam delivery systems," Proc. SPIE **8016**, 80160Q (2011).

[41] K. Han and C.-H. Chang "Numerical modeling of sub-wavelength anti-reflective structures for solar module applications," Nanomaterials **4**, 87–128 (2014).

[42] J. Yamauchi, M. Mita, S. Aoki, and H. Nakano, "Analysis of antireflection coatings using the FD-TD method with the PML absorbing boundary condition," IEEE Photon. Technol. Lett. **8**, 239–241 (1996).

[43] Z. Y. Yang, D. Q. Zhu, M. Zhao, and M. C. Cao, "The study of a nano-porous optical film with the finite difference time domain method," J. Opt. A: Pure Appl. Opt., **6**, 564–568 (2004).

[44] M. G. Moharam and T. K. Gaylord, "Rigorous coupled-wave analysis of planar-grating diffraction," J. Opt. Soc. Am. **71**, 811–818 (1981).

[45] L. Li, "New formulation of the Fourier modal method for crossed surface-relief gratings," J. Opt. Soc. Am. A **14**, 2758–2767 (1997).

[46] D. S. Hobbs, B. D. MacLeod, E. Sabatino III, T. M. Hartnett, and R. L. Gentilman, "Laser damage resistant anti-reflection microstructures in Raytheon ceramic YAG, sapphire, ALON, and quartz." Proc. of SPIE **8016**, 80160T (2011).

[47] D. S. Hobbs, "Laser Damage Threshold Measurements of Anti-Reflection Microstructures Operating in the Near UV and Mid-IR," Proc. SPIE **7842**, 78421Z (2010).

[48] C. Florea, L. Busse, S. Bayyab, B. Shaw, I. Aggarwal, and J. Sanghera, "Anti-reflective surface structures in spinel ceramic windows," *The 10th Pacific Rim Conference on Ceramic and Glass Technology*, San Diego, CA, paper S10-014 (2013).

[49] D. G. Stavenga, S. Foletti, G. Palasantzas, and K. Arikawa, "Light on the moth-eye corneal nipple array of butterflies," Proc. Biol. Sci. **273**, 661–667 (2006).

[50] A. F. Oskooi, D. Roundy, M. Ibanescu, P. Bermel, J. D. Joannopoulos, and S. G. Johnson, "MEEP: A flexible free-software package for electromagnetic simulations by the FDTD method," Comp. Phys. Comm. **181**, 687–702 (2010).

[51] D. Raguin and G. Morris, "Antireflection structured surfaces for the infrared spectral region," Appl. Opt. **32**, 1154–1167 (1993).

[52] W. H. Southwell, "Pyramid-array surface-relief structures producing antireflection index matching on optical surfaces," J. Opt. Soc. Am. A **8**, 549–553 (1991).

[53] J. F. DeFord and M. R. Kozlowski, "Modeling of electric-field enhancement at nodular defects in dielectric mirror coatings," Proc. SPIE **1848**, 455–476 (1993).

[54] X. Cheng, T. Ding, B. Ma, H. Jiao, J. Zhang, Z. Shen, and Z. Wang, "Defect-driven laser-induced damage in optical coatings," in CLEO: 2014, OSA Technical Digest (online) (Optical Society of America, 2014), paper JTh3J.1.

[55] Roger M. Wood, *Laser-Induced Damage of Optical Materials* (Institute of Physics Publishing, 2003).

[56] X. Jing, J. Shao, J. Zhang, Y. Jin, H. He, and Z. Fan, "Calculation of femtosecond pulse laser induced damage threshold for broadband antireflective microstructure arrays," Opt. Express **17**, 24137–24152 (2009).

[57] M. Steel, T. White, C. M. de Sterke, R. McPhedran, and L. Botten, "Symmetry and degeneracy in microstructured optical fibers," Opt. Lett. **26**, 488–490 (2001).

[58] V. R. Almeida, Q. Xu, C.A. Barrios, and M. Lipson, "Guiding and confining light in void nanostructure, Opt. Lett. **29**, 1209–1211 (2004).

[59] M. Born and E. Wolf, *Principles of optics* (Cambridge University Press, 2003).

[60] Y.-F. Huang, S. Chattopadhyay, et al., "Improved broadband and quasi-omnidirectional anti-reflection properties with biomimetic silicon nanostructures," Nature Nanotech. **2** 770–774 (2007).

[61] M. A. Duguay, Y. Kokubun, T. L. Koch, and L. Pfeiffer, "Antiresonant reflecting optical waveguides in SiO_2Si multilayer structures," Appl. Phys. Lett. **49**, 13–15 (1986).

[62] F. Benabid, J. C. Knight, G. Antonopoulos, and P. St. J. Russell, "Stimulated Raman scattering in hydrogen-filled hollow-core photonic crystal fiber," Science **298**, 399–402 (2002).

[63] A. Argyros, S. G. Leon-Saval, J. Pla, and A. Docherty, "Antiresonant reflection and inhibited coupling in hollow-core square lattice optical fibres," Opt. Express **16**, 5642–5648 (2008).

[64] F. Benabid, F. Gerome, B, Debord, and M. Alharbi, "Fiber For Fiber Lasers: Kagome PC fiber goes to extremes for ultrashort-pulse lasers," Laser Focus World **50** 29–34 (2014).

[65] A. N. Kolyadin, A. F. Kosolapov, A. D. Pryamikov, A. S. Biriukov, V. G. Plotnichenko, and E. M. Dianov, "Light transmission in negative curvature hollow core fiber in extremely high material loss region," Opt. Express **21**, 9514–9519 (2013).

[66] W. Belardi and J. C. Knight, "Effect of core boundary curvature on the confinement losses of hollow antiresonant fibers," Opt. Express **21**, 21912–21917 (2013).

[67] W. Belardi and J. C. Knight, "Hollow antiresonant fibers with low bending loss," Opt. Express **22**, 10091–10096 (2014).

[68] F. Poletti, J. R. Hayes, and D. J. Richardson, "Nested antiresonant nodeless hollow core fiber," Opt. Express **22**, 23807 (2014).

[69] M. S. Habib, O. Bang, and M. Bache, "Low-loss hollow-core silica fibers with adjacent nested anti-resonant tubes," Opt. Express **23**, 17394 (2015).

[70] C. Wei, R. A. Kuis, F. Chenard, C. R. Menyuk, and J. Hu, "Higher-order mode suppression in chalcogenide negative curvature fibers," Opt. Express **23**, 15824–15832 (2015).

[71] F. Poletti et al., "Optimising the performances of hollow antiresonant fibres," ECOC Technical Digest, paper Mo.2.LeCervin.2 (2011).

[72] N. M. Litchinitser, A. K. Abeeluck, C. Headley, and B. J. Eggleton, "Antiresonant reflecting photonic crystal optical waveguides," Opt. Lett. **27**, 1592–1594 (2002).

[73] L. Vincetti, and V. Setti, "Waveguiding mechanism in tube lattice fibers," Opt. Express **18**, 23133–23146 (2010).